University of São Paulo
Institute of Astronomy, Geophysics and Atmospheric Sciences
Department of Atmospheric Sciences

Gláuber Camponogara

# Relationship between biomass burning aerosols from Amazon and mesoscale convective systems over the La Plata Basin

# Interação entre aerossóis de queimadas na Amazônia e sistemas convectivos de mesoescala na Bacia do Prata

São Paulo

2017

Gláuber Camponogara

# Relationship between biomass burning aerosols from Amazon and mesoscale convective systems over the La Plata Basin

# Interação entre aerossóis de queimadas na Amazônia e sistemas convectivos de mesoescala na Bacia do Prata

Thesis submitted in partial fulfillment of the requirements for the degree of Doctor of Sciences in the Institute of Astronomy, Geophysics and Atmospheric Sciences.

Major field: Meteorology
Advisor: Maria Assunção Faus da Silva Dias
Co-advisor: Gustavo G. Carrió

Final version. The original copy is available in the library.

São Paulo

2017

*Dedicated to my family.*

# Acknowledgements

I would like to offer profound thanks to my advisor, Prof. Dr. Maria Assunção, for giving me the opportunity of working on this research under her guidance and for her valuable insight. It has been over seven years working together and during this period I have developed my skills as a scientist having her as an example to follow;

I am truly grateful for all the support and encouragement given by my co-advisor, Dr. Gustavo G. Carrió. I have a better understanding of cloud microphysics and data assimilation under his wise guidance;

I would like to acknowledge Prof. Dr. Edmilson, Prof. Dr. Hallack and Prof. Dr. Pedro, for their suggestions with respect to this research.

I thank Dr. Saulo Freitas for his support with respecto to BRAMS.

I thank Dr. Louie Grasso for his assistance with CRTM as well as for his rides and interesting conversations.

I would like to thank all my friends and colleges, in particular, Mercel, for discussing my work and for sharing his knowledge.

I also would like to thank the staff of the IAG for all their efficient support during the course of this project.

This project would have been impossible without the financial support of CAPES and FAPESP (grants no. 2012/08115-9 and 2014/05351-9)

I thank my family, Ivani, Luiz, Ândrei and Douglas, for their encouragement, support, and unconditional love;

I would like to give an especial thanks to my girlfriend, Carol, that has always been kind and supportive, encouraging me to give my best in my research. She has always believed me even when I did not believe in myself. I also would like to thank her family, Maria Cida, Shirlei and Rogério, for their kindness and friendship.

---

Esta tese/dissertação foi escrita em LaTeX com a classe IAGTESE, para teses e dissertações do IAG.

"*The cure for a fallacious argument is a better argument, not the suppression of ideas*"

Carl Sagan

# Resumo

Altas cargas de aerossóis são liberadas na atmosfera através da queima de biomassa na Amazônia e Brasil Central durante a estação seca. Estas partículas podem interagir com as nuvens como núcleos de condensação (CCN), alterando as propriedades microfísicas e radiativas das nuvens e, portanto, afetando o balanço radiativo da região. Além disso, os aerossóis oriundos de queima de biomassa podem ser transportados pelo jato de baixos níveis (LLJ) para a Bacia do Prata, onde os sistemas convectivos de mesoescala (MCS) são observados com mais frequência durante as estações de primavera e verão. Este tema não tem sido estudado e, portanto, existem algumas questões em aberto sobre como os aerossóis de queima de biomassa na Amazônia interagem com os MCS que se formam na Bacia do Prata. Esse trabalho propõe investigar como esses aerossóis podem afetar os MCS na Bacia do Prata durante a estação de primavera. Os efeitos dos aerossóis são difíceis de isolar, pois nuvens convectivas são muito sensíveis à pequenas perturbações do ambiente, por esse motivo, uma análise detalhada utilizando diferentes técnicas é empregada. Os métodos binplot, histograma 2D e funções ortogonais empíricas (EOF) combinadas são utilizados para identificar condições do ambiente com possíveis efeitos dos aerossóis. Os dados de reanálise 2, TRMM-3B42 e AERONET são utilizados cobrindo o período que vai de 1999 a 2012 durante Setembro–Dezembro. Esses resultados mostram que existem dois padrões associados à interação chuva–aerossol na Bacia do Prata: o primeiro no qual as condições dinâmicas são mais importantes que os aerossóis para gerar chuva; e o segundo onde as partículas de aerossol tem um importante papel na formação da precipitação, agindo principalmente no sentido de suprimir a chuva sobre a bacia. Experimentos numéricos variando as concentrações de CCN foram realizados através do modelo BRAMS-4.3 para um caso de MCS observado na Bacia do Prata em 21 de setembro de 2010. Os

experimentos revelam uma ligação entre a concentração de CCN e a dinâmica do MCS, onde fortes correntes descendentes foram observadas sob altas quantidades de aerossóis, produzindo mais células de correntes ascendentes como resposta. Em adição, as simulações mostram maiores volumes de precipitação conforme a concentração de CCN aumenta, o que aparenta contradizer os resultados observacionais mostrados neste trabalho. Uma melhoria nos resultados numéricos consistiu em desenvolver o sistema Mesoscale Assimilation (MESOASSIM) para assimilar radiações de satélite no infravermelho no BRAMS-4.3. O MESOASSIM foi capaz de diminuir o erro médio quadrático da temperatura de brilho ajustando as variáveis estado do modelo. Como consequência, foi obtida uma melhoria no campo de precipitação da simulação.

Palavras-chave: sistemas convectivos de mesoescala, CCN, modelagem numérica, assimilação de dados, Bacia do Prata.

# Abstract

High aerosol loads are discharged into the atmosphere by biomass burning in Amazon and Central Brazil during the dry season. These particles can interact with clouds as cloud condensation nuclei (CCN) changing cloud microphysics and radiative properties and, thereby affecting the radiative budget of the region. Furthermore, the biomass burning aerosols can be transported by the low level jet (LLJ) to La Plata Basin where mesoscale convective systems (MCS) are observed frequently during spring and summer seasons. Unfortunately, this issue has not been addressed yet and, therefore, there are some open questions about how Amazon's biomass burning aerosols interact with La Plata Basin's MCSs. This work proposes to investigate how these aerosols may affect the MCSs over the La Plata Basin during spring. Aerosol effects are difficult to isolate because convective clouds are very sensitive to small environment disturbances, for that reason, detailed analysis using different techniques are used. The binplot, 2D histograms and combined empirical orthogonal function (EOF) methods are used to identify certain environmental conditions with the possible effects of aerosol loading. Reanalysis 2, TRMM-3B42 and AERONET data are used from 1999 up to 2012 during September-December. The results show that there are two patterns associated with rainfall-aerosol interaction in La Plata Basin: one in which the dynamic conditions are more important than aerosols to generate rain; and a second one where the aerosol particles have a more important role in rain formation, acting mainly to suppress rainfall over the basin. Numerical experiments varying CCN concentrations were performed through the model BRAMS-4.3 for an MCS case observed over the La Plata Basin on 21 September 2010. The experiments reveal a link between CCN number concentration and MCS's dynamics, where stronger downdrafts were observed under higher amounts of aerosols, generating more updraft cells in response. Moreover, the

simulations show higher amounts of precipitation as CCN concentration increases, which goes in opposite direction of observation's outcomes presented here. In attempt to improve these numerical results the Mesoscale Assimilation system (MESOASSIM) has been developed to assimilate infrared satellite radiances into BRAMS-4.3. The MESOASSIM framework was able to decrease the root mean square error of the brightness temperature by adjusting the model state variables. As a consequence, the model's precipitation field was improved.

Keywords: mesoscale convective systems, CCN, numerical modeling, data assimilation, La Plata Basin.

# List of Figures

1.1 The La Plata Basin and its main rivers. . . . . 30

2.1 Climatological distribution of MCSs over South America for each season (Silva Dias et al., 2009). The figure is a compilation of results from Velasco and Fritsch (1987), Conforte (1997), Torres and Nicolini (2002), Salio et al. (2007). The MCSs observed during SALLJEX (Vera et al., 2006) are indicated. 37

2.2 Schematic illustration about this work context. The graphics are climatologies of AOD for Rio Branco and Alta Floresta AERONET stations, and rainfall estimative from TRMM-3B42 for Asunción, Santa Maria and Buenos Aires cities. Ji Paraná, Cuiabá, Santa Cruz, and Campo Grande AOD stations are located in red. . . . . 38

2.3 Mean wind of north flow cases identified by the filtering method. Blue box represents the study area, red box is an auxiliary region for the filter and thick black contour delimits the La Plata Basin. . . . . 40

2.4 Daily AOD during September 2007 from AERONET stations. There were not measurements from Santa Cruz station on this period. . . . . 44

2.5 Enhanced infrared satellite images from GOES 11 for a MCS evolution on 12 September 2007 over the La Plata Basin. Colors indicate infrared temperatures. (a) 05:00 UTC, (b) 06:45 UTC, (c) 10:15 UTC, and (d) 14:45 UTC. . . . . 45

2.6 Large-scale fields on 12 September 2007 at 06:00 UTC: (a) wind and relative humidity at 850 hPa; (b) mean 700-500 hPa relative humidity (shaded) and $\omega$ at 500 hPa (contour); (c) wind and divergence at 200 hPa. . . . . 46

2.7 Rainfall rate binned by AOD range of 0.1 for each AERONET station for all selected cases (see Sect. 2.2.4) during the months of September-October-November-December of 1999-2012. . . . . 47
2.8 Two-dimensional histogram of average rainfall rate for each AERONET station for all selected cases (see Sect. 2.2.4) during the months of September-October-November-December of 1999-2012. Colors indicate average rainfall rate for each bin of rainfall fraction and AOD. . . . . 48
2.9 Two-dimensional histogram of average rainfall rate for each AERONET station for all selected cases (see Sect. 2.2.4) during the months of September-October-November-December of 1999-2012. Colors indicate average rainfall rate for each bin of $\omega$ and AOD. . . . . 49
2.10 EOFs and their components AOD, RR, $\omega$, and RH for each AERONET station for all selected cases (see Sect. 2.2.4) during the months of September-October-November-December of 1999-2012. Colors indicate the stations of Alta Floresta (AF), Ji Paraná (JP), Rio Branco (RB), Santa Cruz (SC), Campo Grande (CG), and Cuiabá (CB). . . . . 51

3.1 Model domain for 16 km (brown box), 4 km (blue box) and 2.5 km (red box) of grid spacing. The topography elevation of the La Plata Basin is shaded. . . . . 59
3.2 Vertical profiles of CCN concentrations used to initialize the numberical model. . . . . 60
3.3 Enhanced infrared satellite images from GOES 12 for an MCS case observed over the La Plata Basin on 21 September 2010. Colors indicate infrared temperatures. . . . . 61
3.4 Synoptic fields on 21 September 2010 at 00:00 UTC: (a) sea level pressure (contour lines) and thickness (shaded); (b) wind (vectors) and specific humidity (shaded) at 850 hPa; (c) geopotential height (contour) and vertical p-velocity (shaded) at 500 hPa; and (d) wind direction (vector) and magnitude (shaded) at 250 hPa. . . . . 63

3.5 Synthetic infrared satellite images for the CN-Low, CN-Med, CN-High and CN-ExtHigh experiments at 06:00 (left panels), 08:30 (middle panels) and 11:00 UTC (right panels). Colors indicate brightness temperature at channel 10.7 $\mu$m. The black contour line refers to the brightness temperature equal to -32 °C, which delimits the MCS area (Maddox, 1980). . . . . 65
3.6 Precipitation covered area (km$^2$), maximum precipitation rate (mm/h) and total accumulated precipitation ($1 \times 10^5$ mm) as a function of time for the CN-Low (blue), CN-Med (marigold), CN-High (green) and CN-ExtHigh (red) experiments. The shaded area in grey represents the time period that the entire MCS is within the grid domain. . . . . 66
3.7 Total upwelling vapor flux at cloud base as function of time for the CN-Low (blue), CN-Med (marigold), CN-High (green) and CN-ExtHigh (red) experiments. The shaded area in grey represents the time period that the entire MCS is within the grid domain. . . . . 67
3.8 Total area of updraft (km$^2$) and number of updraft cells as a function of time for the CN-Low (blue), CN-Med (marigold), CN-High (green) and CN-ExtHigh (red) experiments. The volume integral of concentrations is weighted by their respective mass. The shaded area in grey represents the time period that the entire MCS is within the grid domain. . . . . 69
3.9 Volume integrals of cloud, drizzle, rain and supercooled cloud in terms of mass ($1 \times 10^8$ kg) and number concentration ($1 \times 10^5$ m$^{-3}$) throughout time for the CN-Low (blue), CN-Med (marigold), CN-High (green) and CN-ExtHigh (red) experiments. Only grid columns with updraft greater than 5 m/s are considered in the computation. The number concentrations are weighted by their respective mass. The shaded area in grey represents the time period that the entire MCS is within the grid domain. . . . . 71
3.10 Mean vertical profiles of mixing ratio (g/kg) and number concentration ($1 \times 10^6$ m$^{-3}$) for cloud, drizzle, rain and supercooled cloud for the CN-Low (blue), CN-Med (marigold), CN-High (green) and CN-ExtHigh (red) experiments. Only grid columns with updraft greater than 5 m/s are considered in the computation. . . . . 72
3.11 As in Figure 3.9, but for pristine and aggregate categories. . . . . 73

3.12 As in Figure 3.10, but for pristine and aggregate categories. . . . . 74
3.13 As in Figure 3.9, but for graupel and hail mixing ratios. . . . . 75
3.14 As in Figure 3.10, but for graupel and hail mixing ratios. . . . . 76
3.15 Average of the three highest updraft peaks throughout time (a) and strongest updraft profile (b) for the CN-Low (blue), CN-Med (marigold), CN-High (green) and CN-ExtHigh (red) experiments. The shaded area in grey represents the time period that the entire MCS is within the grid domain. . 77
3.16 Averaged buoyancy, rain mixing ratio and downdraft between 9:00 and 10:00 UTC for the CN-Low (blue), CN-Med (marigold), CN-High (green) and CN-ExtHigh (red) experiments. The model outputs were saved every 5 min to compute these profiles. Only vertical velocities smaller than -1 m/s are considered for the average. . . . . 78

4.1 Flow diagram of MESOASSIM. . . . . 88
4.2 Model domain for 16 km (brown box) and 8 km (blue box) grid spacing. The topography elevation within the La Plata Basin region is shaded. . . . . 91
4.3 Infrared satellite data from GOES 12 for an MCS observed on 21 September 2010. Colors indicate the brightness temperature at channel 10.7 $\mu$m. . . . 94
4.4 Synthetic infrared satellite images computed by CRTM for the NoAssim experiment from 06:00 UTC (cycle 1) up to 12:00 UTC (cycle 7), with one hour of interval. Colors indicate the brightness temperature at channel 10.7 $\mu$m. . . . . 95
4.5 As in Figure 4.4, but for the Analysis experiment. . . . . 96
4.6 Difference between the BTs from the Analysis and FGuess experiments for all assimilation cycles (from 06:00 UTC up to 12:00 UTC, with one hour of interval). . . . . 97
4.7 Total cost function normalized by the number of observations. Colors indicate the respective minimization iteration where marigold represents the first iteration, green indicates the second iteration and red refers to the third iteration. The color blue represents the total cost function before minimization. . . . . 98

4.8 Root mean square error of BT from NoAssim, FGuess and Analysis for all observations. FGuess refers to the fist guess brightness temperature that is computed from Analysis before the cost function minimization. . . . . 99
4.9 Root mean square error of BT from NoAssim, FGuess and Analysis over the MCS area (58°W–46.2°W and 34°S–25°S). The Fguess refers to the fist guess brightness temperature that is computed from Analysis before the cost function minimization. . . . . 100
4.10 Average of the five strongest updrafts and downdrafts of the NoAssim and Analysis experiments for each assimilation cycle, except for the first one. . 101
4.11 Wind field at 2 km height for the NoAssim (left panel) and Analysis (right panel) experiments. The wind direction is represented by vectors and its magnitude (m/s) is shaded. . . . . 102
4.12 Vapor mixing ratio (g/kg) at 2 km height for the NoAssim (left panel) and Analysis (right panel) experiments. . . . . 103
4.13 Ice-liquid potential temperature (K) at 2 km height for the NoAssim (left panel) and Analysis (right panel) experiments. . . . . 103
4.14 Wind field at 10 km height for the NoAssim (left panel) and Analysis (right panel) experiments. The wind direction is represented by vectors and its magnitude (m/s) is shaded. . . . . 104
4.15 Accumulated precipitation from 06:00 UTC (cycle 1) to 12:00 UTC (cycle 7) computed from the TRMM-3B42's precipitation product and the NoAssim and Analysis experiments. . . . . 105

A.1 Skew-t diagram of temperature, dew point temperature and wind used in the numerical experiments. . . . . 129
A.2 Total grid integration of supercooled cloud water, rain and hail mixing ratios as well as maximum vertical velocity from BRAMS (blue line) and RAMS (red line). The experiments with low and high CCN concentrations are represented by solid and dashed, respectively. These numerical simulations were done by using the 2M scheme. . . . . 131
A.3 Same as Figure A.2, but with 3MHAIL scheme. . . . . 132

A.4 Surface amounts of rain during 45 minutes of simulation from BRAMS and RAMS for low and high CCN concentrations using the 2M microphysical parametrization. . . . . 133
A.5 Surface amounts of hail (ach) during 45 minutes of simulation from BRAMS and RAMS for high and low CCN concentrations using the 2M microphysical parametrization. . . . . 134
A.6 Same as Figure A.4 but using 3MHAIL scheme. . . . . 135
A.7 Same as Figure A.5 but using 3MHAIL scheme. . . . . 136

# List of Tables

2.1 Variance explained by the first and second EOFs and the variance explained by these two EOFs for each AOD station for all selected cases (see Sect. 2.2.4) during the months of September-October-November-December of 1999-2012. . . . . 50

3.1 BRAMS main configuration. . . . . 60

4.1 Grid configurations used in the MESOASSIM experiments. . . . . 89

4.2 Main configurations used in the simulations with MESOASSIM for the MCS case occurred on 21 September 2010. . . . . 92

# Lista of Abbreviations

| | | |
|---|---|---|
| AERONET | – | Aerosol Robotic Network |
| AOD | – | Aerosol Optical Depth |
| BRAMS | – | Brazilian developments on the Regional Atmospheric Modeling System |
| BT | – | Brightness Temperature |
| CATT | – | Coupled Aerosol and Tracer Transport model |
| CCN | – | Cloud Condensation Nuclei |
| CFSR | – | National Centers for Environmental Prediction |
| CRTM | – | Community Radiative Transfer Model |
| CPTEC | – | *Centro de Previsão do Tempo e Estudos Climáticos* |
| DOE | – | Department of Energy |
| EnKF | – | Ensemble Kalman Filter |
| EnsDA | – | Ensemble Data Assimilation |
| EOF | – | Empirical Orthogonal Functions |
| JCSDA | – | US Joint Center for Satellite Data Assimilation |
| GCCN | – | Giant Cloud Condensation Nuclei |
| GEOS-5 SCM | – | Goddard Earth Observing System Single Column Model |
| GOES | – | Geostationary Operational Environmental Satellite |
| IDW | – | Inverse Distance Weighting |
| IFN | – | Ice-forming Nuclei |
| INPE | – | *Instituto Nacional de Pesquisas Espaciais* |
| LLJ | – | Low-level Jet |
| LNCC | – | *Laboratório Nacional de Computação Científica* |
| MCS | – | Mesoscale Convective System |
| MESOASSIM | – | Mesoscale Assimilation system |

MLEF – Maximum Likelihood Ensemble Filter

NASA – National Aeronautic Spatial Agency

NCEP – National Centers for Environmental Prediction

NCAR – National Center for Atmospheric Research

NDVI – Normalized Difference Vegetation Index

OAS – Organization of American States

RAMS – Regional Atmospheric Modeling System

RMSE – Root Mean Square Error

$\text{RMSE}_{tot}$ – root mean square error for all observations

$\text{RMSE}_{mcs}$ – root mean square error for observations over the MCS area

TRMM – Tropical Rainfall Measurement Mission Project

UTC – Coordinated Universal Time

WRF – Weather Research and Forecasting

WWAP – World Water Assessment Program of United Nation

# List of Symbols

| | | |
|---|---|---|
| $\omega$ | – | vertical p velocity |
| RH | – | mean relative humidity between 700 and 500 hPa |
| RR | – | areal average of rainfall rate |
| $n$ | – | number of cases selected |
| $R^2$ | – | variance explained |
| $e_1$ | – | first eigenvector |
| $e_2$ | – | second eigenvector |
| $J$ | – | cost function |
| $\boldsymbol{x}$ | – | State vector |
| $N_{state}$ | – | state vector length |
| $\boldsymbol{x}_b$ | – | background state vector |
| $H$ | – | nonlinear observation operator |
| $\boldsymbol{y}$ | – | observation vector |
| $N_{obs}$ | – | number of observations |
| $\boldsymbol{P}_f$ | – | forecast error covariance matrix |
| $M$ | – | forecast model |
| $\boldsymbol{p}_i$ | – | random perturbation vector for each ensemble member $i$ |
| $\boldsymbol{b}_i$ | – | column $i$ of matrix $\boldsymbol{P}_f^{1/2}$ |
| $\zeta$ | – | control vector |
| $N_{ens}$ | – | number of ensemble members |
| $\boldsymbol{I}$ | – | identity matrix |
| $k$ | – | minimization iteration |
| $\alpha$ | – | step-length |

$\boldsymbol{d}$ – descent direction

$\boldsymbol{V}$ – eigenvector

$\boldsymbol{\Lambda}$ – eigenvalue

$\boldsymbol{J}_f$ – forecast term of the cost function

$\boldsymbol{J}_{obs}$ – observation term of the cost function

# Contents


*1. Introduction* . . . . . 29

1.1 Objective . . . . . 31

*2. Observational background* . . . . . 33

2.1 Introduction . . . . . 33

2.2 Data and methods . . . . . 39

2.2.1 Reanalysis 2 . . . . . 39

2.2.2 TRMM-3B42 . . . . . 39

2.2.3 AERONET . . . . . 40

2.2.4 Filtering . . . . . 41

2.2.5 Binplot . . . . . 42

2.2.6 2-D histograms . . . . . 42

2.2.7 Combined EOF . . . . . 42

2.3 A case study . . . . . 43

2.4 Results and discussion . . . . . 47

2.5 Conclusions . . . . . 51

*3. Numerical experiments with CCN concentrations* . . . . . 53

3.1 Introduction . . . . . 53

3.2 Methodology . . . . . 57

3.2.1 Atmospheric model . . . . . 57

3.2.2 Experiments design . . . . . 58

3.3 Results . . . . . 61

3.4 Conclusions . . . . . 79

*4. Mesoscale data assimilation* . . . 81
4.1 Introduction . . . 81
4.2 Methodology . . . 84
4.2.1 MESOASSIM . . . 84
4.2.1.1 Maximum likelihood ensemble filter . . . 84
4.2.1.2 Observation operator . . . 86
4.2.1.3 Computational suite . . . 87
4.2.1.4 Implementation issues . . . 89
4.2.2 Experiment design . . . 90
4.3 Results . . . 92
4.4 Conclusions . . . 106

*5. Main conclusions and future work* . . . 109
5.1 Future work . . . 111
5.2 Final statement . . . 112

*Bibliography* . . . 113

*Appendix* 125

*A. Implementations on BRAMS–4.3* . . . 127
A.1 Updates, adjustments and code problems . . . 127
A.2 Validation of microphysical parameterizations . . . 129

Chapter 1

# Introduction

The La Plata Basin, is the fifth-largest hydrographic basin in the world and the second-largest in South America, covering an area of 3.200.000 km$^2$ (Figure 1.1) and staying only behind the Amazon Basin. This basin is located in the most populous regions in the South American continent, extending to territories of five countries, Brazil, Argentina, Uruguay, Paraguay and Bolivia with a total over 100 million inhabitants (World Water Assessment Program of United Nation – WWAP, 2009). Great part of the domestic consumption of these regions is supplied by water stored in the La Plata Basin as well as the demands of industry, agricultural activities and hydropower generation. In addition, this basin works as a recharge zone for the Guarani Aquifer, one of the largest underground reservoirs of fresh water in the world.

The total hydroelectric potential of the La Plata Basin is about 92000 MW, of which half are being used (Organization of American States – OAS [1], 2006), with 75 hydroelectric dams placed over its rivers. The main sub basins are Paraná, Uruguay and Paraguay. The main hydroelectric dams are Itaipú (second biggest in the world and placed between Brazil and Paraguay), Salto Grande (placed between Argentina and Uruguay) and Yacyreta (between Argentina and Paraguay). The Itaipú dam, in particular, with 20 generating units and 14000 MW of generation capacity, supplies an energy consumption of approximately 15% for Brazil and 75% for Paraguay (`www.itaipu.gov.br`). Hence, the La Plata Basin plays an important social and economic role in the region and, therefore, it is important to understand the atmospheric phenomena that modulate the amount of precipitation over its rivers.

[1] `http://www.oas.org/usde/plata/comerciof.htm`

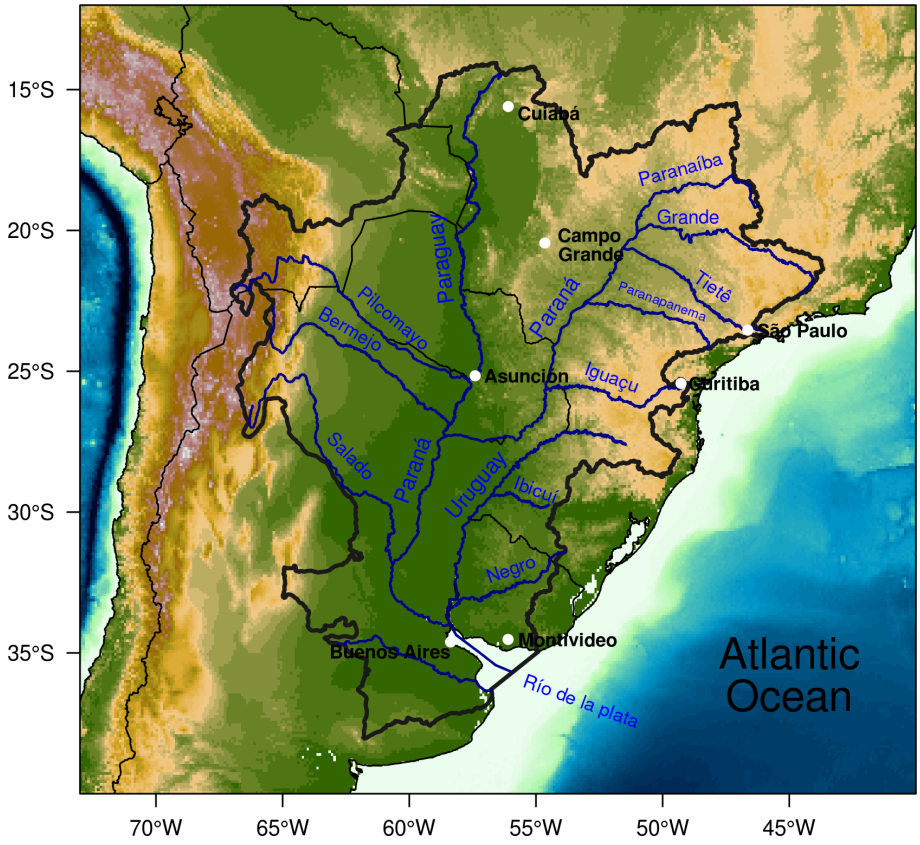


*Figure 1.1:* The La Plata Basin and its main rivers.

The La Plata Basin's precipitation regime is modulated throughout the year by meteorological phenomena such as mesoscale convective systems (MCS), cold fronts, cyclones and cut-off lows (Reboita et al., 2010). According to Zipser et al. (2006), the MCSs that are observed over the La Plata Basin are seen as the most intense in the world. These systems are observed more often in spring and summer seasons in the basin (Silva Dias et al., 2009). Generally, these systems form over Argentina between 18:00 and 00:00 UTC and displace to the east toward Uruguay and southern Brazil during daytime (Machado et al., 1998; Salio et al., 2007) or even to the northwest toward Paraguay (Anabor et al., 2008). The MCSs are responsible for approximately 90% of the total rain over the basin (Nesbitt et al., 2006) and can generate flooding due to their capacity of generating high precipitation rates (Salio et al., 2007).

High aerosol loadings are observed in the atmosphere as a result of biomass burning during the Amazon Basin and Central Brazil dry season (July–December) as reported in the literature (Andreae et al., 2004; Martin et al., 2010; Artaxo et al., 2013). According to Freitas et al. (2005), these aerosols can be transported to the La Plata Basin by wind

circulation and, therefore, can interact with MCSs that form over the basin during the spring. The aerosol impacts include their action as cloud condensation nuclei (CCN). In high concentrations, CCNs can alter the cloud microphysics and, consequently, precipitation processes in both temporal and spatial scales.

## *1.1 Objective*

Based on the arguments put forward, the main questions that guide this study are:

- How does the interaction between aerosols and MCS occur?
- What is the impact of high aerosol concentration in terms of rain?
- What is the effect of high aerosol concentrations in the MCS's dynamics?

The specific objectives of this research are:

- To investigate the observed interactions between Amazon's biomass burning aerosols with the MCSs over the La Plata Basin during the austral spring;
- To use a state of the art microphysical parametrization to study the MCS's evolution;
- To improve the knowledge about microphysical and dynamical mechanisms related to interaction between aerosols and MCSs;
- To develop a mesoscale assimilation framework to improve numerical simulations.

The present document is divided in four chapters. Chapter 2 refers to an analysis of the aerosol impact on precipitation over the La Plata Basin from an observational point of view. Chapter 3 addresses to numerical simulations with idealized CCN profiles for an MCS case observed over the basin. This chapter intends to understand how aerosols affect MCS's dynamics and microphysics. Chapter 4 refers to an assimilation approach, incorporating infrared satellite radiances into the numerical simulation in order to improve the model results. The general conclusions of this study are presented in Chapter 5 as well as suggestions for future work. Finally, Appendix A reveals some modification that were made in the BRAMS–4.3 code and a validation study about the microphysical parametrization implemented in this model during the course of this work.

Chapter 2

# Observational background

The results presented into this chapter were published in the Atmospheric Chemistry and Physics (Camponogara et al., 2014).

**Relationship between Amazon biomass burning aerosols and rainfall over the La Plata Basin**

## *2.1 Introduction*

During the dry season, high concentrations of aerosol particles from biomass burning associated with human activities (mainly agricultural practices and deforestation) have been documented in the Amazon and central Brazil (Artaxo et al., 2002; Freitas et al., 2005; Martins et al., 2009). These aerosols can act as cloud condensation nuclei (CCN), potentially changing the cloud microphysics as well as the radiative properties and lifetime of clouds (Marengo et al., 2002) affecting the Amazon's radiative budget (Lin et al., 2006).

It is well known that aerosols can affect the environment through scattering and absorption of solar radiation (direct effect) and interactions with cloud microphysics (indirect effect). The Intergovernmental Panel on Climate Change (IPCC, 2007) indicates that the uncertainty in aerosol effects on clouds is large compared to other forcings due to human activities. High concentrations of aerosol can modify cloud droplet distribution, increasing droplet concentration while keeping an approximately constant liquid water content (Twomey, 1974). The reduction in cloud droplet size changes the precipitation efficiency and causes an increase in cloud liquid water content and lifetime of the clouds (Albrecht, 1989).

Comparing polluted and clear atmospheres, Rosenfeld (1999) observed that high concentrations of aerosol suppress warm precipitation and that clouds present colder tops than in clear conditions. Through numerical modeling, van den Heever et al. (2006) observed that an increase in aerosol concentration causes an increase in updraft velocity due to latent heat release by condensation. They verify an increase in amounts of rain associated with an increase in GCCN (giant cloud condensation nuclei) and IFN (ice-forming nuclei), whereas an increase in CCN concentration causes a rainfall decrease. High CCN concentrations can also increase ice particle numbers (van den Heever et al., 2006) and, thereby lighting (Albrecht et al., 2011). In the Amazon Basin, Andreae et al. (2004) indicate that clouds formed in regions with a heavy load of biomass burning aerosols have droplet spectra with different properties when compared to clouds formed in clear environments.

Convective clouds are very sensitive to small environmental differences; therefore, it is very difficult to isolate aerosol effects from observations (Wall, 2013). According to Khain et al. (2008), precipitation can be affected by drop condensation and ice deposition (generation), and drop evaporation and ice sublimation (loss), where these variables are perturbed by wind shear, moisture, instability, aerosol, etc. However, atmospheric conditions (e.g., dynamic processes) tend to be more important than aerosol for rainfall production (Jones and Christopher, 2010).

Rodriguez et al. (2010) characterized meteorological conditions associated with thunderstorm and non-thunderstorm days over the city of São Paulo and investigated the pollution influence on them. The thunderstorms were basically regulated by dynamical and thermodynamic characteristics while aerosols did not show any significant effect. Albrecht et al. (2011) observed that large-scale and local environmental thermodynamics processes favored the development of intense thunderstorms over the Amazon at the end of the dry season, with no apparent effect of aerosol loading. During the wet season, however, thunderstorms were preferably observed in periods of high CCN concentrations.

Tao et al. (2007) showed aerosol effects on three different deep convective cloud systems. These authors concluded that higher aerosol concentration can either favor or disfavor the precipitation process, depending on atmospheric conditions. Fan et al. (2007) found that rain delay is more sensitive to relative humidity than to aerosol concentrations and only under conditions of significant moisture, the aerosols can significantly change convection and rain rate. Numerical studies focused on isolated deep convective clouds performed by

Fan et al. (2009) show that in the case of strong wind shear, generally, aerosols suppress convection. This effect is more important in humid air than dry air. Fan et al. (2009) also observed an enhancement in convection by enhanced aerosol concentrations under weak wind shear until an optimum aerosol concentration is reached.

In the present study, the sensitivity of rainfall to aerosol is examined for the La Plata Basin. This basin is the fifth-largest hydrographic basin in the world and the second-largest on the continent, covering Uruguay, Brazil, Argentina, Paraguay and Bolivia. It has a very large hydroelectric potential, with several plants placed on its rivers. Located in one of most densely populated regions in South America, the La Plata Basin sustains domestic consumption and agricultural activities and, thereby represents an important economic factor for the region.

Figure 2.1 from Silva Dias et al. (2009) (c.f., Durkee and Mote, 2010) shows the geographical and seasonal distribution of mesoscale convective systems (MCS) in South America. It may be seen that there is a greater number of MCS during the austral spring and summer over South America, mainly over Paraguay, northern Argentina and southern Brazil. These systems are large cumulonimbus clusters with lifecycles from hours to days and can cause floods, heavy rainfall and severe weather (Velasco and Fritsch, 1987; Fritsch and Forbes, 2001). Zipser et al. (2006) reports that the MCS in the La Plata Basin are seen as the most intense in the world.

Observational studies from Marengo et al. (2002) and Salio et al. (2007) show a narrow flow north of the La Plata Basin and east of the Andes, with a maximum wind speed at an altitude of approximately 2000 m, known as a low-level jet (LLJ). The LLJ is responsible for carrying large heat and moisture content from the Amazon Basin toward the La Plata Basin, feeding the convective systems that develop in the region. Furthermore, Freitas et al. (2005) suggest that the LLJ can transport aerosols from biomass burning in the Amazon and central Brazil to the La Plata Basin in the dry season (austral winter and spring). Thus, in austral spring, the MCS develop under high aerosol loading conditions and, consequently, may be affected by these particles.

Figure 2.2 is a schematic illustration of the present work context. The climatologies for aerosol optical depth (AOD) at 440 nm for the Rio Branco and Alta Floresta stations and rainfall for Asunción, Santa Maria and Buenos Aires are shown. The AOD and rainfall are retrieved by AERONET and TRMM–3B42, respectively. Ji Paraná, Cuiabá, Santa Cruz

and Campo Grande (in red) are also AOD stations; their climatological graphics are not shown in Fig. 2.2, but their data are used in this study. AOD stations show high values between July and December (dry season) with peaks, in September, of about 1.0 for Rio Branco and 1.5 for Alta Floresta. These high values are due to biomass burning activity (Artaxo et al., 2002) and are eventually transported via LLJ to the La Plata Basin (Freitas et al., 2005). Significant amounts of rain are observed in Asunción for most of the year (less in July–September) and for the whole year in Buenos Aires and Santa Maria. Indeed, the aerosols from the biomass burning region may potentially affect the hydrologic balance of the La Plata Basin. However, the question that arises is, if aerosols from biomass burning in the Amazon and central Brazil affect the evolution of MCS in the La Plata Basin, how important is the impact on precipitation? This work proposes to address this question using available data from AERONET and TRMM-3B42 and the NCAR/DOE reanalysis. Section 2 describes the data and method of analysis; in Section 3 a case study is presented to illustrate the large-scale setup of a typical MCS in the region. Results and discussion of the available time series and conclusions are presented in Section 4 and 5, respectively.

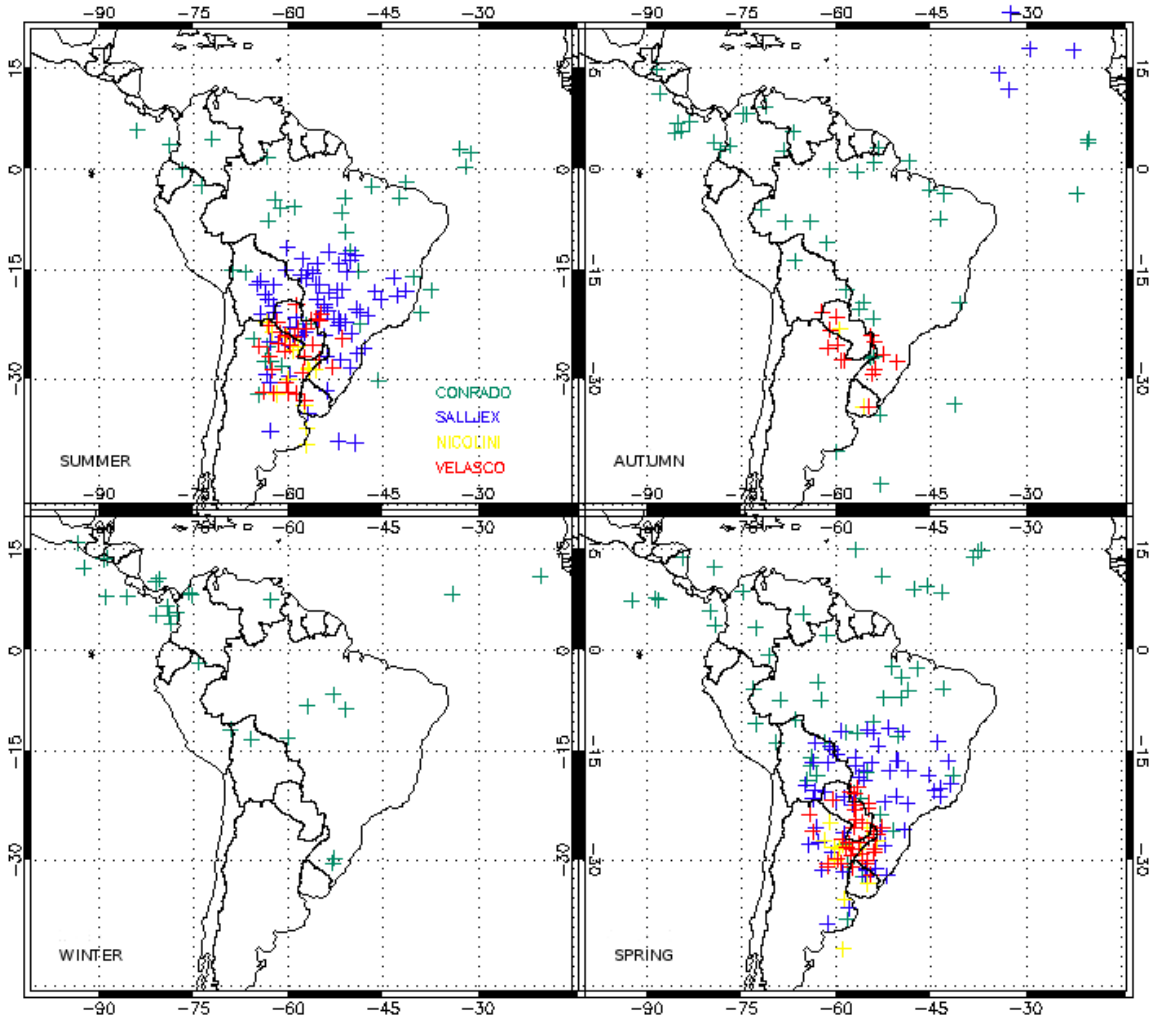


*Figure 2.1:* Climatological distribution of MCSs over South America for each season (Silva Dias et al., 2009). The figure is a compilation of results from Velasco and Fritsch (1987), Conforte (1997), Torres and Nicolini (2002), Salio et al. (2007). The MCSs observed during SALLJEX (Vera et al., 2006) are indicated.

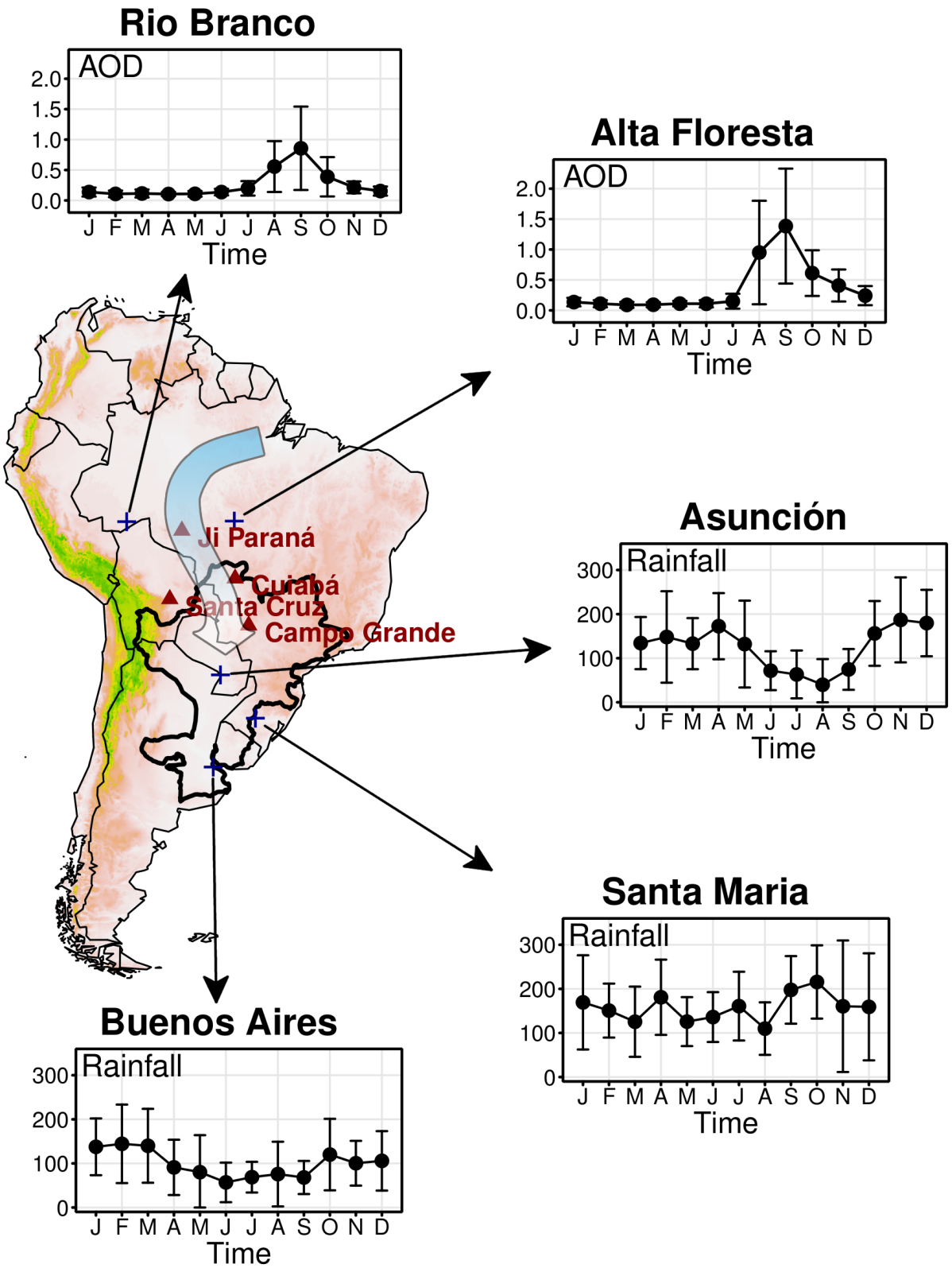


*Figure 2.2:* Schematic illustration about this work context. The graphics are climatologies of AOD for Rio Branco and Alta Floresta AERONET stations, and rainfall estimative from TRMM-3B42 for Asunción, Santa Maria and Buenos Aires cities. Ji Paraná, Cuiabá, Santa Cruz, and Campo Grande AOD stations are located in red.

## 2.2 Data and methods

Three different methods will be presented in an attempt to examine the aerosol effects on rainfall over the La Plata Basin. As described below, this study uses reanalysis to characterize the dynamic and thermodynamic environment, precipitation estimates from satellites and AOD data from AERONET. The data period extends from 1999 to 2012 and the focus is on the dry season and the beginning of the wet season (i.e., September through December).

### 2.2.1 Reanalysis 2

Reanalysis 2 data from NCEP-DOE (National Center for Environmental Prediction – Department of Energy) is used in order to provide large-scale information about the La Plata Basin. These data are an updated version of NCEP-NCAR (National Center for Atmospheric Research) reanalysis, with improvements to the forecast model and data assimilation system (Kanamitsu et al., 2002). It has an updated 6-hourly global analysis series from 1979 to the present and 2.5° x 2.5° grid spacing and is available from `http://www.esrl.noaa.gov/psd/data/gridded/data.ncep.reanalysis2.html`

Winds at 850 hPa are used to define the circulation associated with convective systems. The field of vertical p velocity $\omega$ at 500 hPa is used to indicate the dynamic forcing, with negative $\omega$ indicating upward vertical motion favoring the development of clouds, while positive values indicate subsidence, in principle inhibiting clouds. The mean relative humidity between 700 and 500 hPa (RH) is chosen as an indicator of mid-level moisture in the environment. These variables, vertical p velocity and relative humidity, are averaged over all grid points in the blue box (Fig. 2.3). In order to simplify the nomenclature of these variables, they will just be called $\omega$ (areal average of vertical p velocity at 500 hPa) and RH (areal average of mean relative humidity).

### 2.2.2 TRMM-3B42

The spatial and time variations of rainfall have been obtained from a TRMM (Tropical Rainfall Measuring Mission) satellite, generated by the 3B42 algorithm version 7. These gridded rainfall estimates have been available since 1998 with a 3 h temporal resolution and $0.25° \times 0.25°$ spatial resolution covering global latitudes from 50° S to 50° N (`http:`

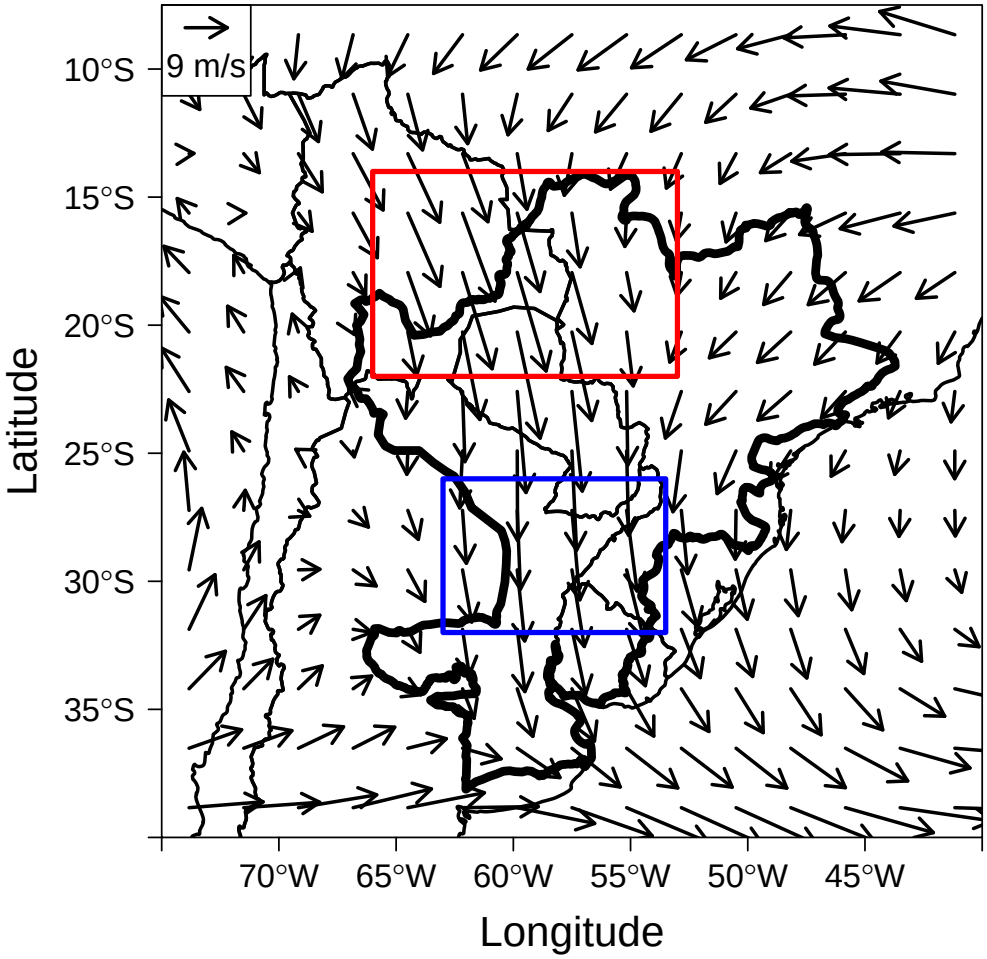


*Figure 2.3:* Mean wind of north flow cases identified by the filtering method. Blue box represents the study area, red box is an auxiliary region for the filter and thick black contour delimits the La Plata Basin.

`//trmm.gsfc.nasa.gov/3b42.html`). According to Su et al. (2008), the precipitation estimates from TRMM-3B42 detect most of the daily precipitation events over the La Plata Basin, although they tend to overestimate heavy precipitation. Rainfall rate in $\mathrm{mm\,day^{-1}}$ and the percentage of rainy grid points over the blue rectangle (rainfall fraction) were computed. A rainy grid point is defined when rainfall rate $> 0.2\,\mathrm{mm\,h^{-1}}$. Areal averages over all grid points in the blue box region (Fig. 2.3) are computed for rainfall rate; only cases with values above $1\,\mathrm{mm\,day^{-1}}$ are considered to be rain events. In the next sections the areal average of rainfall rate of the blue box is hereafter referred to as RR.

### *2.2.3 AERONET*

We used AOD data provided by AERONET (Aerosol Robotic Network), described by Holben et al. (1998) and coordinated by NASA (National Aeronautic Spatial Agency).

AERONET is a global network of sunphotometers that has monitored AOD and aerosol optical properties, under clear sky conditions during the day from directed sun measurements, since 1993. The level 2 product of daily AOD for the wavelength of 440 nm has been used for the sunphotometers at Alta Floresta, Ji Paraná, Rio Branco, Santa Cruz, Campo Grande and Cuiabá. These locations are indicated in Fig. 2.2. AOD has been used as proxy for aerosol concentration following the work of Guyon et al. (2003). They showed that the Amazon Basin biomass burning causes the AOD increases with an increased Ångström coefficient, indicating that in polluted conditions the fine mode of aerosols predominantly contributes to the aerosol concentration.

### *2.2.4 Filtering*

The main assumption of this work is that aerosol from biomass burning is advected from the Amazon and central Brazil to the La Plata Basin under north wind conditions (Freitas et al., 2005). Figure 2.3 shows the average wind field for of all north wind cases from 1999 to 2012 in the transition from the dry to wet seasons; the blue box represents the area under study in the La Plata Basin where rainfall and aerosol relationships are investigated. The red box is located between the blue box and the biomass burning region. A north wind case is defined when the areal average of the meridional wind component over both red and blue rectangles is negative. The cases with wind direction between 30° and 90° over the blue rectangle are discarded to avoid sample contamination from other aerosol sources (e.g., from southeastern Brazil). A further condition to accept a north wind case is that minimum rainfall ($< 3$ mm as areal average over the red box) is observed between the source region and the study region, so that cases where aerosols would be removed by wet deposition before arriving at the blue rectangle are not considered.

The aerosol travel time from the origin to the destination is taken into account by defining a time lag as the time period (in days) that aerosols take to travel from the origin station to the La Plata Basin. For each rain event, lagged correlations between RR and AOD retrieved from 1 up to 5 days before the rain event were computed.

The higher absolute value of lagged correlation for each station is used to define the lag as an indicator of the optimal time interval between aerosol sources and the blue rectangle region (i.e., there is a time lag for each AERONET station). The time lags were also calculated based on average wind at 850 hPa and the distance between the origin and

destination. The results (not shown) were similar, suggesting that the lags were adequate for relating AOD measurements from the Amazon to rainfall in the La Plata Basin.

### *2.2.5 Binplot*

Binplot is an easy tool for exploring the effect of low and high aerosol loadings on the rainfall. This method basically consists in averaging rainfall rate between a bin range of AOD (in this case, 0.1). Then for each AOD range, the average rainfall rate was calculated and plotted for each of the AERONET stations.

### *2.2.6 2-D histograms*

This method is similar to the binplot, but now, besides AOD intervals, intervals of $\omega$ and rainfall fraction will be considered. The rainfall fraction is defined as the percentage of grid points with rainfall rate $> 0.2\,\mathrm{mm\,h^{-1}}$. For each interval of $\omega$, representing a given dynamic pattern, the aerosol effects are investigated.

### *2.2.7 Combined EOF*

According to the methodology contained in Wilks (2006), the combined empirical orthogonal function (EOF) analysis has been used to determine patterns in the joint variation of AOD, rainfall rate, $\omega$ and relative humidity. This procedure has been used as another way of detecting aerosol effects with similar synoptic patterns. EOF calculation was then divided into four steps:

1. A matrix of data was built as

$$\begin{bmatrix} AOD_1 & RR_1 & \omega_1 & RH_1 \\ AOD_2 & RR_2 & \omega_2 & RH_2 \\ \vdots & \vdots & \vdots & \vdots \\ AOD_n & RR_n & \omega_n & RH_n \end{bmatrix}$$

   where, $n$ corresponds to the number of cases selected;

2. The matrix was normalized by subtracting each column by its average and dividing by its standard deviation;

3. The covariance matrix was determined from the normalized matrix;

4. The combined EOF was calculated through the eigen function from R software (`http://www.r-project.org`) that uses the LAPACK (Linear Algebra PACKage) routines.

The results from the aforementioned statistical analysis are described after an overall presentation of a case study along with the general features associated with MCS in the La Plata Basin.

## *2.3 A case study*

An MCS that occurred on 12 September 2007 is used to illustrate the motivation of this work. Figure 2.4 shows AOD values for September 2007 for each station in the Amazon and central Brazil. High AOD values are associated with intense biomass burning (Artaxo et al., 2002), with peaks around 5 for Alta Floresta, 4 for Ji Paraná, 3 for Rio Branco and 2 for other stations (Santa Cruz had no measurements in this month). Looking for days closer to 12 September, it is possible to observe AOD values over 2 for all stations. Then on 12 September, winds from the north indicate a case of transport of high aerosol loadings from the Amazon and central Brazil to the south. This condition provides an environment with high aerosol concentration where the MCS was formed.

Satellite images are shown in Fig. 3.3 for 05:00, 06:45, 10:15 and 14:00 UTC. These images reveal the formation of MCS up to the mature stage; some isolated cells are formed during the first hours and begin to grow and organize, generating a large cloud cluster over northeastern Argentina that reached the mature stage at approximately 14:45 UTC. This system reached brightness temperatures below -70° C and, according to the precipitation estimate from TRMM-3B42, it generated a 6 mm day$^{-1}$ area average and a maximum of 14.4 mm h$^{-1}$ (both over the blue rectangle).

Wind and relative humidity at 850 hPa, mean 700–500 hPa RH (shaded) and $\omega$ at 500 hPa (contour), and wind and divergence at 200 hPa are given in Fig. 2.6. A moist region with RH above 50% is apparent, slightly to the east from a moisture flow observed at 850 hPa (Fig. 2.6a). The $\omega$ field is close to zero over the MCS location, in other words, a neutral condition at 500 hPa. The moisture flow from the north is apparent along with a wind convergence at low levels and upper level divergence at 200 hPa. This condition favors convection, as discussed by Salio et al. (2007). The question posed is whether systems like

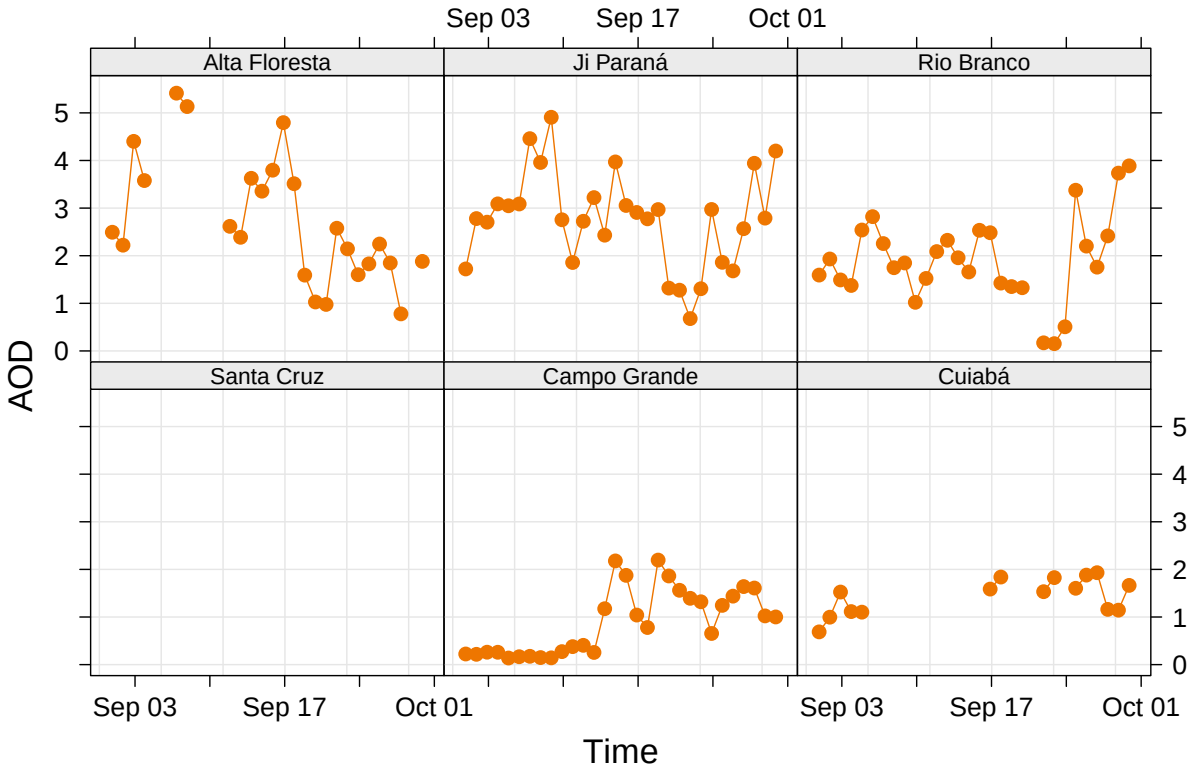


*Figure 2.4:* Daily AOD during September 2007 from AERONET stations. There were not measurements from Santa Cruz station on this period.

this may have been affected by aerosols coming from the north and intruding in low to middle levels into the MCS. The next section will investigate if the aerosols may cause any detectable effect on precipitation over the La Plata Basin, thus influencing the hydrology of the region.

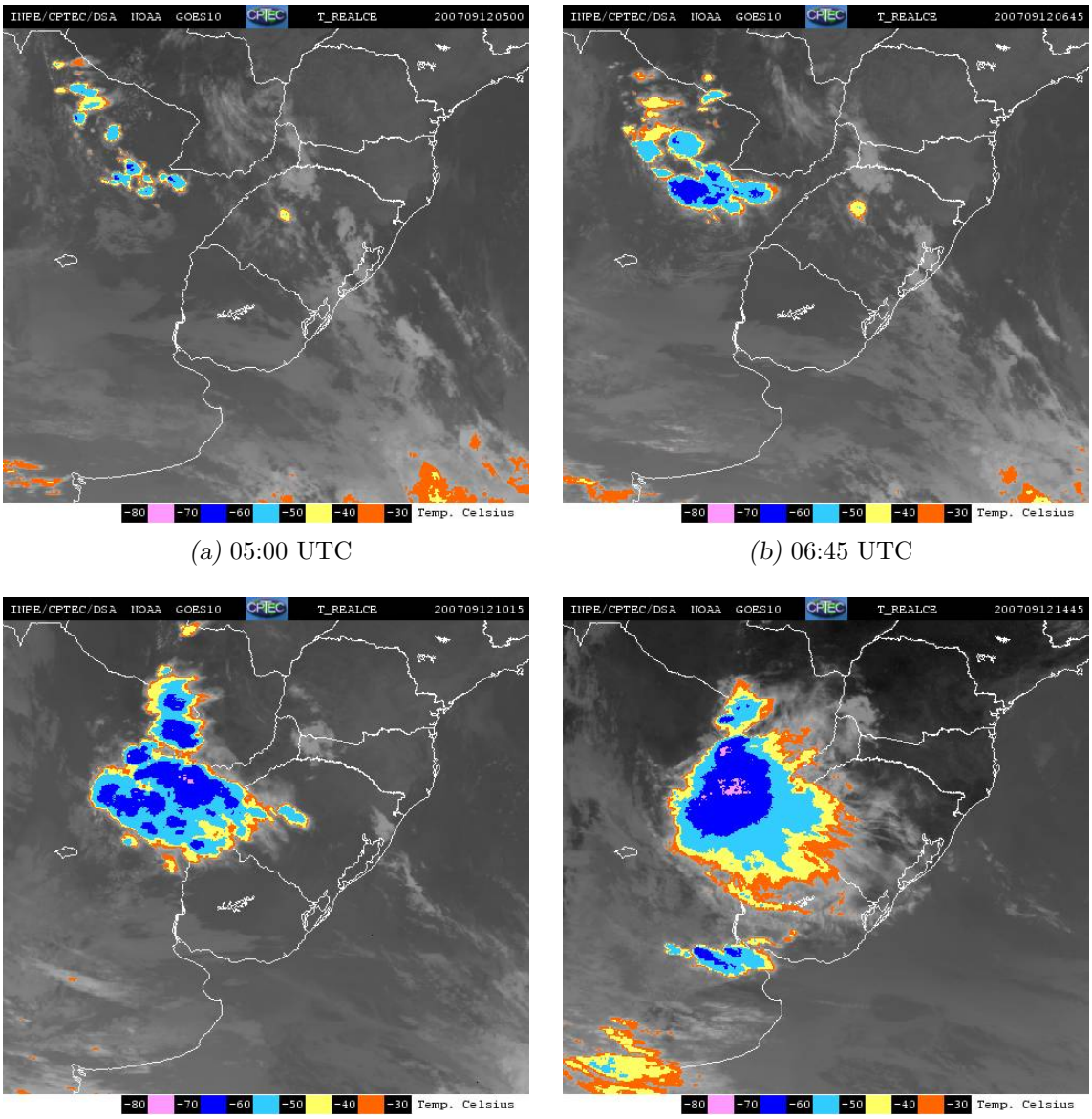


*(a)* 05:00 UTC

*(b)* 06:45 UTC

*(c)* 10:15 UTC

*(d)* 14:45 UTC

*Figure 2.5:* Enhanced infrared satellite images from GOES 11 for a MCS evolution on 12 September 2007 over the La Plata Basin. Colors indicate infrared temperatures. (a) 05:00 UTC, (b) 06:45 UTC, (c) 10:15 UTC, and (d) 14:45 UTC.

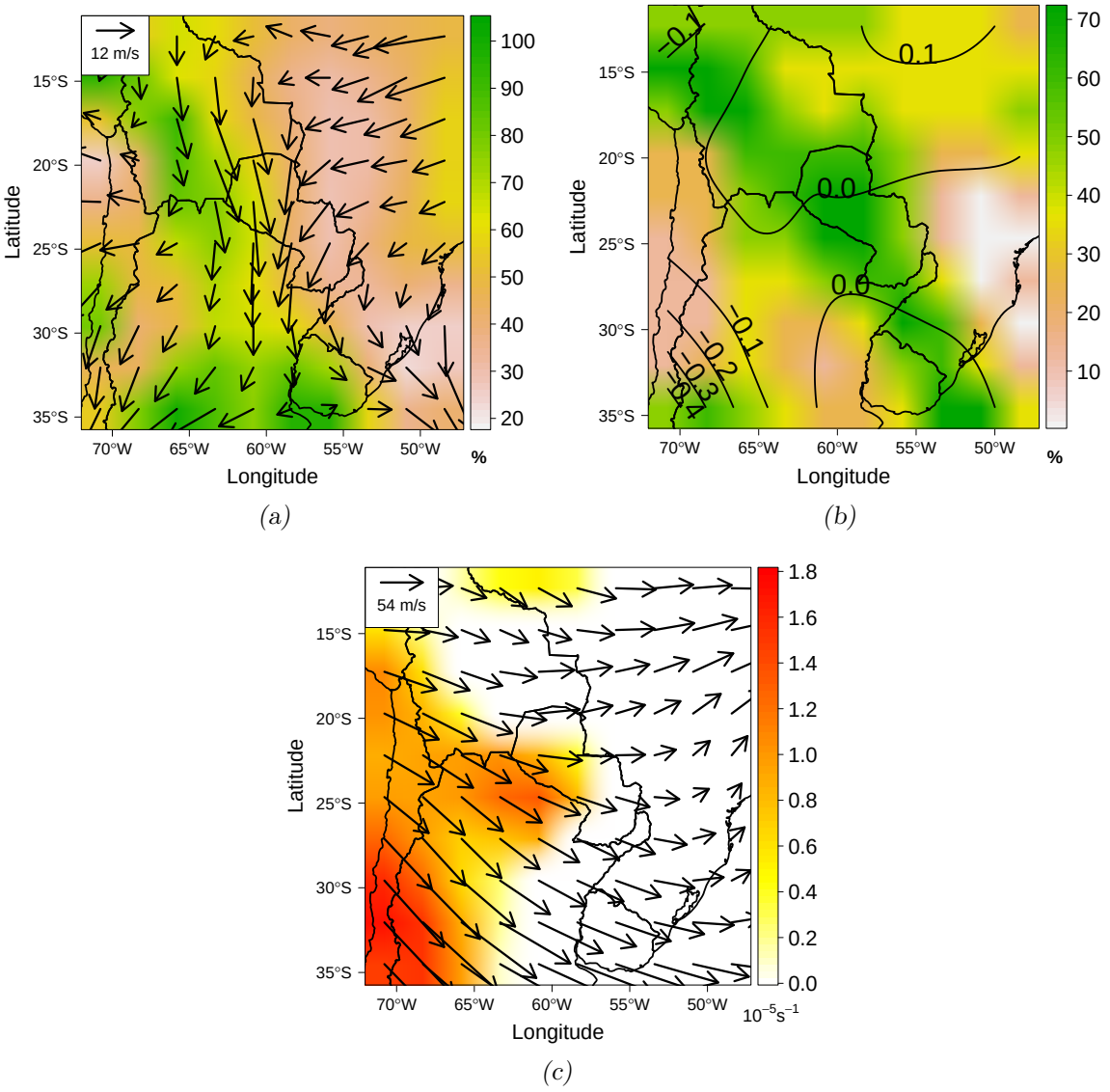


*Figure 2.6:* Large-scale fields on 12 September 2007 at 06:00 UTC: (a) wind and relative humidity at 850 hPa; (b) mean 700-500 hPa relative humidity (shaded) and $\omega$ at 500 hPa (contour); (c) wind and divergence at 200 hPa.

## 2.4 Results and discussion

Comparisons between aerosols and rainfall have been made by considering the best correlated time lag between the path from the biomass burning region to the La Plata Basin, as described in Sect. 2.2.4. The total number of analyzed cases is 150 from Alta Floresta, 33 from Ji Paraná, 109 from Rio Branco, 45 from Santa Cruz, 78 from Campo Grande and 78 from Cuiabá. Figure 2.7 shows the rainfall rate as a function of AOD. It can be seen that rainfall decreases as AOD increases, which means higher aerosol load is associated with lower precipitation. This pattern occurs at all stations and it is more significant for AOD below 1, but is it really related to aerosol loads? Or may it occur due to another forcing? Another feature of Fig. 2.7 is an indication of a bimodal distribution of rainfall with AOD; the reasons for that are unknown at this point. The local maxima may be due to different environmental conditions associated with rainfall. We further examine this in the following paragraphs when we separate rainfall according to the dynamic forcing represented by $\omega$.

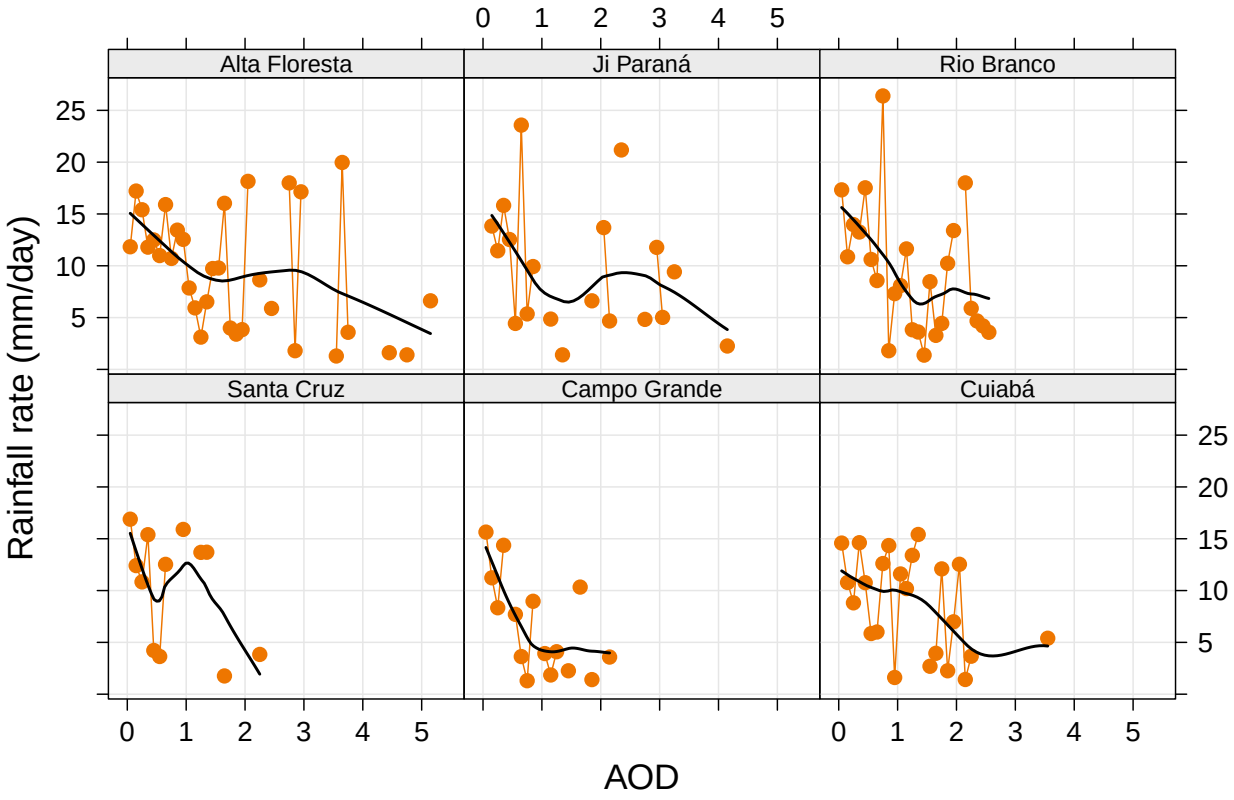


*Figure 2.7:* Rainfall rate binned by AOD range of 0.1 for each AERONET station for all selected cases (see Sect. 2.2.4) during the months of September-October-November-December of 1999-2012.

Figure 2.8 shows the average rainfall rate (shaded boxes) as a function of rainfall fraction and AOD. Differences in rainfall rates between rainfall fraction and AOD ranges are immediately apparent. Below 40 % there is no contrast between the shaded boxes; in other words, it is not possible to detect the aerosol effect. For values above 40 %, a strong contrast between the boxes can be seen, indicating a possible impact of aerosols on rainfall. In other words, the effect of aerosol loading on rainfall is statistically evident in systems capable of generating large areal precipitation over the basin through a 2-D histogram method. However, patterns cannot be identified clearly, probably because there are other dominant forcings.

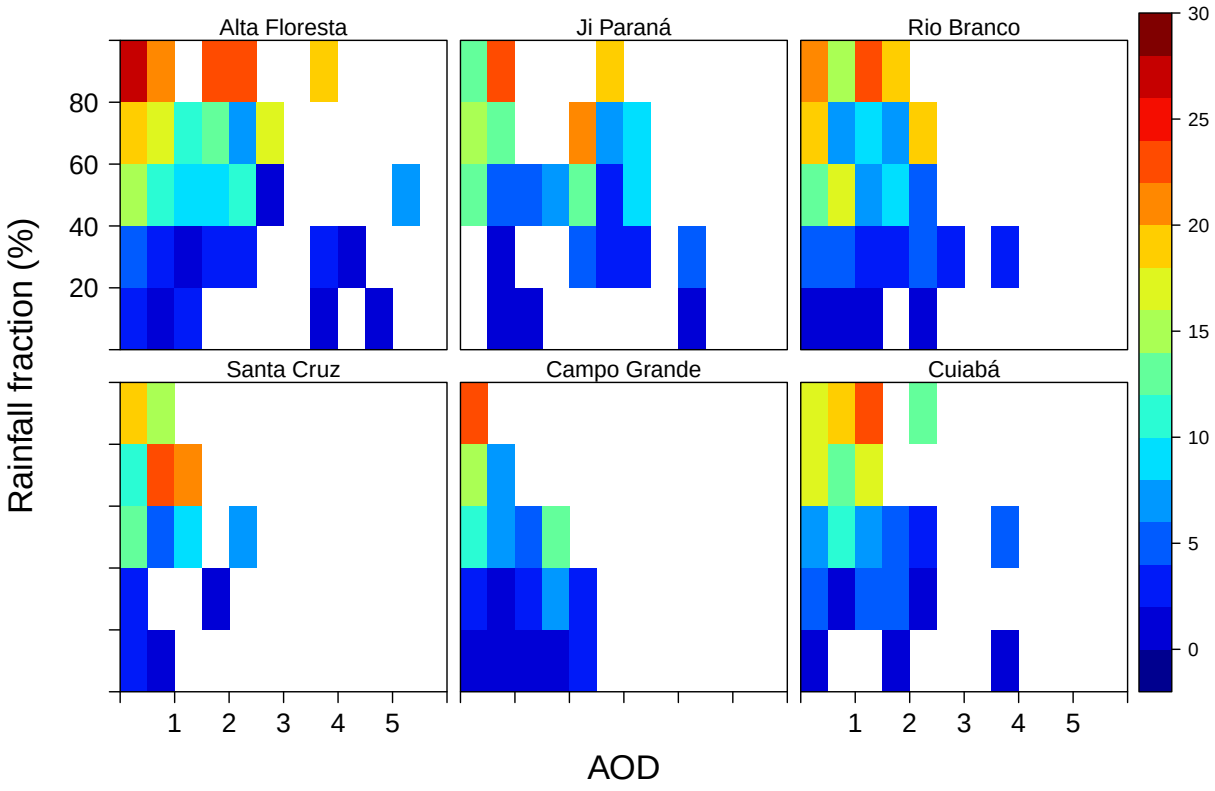


*Figure 2.8:* Two-dimensional histogram of average rainfall rate for each AERONET station for all selected cases (see Sect. 2.2.4) during the months of September-October-November-December of 1999-2012. Colors indicate average rainfall rate for each bin of rainfall fraction and AOD.

Dynamics is one of most important forcings to generate rain and, for this reason, it is very difficult to recognize aerosol effects that are usually secondary. In this context, dynamic patterns were separated using the two-dimensional histograms (similar to Fig. 2.8). Figure 2.9 shows the rainfall rate as a function of $\omega$ and AOD. $\omega$ (the vertical p velocity at 500 hPa) is used to identify the large-scale dynamic forcing. Large values of negative

$\omega$ are associated with enhanced upper motion that favors the widespread development of rainfall. In the absence of this forcing, low values of $\omega$ represent cases where the large-scale dynamics does not force rainfall. Differences between strong and weak $\omega$ (below and above -0.25 $\mathrm{Pa\,s^{-1}}$, respectively) are easily observed for all stations. AOD dominates the precipitation for low $\omega$ values; conversely, vertical velocity dominates the precipitation under high $\omega$ values. Thus, aerosol effects are dominant under weak dynamic forcing conditions, inhibiting rainfall. Another feature of Fig. 2.9 is a bimodal distribution (like in Fig. 2.7) associated with large rainfall amounts and intense dynamic forcing. This pattern explains the nature of the two modes identified in Fig. 2.7 that are due to the large-scale upward motion.

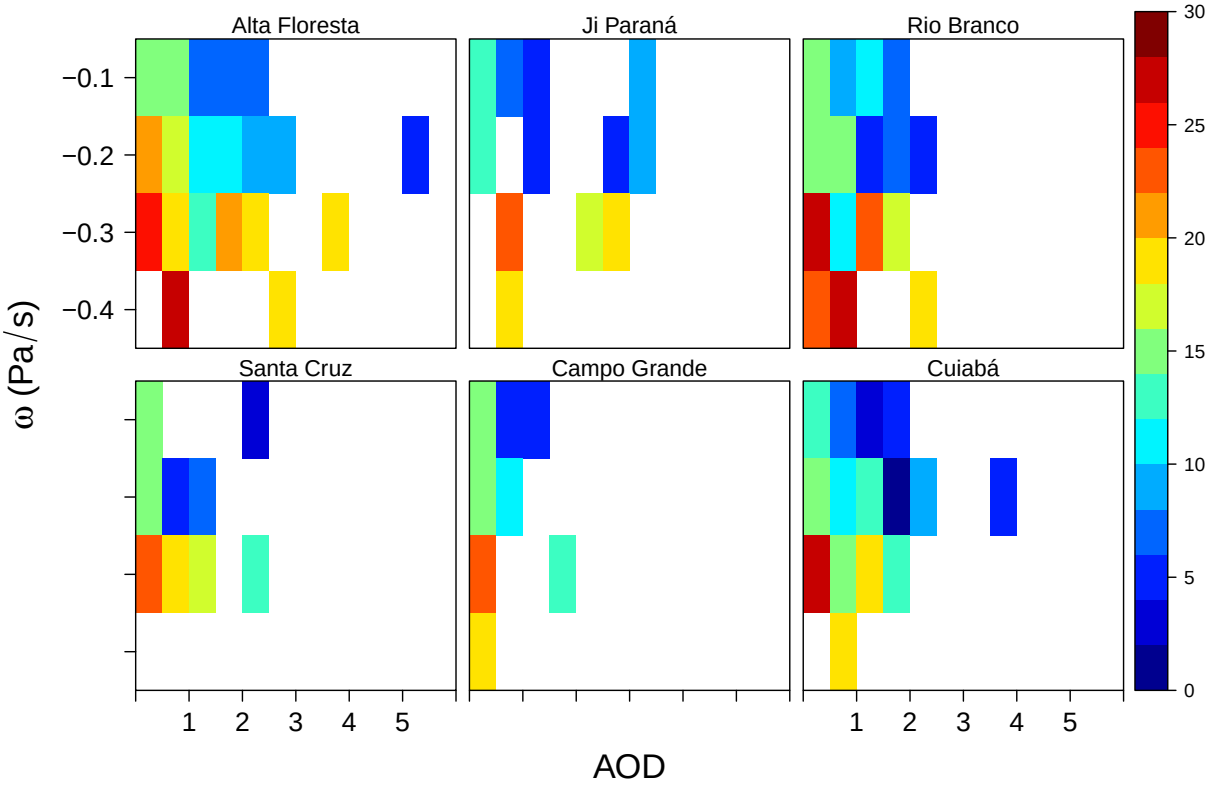


*Figure 2.9:* Two-dimensional histogram of average rainfall rate for each AERONET station for all selected cases (see Sect. 2.2.4) during the months of September-October-November-December of 1999-2012. Colors indicate average rainfall rate for each bin of $\omega$ and AOD.

Combined EOFs were calculated in another attempt to observe the aerosol effect and reinforce the previous results. The combined EOF analysis is used to identify variability patterns from a group of variables. In other words, the eigenvectors detect linear relationships between AOD, RR, $\omega$, and RH. Table 2.1 shows the variance explained by the

first and second eigenvectors and the total explained by these two. The first EOF explains around 43 % of the variance of the data set for all AOD stations and the second EOF 31 %; together these eigenvectors represent more than 70 % of the data variance explained. The other two EOFs are not shown since they explain a lower portion of the variance. Satellite images for the cases detected by the EOF time series were examined (not shown). It was observed that about 70 % of selected rain events are associated with MCS. The other 30 % are basically related to cold fronts and extratropical cyclones with embedded convective systems.

*Table 2.1* - Variance explained by the first and second EOFs and the variance explained by these two EOFs for each AOD station for all selected cases (see Sect. 2.2.4) during the months of September-October-November-December of 1999-2012.

| | $R_1^2(\%)$ | $R_2^2(\%)$ | $R_1^2 + R_2^2$ |
|---|---|---|---|
| Alta Floresta | 41 | 31 | 72 |
| Ji Paraná | 43 | 30 | 73 |
| Rio Branco | 42 | 34 | 76 |
| Santa Cruz | 45 | 30 | 75 |
| Campo Grande | 41 | 31 | 72 |
| Cuiabá | 43 | 30 | 73 |

EOFs and their respective components AOD, RR, $\omega$ and RH for each AOD station (in colors) are shown in Fig. 2.10; values represent perturbations with respect to the average. Looking at $e_1$, it is possible to verify that this eigenvector detects a pattern with small AOD anomalies and large anomalies of RR, $\omega$ and RH, reflecting a pattern basically independent of AOD. The physical interpretation of the first eigenvector is that stronger large-scale upward motion and moister mid-level atmosphere are associated with larger amounts of rainfall. For a moister mid-level environment, the entrainment into the cloud generates less evaporation, thus potentially affecting the rainfall production.

The second EOF detects large positive anomalies of AOD associated with large negative anomalies in rainfall for small anomalies of $\omega$ and RH. For this pattern, the interpretation is that $\omega$ and RH are average, while large AOD is associated with rainfall suppression. The results from the EOF analysis agree with Figs. 2.7 and 2.9 in that the dynamic component appears as the main rainfall forcing and the aerosol loading as the second one. The first EOF is related to dynamic forcing, whereas the second EOF seems to represent the aerosol forcing. Jones and Christopher (2010) also used EOF analysis to identify possible

interactions between aerosols and precipitation in the Amazon Basin. Their results also detected two patterns, one related to atmospheric conditions favorable to rainfall and the other linked to the aerosol forcing, and associated with rainfall inhibition.

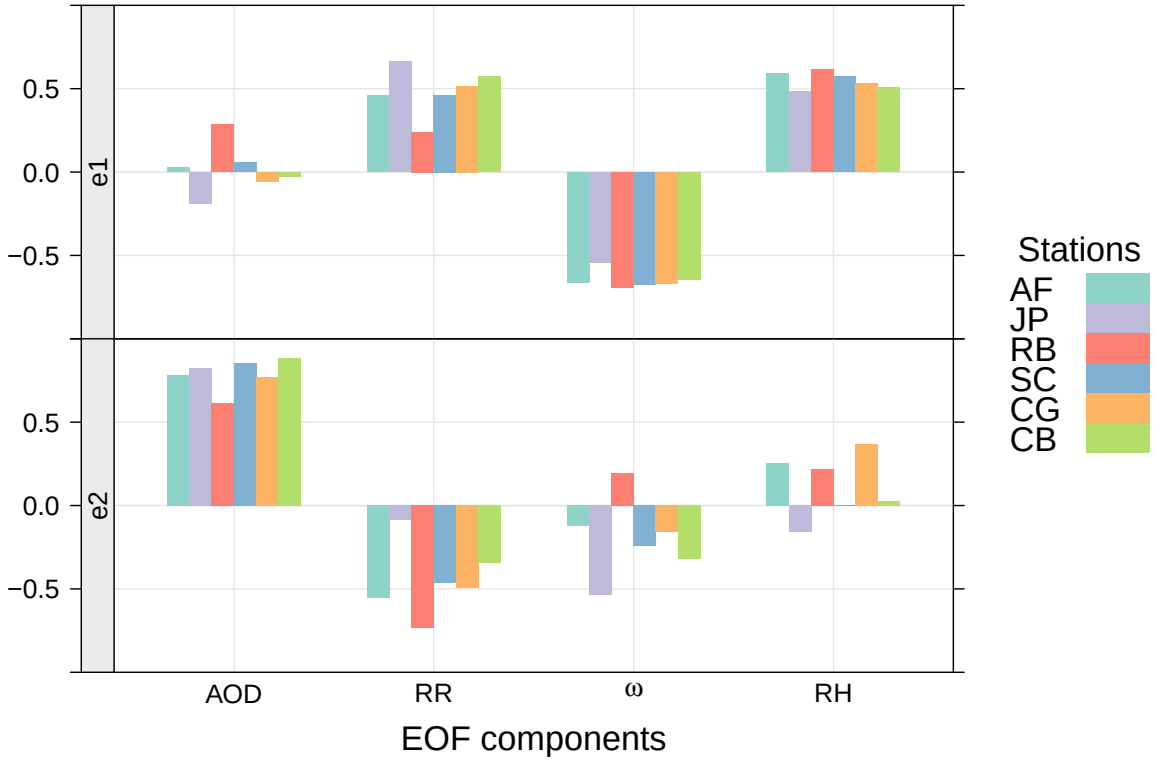


*Figure 2.10:* EOFs and their components AOD, RR, $\omega$, and RH for each AERONET station for all selected cases (see Sect. 2.2.4) during the months of September-October-November-December of 1999-2012. Colors indicate the stations of Alta Floresta (AF), Ji Paraná (JP), Rio Branco (RB), Santa Cruz (SC), Campo Grande (CG), and Cuiabá (CB).

## 2.5 Conclusions

Previous works ((Andreae et al., 2004; Freitas et al., 2005) indicate the aerosol can be transported by the LLJ from the Amazon and central Brazil biomass burning regions to the La Plata Basin. Based on these studies we used three statistical tools in an attempt to isolate aerosol effects from biomass burning on rainfall over the La Plata Basin. The period analyzed was 1999–2012 during the dry season and the beginning of the wet season (September–December) using data from AERONET, TRMM-3B42 and reanalysis 2.

Generally, results show that high aerosol concentrations tend to suppress precipitation

for the three statistical methods used. It was only possible to detect the aerosol effect on rainfall fractions above 40 % (through 2-D histograms). When absolute values of $\omega$ are large, aerosol effects are not detected. However, for $\omega < -0.25\,\mathrm{Pa\,s^{-1}}$ (weak dynamic forcing), high aerosol concentrations tend to suppress rainfall.

A bimodal distribution was observed between rainfall and AOD through the binplot (Fig. 2.7) and a 2-D histrogram (Fig. 2.9). This means that two local maxima of rainfall rate were present under two different AOD regimes. These peaks are generally associated with strong dynamic forcing. In other words, stronger large-scale upward motion causes larger rainfall amounts, which contrasts with the aerosol effects that are associated with rainfall suppression.

The first two patterns from the EOF analysis explain more than 70 % of the data variance, corresponding to about 43 % for the first EOF and 31 % for the second one. The first eigenvector identified the dynamic forcing in which strong vertical velocities represented by $\omega$, moist atmosphere at medium levels and aerosol concentration near the average cause rain above the average. $e_2$ detected the aerosol forcing in which high aerosol loadings in a slightly moist atmosphere and below average $\omega$ were associated with rainfall suppression. These results show that the dynamic component is the main forcing for rain production, while aerosols have a role in inhibiting the rainfall under weak large-scale forcing.

The aerosol rain suppression in MCS is certainly very complex. Simpler cases such as single cloud studies indicate possible processes to take into account. However, the dynamics of large MCS involve multiscale interactions (from cloudscale to mesoscale to large-scale) over a period of several hours. In the particular case of the MCS over the La Plata Basin, the system is apparently affected in its cloud microphysics, with a steady flow of aerosol coming from biomass burning regions to the north. Unfortunately, there are limitations and uncertainties in the statistic tools and data used here that could potentially affect the conclusions. Thus, it is necessary to address this issue further with other tools, such as numerical experimentation, to understand the mechanisms involved and to reduce the uncertainty in the results.

Chapter 3

# Numerical experiments with CCN concentrations

The results presented into this chapter were submitted to the Atmospheric Chemistry and Physics Journal.

**Biomass burning CCNs enhance the dynamics of a Mesoscale Convective System over the La Plata Basin: a numerical approach**

## *3.1 Introduction*

The Amazon Basin exhibits a huge contrast in terms of aerosol concentration between wet (January-June) and dry (July-December) seasons (Andreae et al., 2004; Martin et al., 2010; Artaxo et al., 2013). Aerosol loading is typically about hundreds of particles per $cm^3$ in the wet season with a similar pattern and microphysical characteristics to those found in remote ocean regions. For this reason, the Amazon region has been referred to as "green ocean"(Williams et al., 2002). However, during the dry season, when the Amazon Basin faces a polluted regime with tons of particles being released into the atmosphere by biomass burning, the number of aerosols increases drastically, close to one order of magnitude. The majority of these emissions are due to anthropogenic activities regarding agriculture and deforestation (Reinhardt et al., 2001; Morton et al., 2008). According to Freitas et al. (2005), these aerosols can be transported by the wind to other regions such as the La Plata Basin.

The La Plata Basin is one of most intense convective regions in the world (Zipser et al., 2006) with significant lightning events (Albrecht et al., 2016). This region is dominated by mesoscale convective systems (MCSs) during the spring and summer seasons (Velasco

and Fritsch, 1987; Conforte, 1997; Torres and Nicolini, 2002; Vera et al., 2006; Salio et al., 2007; Durkee and Mote, 2010), which have an important role in the La Plata Basin's hydrological cycle, being responsible for approximately 90% of the total rainfall over the basin (Nesbitt et al., 2006). These systems may produce strong winds, floods, heavy rain and hail (Velasco and Fritsch, 1987; Fritsch and Forbes, 2001).

Mesoscale convective systems normally result from the combination of certain ingredients such as atmospheric instability, mesoscale circulation, the weak midlevel short-wave trough and low level jet (LLJ). Mesoscale circulations contribute to air parcels reaching the free convection level; atmospheric instability favors convection development; the midlevel short-wave trough intensifies low level convergence; and the LLJ brings moisture and heat from the Amazon (Fritsch and Forbes, 2001; Silva Dias et al., 2009). Moreover, the LLJ may also advect huge amounts of aerosols from the Amazon to the La Plata Basin during the dry and dry to wet transition seasons (Freitas et al., 2005), which may interact with MCS in different ways.

Aerosols can absorb and scatter solar radiation (direct effect) leading to a decrease in the surface temperature (semi-direct effect) or even a stabilization of the atmosphere by warming the surrounding air (Eck et al., 1998; Koren et al., 2004, 2008). Part of the aerosols can have affinity with water and act as cloud condensation nuclei (CCN), this being known as the indirect or microphysical effect. In addition, CCNs can increase the warm cloud albedo for a constant liquid water content (Twomey, 1974) and change the lifecycle and the warm rain triggering mechanism (Albrecht, 1989; Martins et al., 2009).

As mentioned in the literature (Rosenfeld, 1999; Rosenfeld et al., 2008; van den Heever et al., 2006; Carrió and Cotton, 2011; Carrió et al., 2014; Zhou et al., 2016), the aerosol microphysical effect is related to the number of cloud droplets that are nucleated. For example, a polluted atmosphere (large number of CCN particles) produces more cloud droplets than a clean one if there is enough water vapor to support a larger population. This effect leads to a narrower cloud droplet size spectrum filled with smaller cloud droplets, which delays the collection growth onset. Hence, more cloud droplets are thrust into freezing levels, becoming supercooled. Finally, the supercooled droplets may either be collected by ice particles (riming process) or freeze homogeneously, producing graupel and eventually hail, and ultimately affecting rainfall at the surface.

By using the Brazilian development on the Regional Atmospheric Modeling System

(BRAMS), Martins et al. (2009) investigated the aerosol effects on cloud microphysical processes during the end of the Amazon dry season and observed significant impacts on precipitation process in spatial and temporal dimensions. The maximum liquid water values increased for high aerosol concentrations in all runs. By using a combination of different observational data sets, Gonçalves et al. (2015) noted that a high concentration of aerosol in the Amazon Basin may increase the cloud lifetime during the dry season as well as convection strengthening.

The invigoration of convective cells due to a CCN increase is usually explained by the latent heat release increase caused by riming enhancement (van den Heever et al., 2006; Rosenfeld et al., 2008). However, CCNs also can affect cold pool and wind shear interaction, modulating the convection strength (Fan et al., 2009). When cold pool and wind shear strengths are balanced, convective cells tend to become more upright, and, consequently, more intense (Rotunno et al., 1988). Environments with high CCN concentrations may invigorate the convection by weakening the cold pool under weak shear conditions (Fan et al., 2009; Lebo and Morrison, 2014). Polluted atmospheres favor the development of fewer but larger raindrops, hence, evaporation cooling is reduced, which decreases the cold pool strength. On the other hand, a combination of strong wind shear with high aerosol loadings may overcome the latent heat release and, as a consequence, weaken convection. This occurs because stronger cold pools are needed to keep the updraft cells more upright under strong wind shear conditions, as shown by Rotunno et al. (1988).

Lebo and Morrison (2014) also observed different responses in precipitation when wind shear is intensified under polluted conditions. As wind shear increases, aerosols tend to generate more precipitation due to greater condensation. In contrast, precipitation was significantly reduced in the strongest wind shear scenario. This effect was caused by an excessively tilting downshear of updraft cells that led to raindrops to fall ahead of the gust front and thus to immediately evaporate.

Through a bidimensional cloud resolving model, Tao et al. (2007) examined the aerosol effects in three distinct deep convection cases from regions with different environments: sea breeze convection in Florida, USA; the squall line in Kansas, USA; and the tropical mesoscale convective system over the Pacific Ocean. For all cases, rainfall suppression was observed under high CCN concentrations during the initial stages of the systems. Conversely, in the mature stage, rainfall underwent suppression only over Kansas, being little

affected over Florida and intensified over the Pacific. These results suggest that evaporation cooling plays an important role in this phenomenon since stronger (weaker) evaporation was observed in polluted environments under moister (drier) conditions. Stronger evaporation favors more intense downdrafts and cold pools, which, depending on atmospheric shear, may intensify the convection and then increase the precipitation.

According to Fan et al. (2007), large aerosol loadings are capable of greatly changing the convection strengthening and rain rate in environments with a high moisture content. On the other hand, Carrió et al. (2014) observed a stronger effect of CCN on hail under low level drier conditions, which favor higher cloud bases, and which do not contribute to warm rain processes, allowing more cloud droplets to become supercooled. As a result, the riming process is enhanced, and hail mass is increased. However, a further CCN increase may generate much smaller droplets, causing riming inhibition and, therefore, homogeneous freezing enhancement.

In summary, MCSs can be affected by aerosol and environmental conditions. Aerosol effects on MCSs can also be influenced by the environment, making the study of this phenomenon even more complex. As mentioned by Wall (2013), Camponogara et al. (2014) and Gonçalves et al. (2015), separating aerosol effects from environmental forcing is a great challenge. Therefore, despite the limitations, numerical models appear to be an important tool to understand the aerosol-cloud-precipitation processes, as pointed out by Tao et al. (2012). The present study is one of the first that seeks to understand the microphysical effects of biomass burning aerosols from the Amazon Basin on mesoscale convective systems over the La Plata Basin. In order to do so, we performed numerical simulations varying CCN number concentration for an MCS case over the La Plata Basin during the spring season. Section 3.2.1 gives a brief description of the atmospheric model, focusing on its microphysical parametrization, and Section 3.2.2 describes how the numerical experimentation was performed. Finally, results and discussion are presented in Section 4.3, followed by conclusions in Section 4.4.

## 3.2 Methodology

### 3.2.1 Atmospheric model

Originally developed from RAMS (Regional Atmospheric Modeling System), the Brazilian development on the Regional Atmospheric Modeling System (BRAMS), version 4.3, is used in this study. RAMS was created by a research group from Colorado State University, joining three numerical models as reported by Cotton et al. (2003): a cloud/mesoscale model (Tripoli and Cotton, 1982); a hydrostatic version of this cloud model (Tremback, 1990); and a sea breeze model (Mahrer and Pielke, 1977). According to Cotton et al. (2003), RAMS, as well as BRAMS, is a non-hydrostatic model with several options related to its physics, which can be set according to the experiment type. It is possible to set different grid spacing using multiple grids, which can be nested either 1-way (coarser grids communicating with finer grids) or 2-way (both coarser and finer grids communicating with each other). Detailed description of the current BRAMS version may be seen in Freitas et al. (2017).

BRAMS has been updated with the two moment microphysical bulk scheme currently used in RAMS, version 6.0, which predicts number concentration and mixing ratio for eight hydrometer species: cloud, drizzle, rain, pristine ice, snow, aggregates, graupel and hail. All hydrometeor categories have their own size distribution represented by a generalized gamma function (Walko et al., 1995; Meyers et al., 1997; Cotton et al., 2003; Saleeby and Cotton, 2004, 2008).

Together, cloud and drizzle categories represent a bimodal distribution of cloud droplets, as reported by Hobbs et al. (1980), and often observed in nature, where drizzle is basically large cloud droplets. The larger droplets function as an intermediate state between cloud droplets and raindrops, slowing the time that the cloud droplet takes to grow into raindrop size in a more realistic way. Pristine ices are primary ice crystals and grow only by vapor deposition. Once these ice crystals reach sizes greater than 100 $\mu$m they become snow. Aggregates are produced by collision and coalescence of pristine ice and snow species. Only snow and aggregate categories can be converted to graupel. The high-density ice particles such as frozen raindrops and hailstone are represented by the hail category.

Cloud number concentrations are predicted by consulting a look-up table that was

pre-computed through a bin-parcel model. This variable is a function of the air temperature, vertical velocity and the CCN number of particles. Drizzle number concentration can be produced by cloud droplet self-collection or Giant CCN activation (such as CCN activation). Pristine ice number concentration is predicted by either IN activation, which depends on ice supersaturation, or homogeneous freezing. The aerosol concentrations can be defined as either a homogeneous (single vertical profile) or a heterogeneous field and can be advected and diffused.

The riming processes are computed by using a binned approach, which tends to be more accurate owing to considering an individual collection efficiency for each bin instead of taking just one collection efficiency for the entire gamma distribution (Saleeby and Cotton, 2008). Bin sedimentation, sea salt and dust treatment and an algorithm for heat and vapor diffusion, without requiring iterations, are other examples of implementations currently present in the microphysical scheme (Cotton et al., 2003).

### *3.2.2 Experiments design*

Numerical experiments were performed with BRAMS, version 4.3, for an MCS case observed over the La Plata Basin on 21 September 2010 (Figure 3.3). We use three 1-way nesting grids with 16 km, 4 km and 2.5 km of grid spacing, respectively from the course to finest one. All grids are centered over the La Plata Basin, as can be seen in Figure 4.2, and their domain sizes are 4800×5120 km (grid 1), 1400×1416 km (grid 2) and 1250×1250 km (grid 3). Figure 4.2 also shows a shaded area related to the La Plata Basin topography elevation. The vertical grid spacing varies from 100 m to 600 m, with a ratio of 1.1, whereas the top of domain extends to near 20 km, with 45 vertical levels. All experiments started on 20 September 2010 at 12:00 UTC. Table 3.1 shows the other important settings used in the experiments.

We performed four experiments with different vertical profiles of CCN concentrations, based on the work of Freitas et al. (2005) (Figure 3.2). The CCN profiles have their peaks at 2.5 km height, where CN-Low, CN-Mid, CN-High and CN-ExtHigh have 500, 1200, 1800 and 2800 particles per centimeter, respectively. Above 4.9 km, the CCN concentrations were considered 100 $cm^{-3}$. These profiles were also nudged on the northern boundary of the finest grid domain, covering five meridional grid cells in order to maintain a constant aerosol input into the grid, as observed in northerly low level flow events (Freitas et al.,

2005).

All the experiments were initialized heterogeneously by using the third generation of reanalysis from the National Centers for Environmental Prediction (NCEP) Climate Forecast System Reanalysis (CFSR). These data sets have 37 vertical levels, 4 times a day (00, 06, 12, 18 UTC), horizontal grid spacing of 0.5°× 0.5° and are available for the period from 01/01/1979 up to 01/01/2011. Moreover, the model also was fed with the Normalized Difference Vegetation Index (NDVI), heterogeneous soil moisture, sea surface temperature weekly averaged, topography, land use and soil texture, downloaded from the *Centro de Previsão do Tempo e Estudos Climáticos* of *Instituto Nacional de Pesquisas Espaciais* (CPTEC/INPE) through the link `http://brams.cptec.inpe.br`.

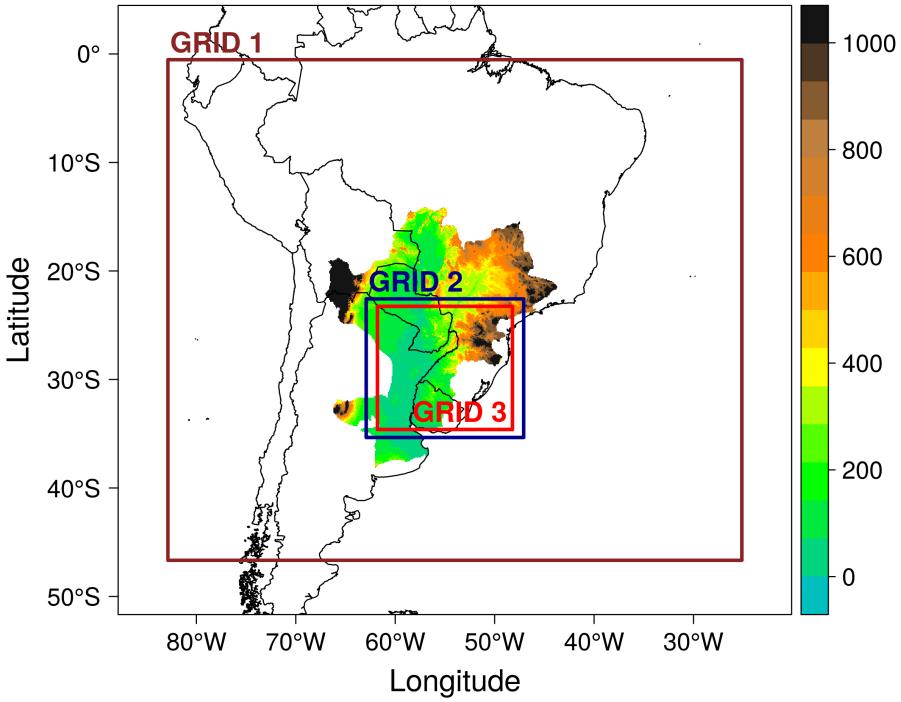


*Figure 3.1:* Model domain for 16 km (brown box), 4 km (blue box) and 2.5 km (red box) of grid spacing. The topography elevation of the La Plata Basin is shaded.

*Table 3.1* - BRAMS main configuration.

| | |
|---|---|
| Number of points for lateral boundary nudging | 5 |
| Nudging time scale for lateral boundary | 1800 s |
| Nudging time scale for the top of domain | 10800 s |
| Lateral boundary condition | Klemp and Wilhelmson (1978) |
| Shortwave/Longwave radiation parametrization | Chen and Cotton (1987) |
| Turbulence parametrization | Mellor and Yamada (1982) |
| Convective parametrization (activated only for grid 1) | Grell (1993) |

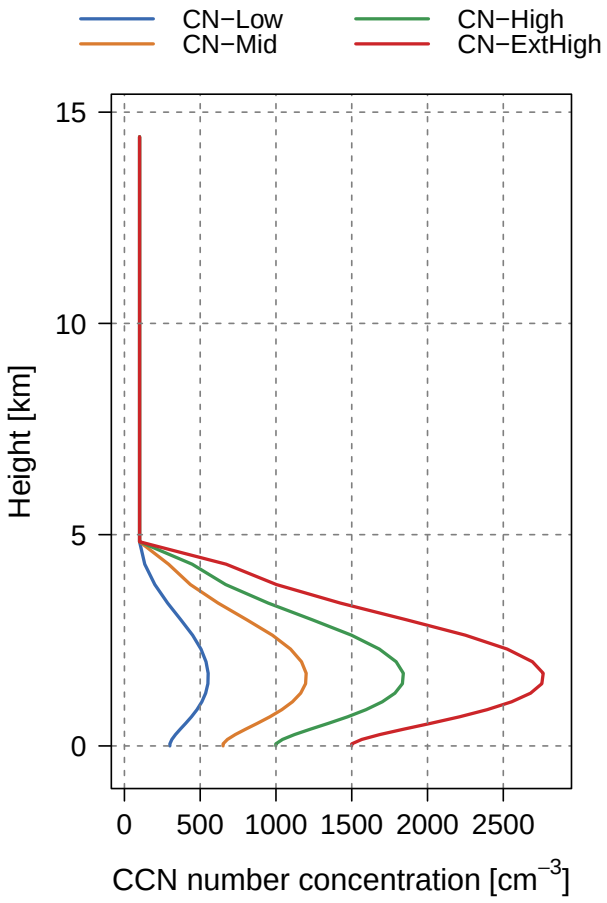


*Figure 3.2:* Vertical profiles of CCN concentrations used to initialize the numberical model.

## 3.3 Results

Numerical experiments varying CCN concentrations (Figure 3.2) were performed by using the BRAMS-4.3 model for the MCS case observed over the La Plata Basin on 21 September 2010. This mesoscale system was observed by the satellite GOES 12, whose images can be visualized in Figure 3.3. The first cells started over northeast of Argentina near 06:00 UTC. In the next few hours these convective cells begin to grow and become organized, forming a large cloud shield at 08:30 UTC. Near 11:00 UTC, the MCS reaches its mature stage, covering the South of Brazil almost entirely.

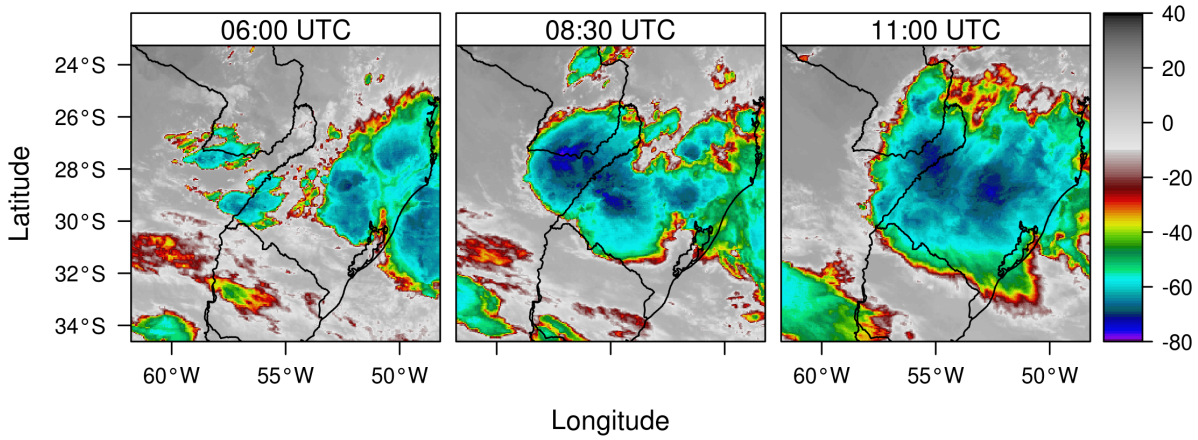


*Figure 3.3:* Enhanced infrared satellite images from GOES 12 for an MCS case observed over the La Plata Basin on 21 September 2010. Colors indicate infrared temperatures.

Synoptic fields are made from CFSR (Figure 3.4), used as initial and boundary conditions in BRAMS. Sea level pressure (contour lines) and thickness (shaded) are given by Figure 3.4a. The thickness refers to the difference between the geopotencial heights of the pressure levels of 500 hPa and 1000 hPa. This variable is proportional to the mean temperature in the layer between 500–1000 hPa. A trough, aligned meridionally, can be seen over the Argentina coast with a strong temperature gradient ahead (Figure 3.4a). Furthermore, it is possible to note a warm air mass over the La Plata Basin, where a peak of thickness is found over northwest of Paraguay, the north of Argentina and the south of Bolivia, which is followed by a low pressure displaced southward (Figure 3.4a). Figure 3.4b shows the wind field (vectors) and specific humidity (shaded) at 850 hPa. A meridional flow is seen advecting moisture (Figura 3.4b) and heat (Figura 3.4a) from the Amazon Basin to Paraguay, northern Argentina and southern Brazil. The trough observed in Figure 3.4a

also appears in the wind field at 850 hPa as well as the South Atlantic High. Geopotential height (contour) and vertical p velocity (shaded) at 500 hPa are given by Figure 3.4c. The trough observed in at 1000 hPa and 850 hPa levels, also appears at 500 hPa, but slightly displaced to the northeast (Figure 3.4c), followed by strong upward motions ahead with peaks of -2.5 Pa/s. A large region of significant negative values of p–velocity associated to the trough is observed over the Atlantic Ocean (58 °W – 35 °W and 50 °S – 33 °S) and the La Plata Basin. Figure 3.4d depicts the wind direction (vector) and magnitude (shaded) at 250 hPa. The subtropical high level jet is observed over Argentina near to a diffluence zone that covers Uruguay, southern Brazil, the northeast of Argentina and Paraguay, which may contribute to upward motion. Conversely, the wind is significantly decelerating over this area, possibly leading to the opposite effect of the diffluence. This configuration may explain why wind divergence is not observed at 250 hPa in the region (not shown here). In addition, the trough observed at other levels also appears at 250 hPa slightly displaced to the northeast.

The dynamical patterns presented in Figura 3.4 provide a favorable environment for convection development over the La Plata Basin. The trough, which extends vertically along the troposphere slightly tilted to northeast, moves toward the La Plata Basin, contributing to low level convergence, and, therefore, upward motion. Furthermore, north wind at low levels advects heat and moisture, which provide an atmosphere favorable to MCS development.

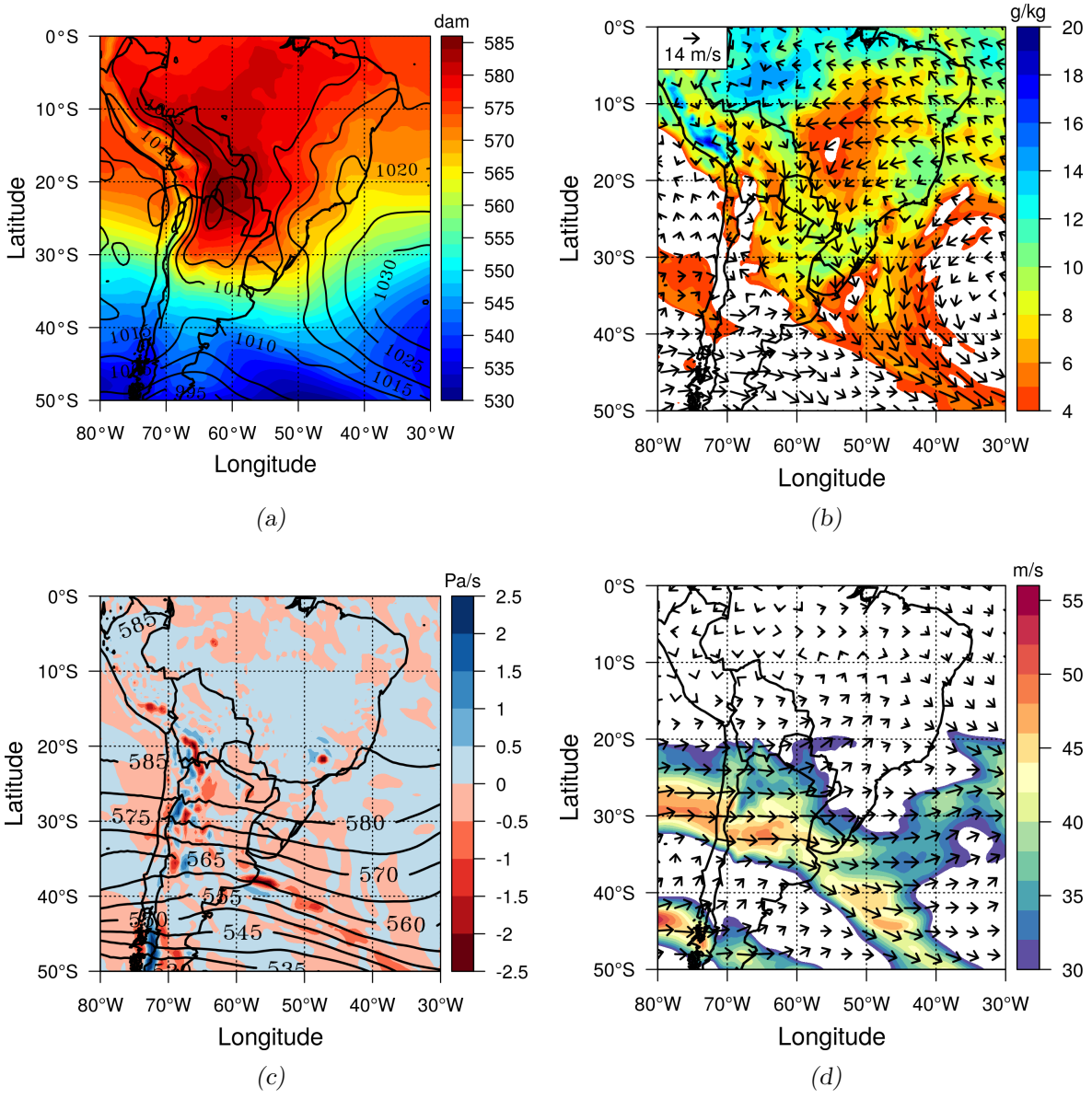


*Figure 3.4:* Synoptic fields on 21 September 2010 at 00:00 UTC: (a) sea level pressure (contour lines) and thickness (shaded); (b) wind (vectors) and specific humidity (shaded) at 850 hPa; (c) geopotential height (contour) and vertical p-velocity (shaded) at 500 hPa; and (d) wind direction (vector) and magnitude (shaded) at 250 hPa.

Synthetic satellite imagery is computed from model output in order to compare the simulations with GOES satellite observations. The synthetic brightness temperature is generated for the thermal channel 10.7 $\mu$m by using the Community Radiative Transfer Model (CRTM) that is described by Chen et al. (2008). Figure 3.5 shows these results at 06:00, 08:30 and 11:00 UTC for different CCN concentrations, where the brightness temperature is shaded. The MCS area was delimited by contouring the brightness temperature equal to -32 °C (Maddox, 1980), in order to use this area as a mask for statistical analyses. By comparing the Figure 3.5 against satellite observations (Figure 3.3), we can see that the convective cells are slightingly displaced toward the east, and the convection over the northeast of Argentina is not well simulated, and the lack of dense observational network in the region may partially explain the model's errors. However, the model presented results with reasonable accuracy and was able to simulate the main system's life cycle, which allows the study of aerosol impacts on the simulated MCS. Slight differences between the runs are noted, especially at 11:00 UTC. Experiments with more aerosols show smaller values of brightness temperature, which are located in different places for each simulation. These results suggest that CCNs can modify the microphysical structure of the system, although they do not seem capable of significantly changing its overall shape. Thus, a more detailed analysis is shown in the following paragraphs.

Figure 3.6 shows the precipitation results in terms of covered area, total accumulated and maximum rate as function of time. The covered area is computed by adding up the grid cell areas with precipitation for each 30 min; the total accumulated is basically the total of the precipitation occurred throughout time integration from 03:00 UTC; and the maximum rate is the maximum hourly accumulated precipitation in the finest grid domain for each 30 min. For these computations, we consider grid cells with at least 2 mm/h of precipitation. Precipitation shows different responses to CCN enhancements, depending on the point of view. The smallest amounts of total accumulated precipitation as well as the precipitation covered area are seen in the CN-Low run. As the CCN increases, larger amounts of total accumulated precipitation, covering bigger areas, are observed. On the other hand, the highest peak of the precipitation rate is seen at 09:00 UTC for CN-Med, followed by CN-Low, CN-High and CN-ExtHigh. The CN-Med experiment presents higher precipitation rates during most of the time.

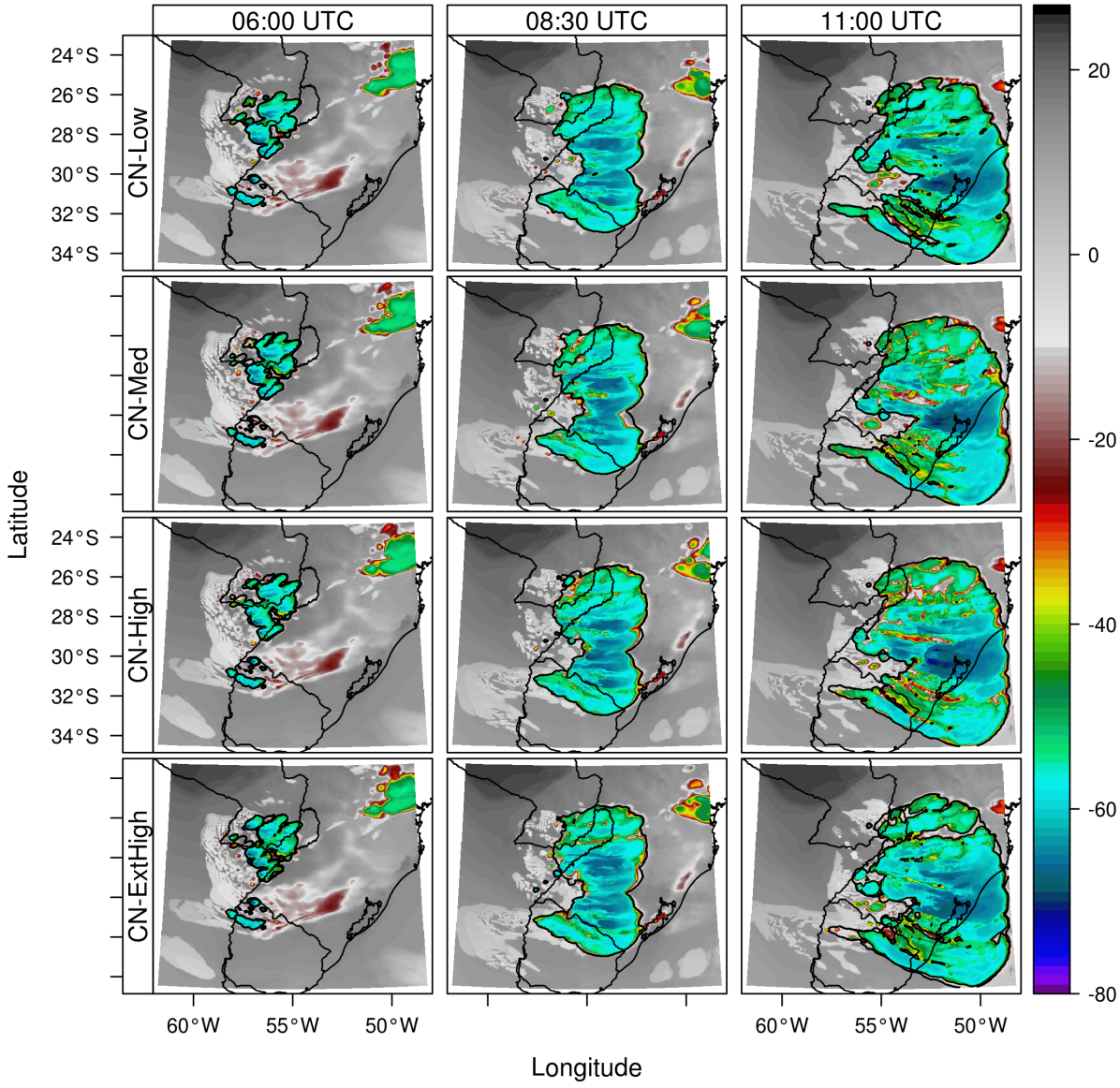


*Figure 3.5:* Synthetic infrared satellite images for the CN-Low, CN-Med, CN-High and CN-ExtHigh experiments at 06:00 (left panels), 08:30 (middle panels) and 11:00 UTC (right panels). Colors indicate brightness temperature at channel 10.7 $\mu$m. The black contour line refers to the brightness temperature equal to -32 °C, which delimits the MCS area (Maddox, 1980).

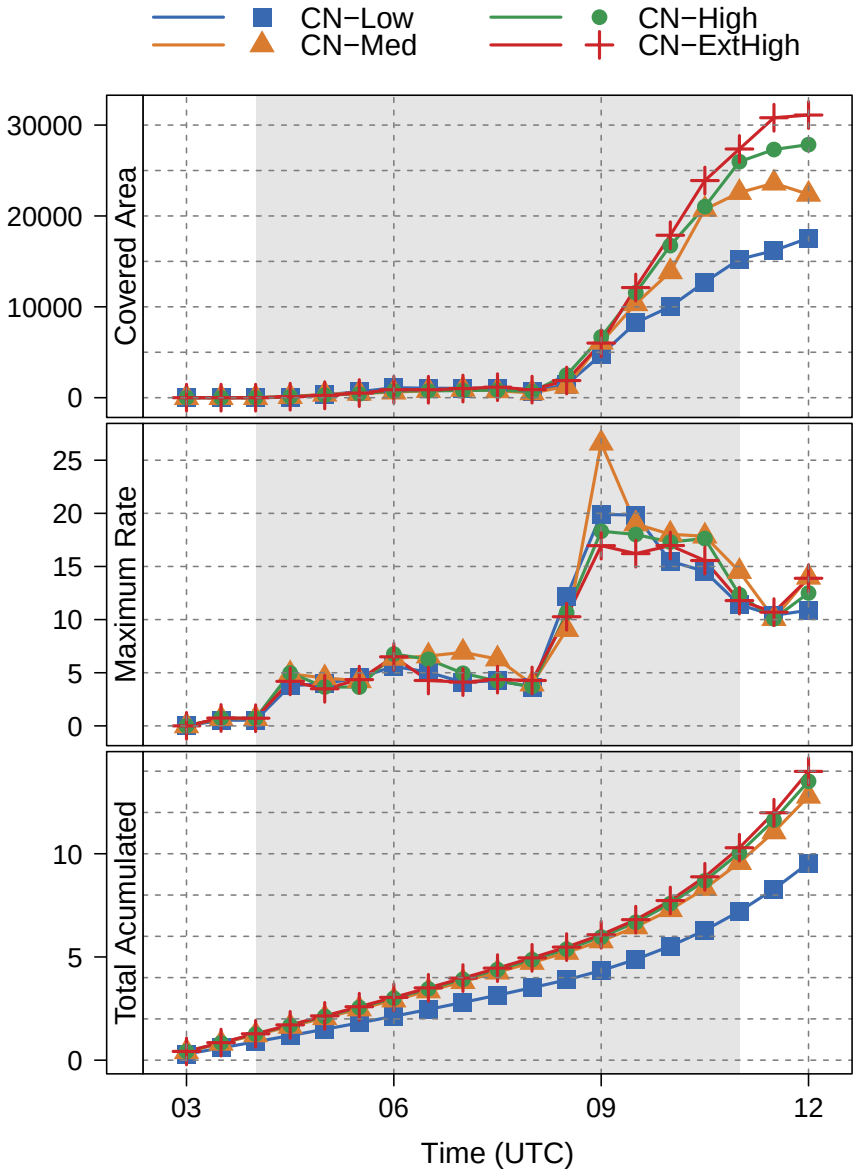


*Figure 3.6:* Precipitation covered area ($km^2$), maximum precipitation rate (mm/h) and total accumulated precipitation ($1 \times 10^5$ mm) as a function of time for the CN-Low (blue), CN-Med (marigold), CN-High (green) and CN-ExtHigh (red) experiments. The shaded area in grey represents the time period that the entire MCS is within the grid domain.

Figure 3.7 shows the total integrated upwelling vapor flux at cloud base, taking into account only the grid cells with vertical velocity greater than zero. This variable is computed by multiplying the vertical velocity on the cloud base by the vapor mixing ratio right below and then integrating horizontally in area. We consider grid cells with cloud mixing ratio bigger than $1 \times 10^{-6}$ g/kg and positive vertical velocity. Slight enhancement of CCN concentrations is enough to significantly change the input of vapor into the system. Further CCN enhancement leads to stronger upwelling vapor flux but does not increase the flux proportionally, revealing non-monotonical behavior.

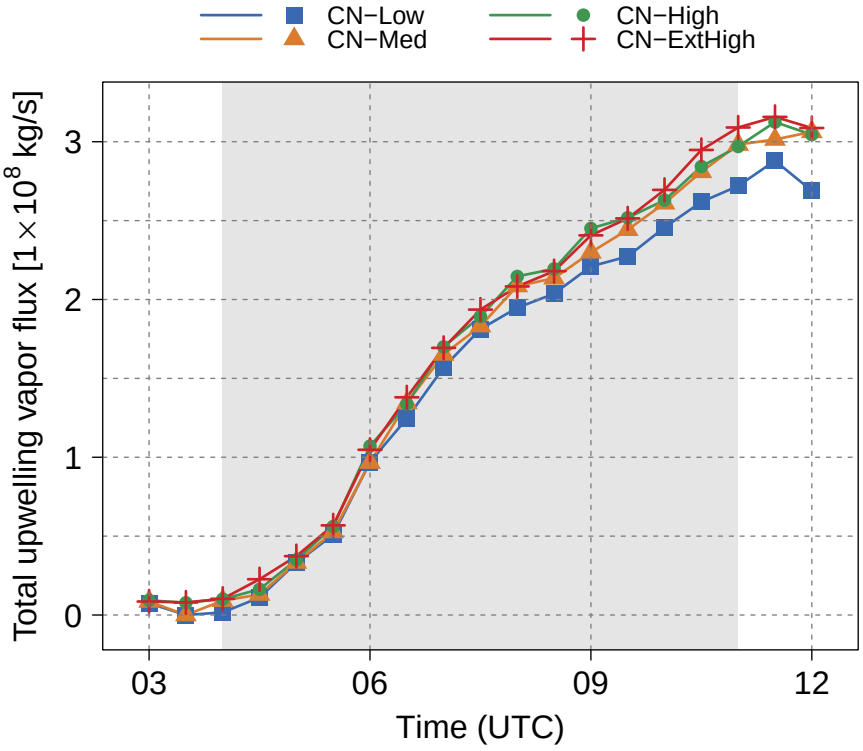


*Figure 3.7:* Total upwelling vapor flux at cloud base as function of time for the CN-Low (blue), CN-Med (marigold), CN-High (green) and CN-ExtHigh (red) experiments. The shaded area in grey represents the time period that the entire MCS is within the grid domain.

Updraft morphology is a key factor to understand the aerosol impact on cloud dynamics, as has been demonstrated in the literature (van den Heever et al., 2006; Carrió et al., 2010; Lebo and Morrison, 2014). Therefore, we computed the number and total area of updrafts for all runs as function of time (Figure 3.8). To compute the updraft number we select the grid columns with mean vertical velocity (between 2 and 8 km height) greater than 0.9 m/s, hence, updrafts with a reasonable vertical extension are kept; second, we group neighboring columns; third, we keep grid cells within these columns that have vertical velocities greater than 1 m/s in order to find the updraft boundaries. The total updraft area was calculated by adding up the maximum horizontal area in the vertical of each localized updraft. Experiments with higher aerosol concentrations tend to produce more updrafts, which, in turn, cover larger areas. These differences become apparent for certain periods such as 04:00 – 05:00 (system formation), 07:00 – 08:00, 08:00 – 09:30 and 09:30 – 11:00 (mature stage). The greatest differences between CN-Low and the other experiments occur during the mature stage, where CN-Med, CN-High and CN-ExtHigh exhibit about 250 updrafts, whereas CN-low has about 200 updrafts.

When we compare Figures 3.6, 3.7 and 3.8, similarities between these variables become evident and show an important link between cloud microphysics and dynamics. The number of updrafts and, consequently, their total covered area increase as aerosol concentration is enhanced. This effect results in higher values of total upwelling vapor flux at cloud base which feeds the condensation process. Hence, larger amounts of total accumulated precipitation are generated over a bigger area. It is important to note that the total accumulated covered area, the total upwelling vapor flux, the number of updraft cells and the total updraft area were computed using different approaches, which end up reinforcing the outcomes.

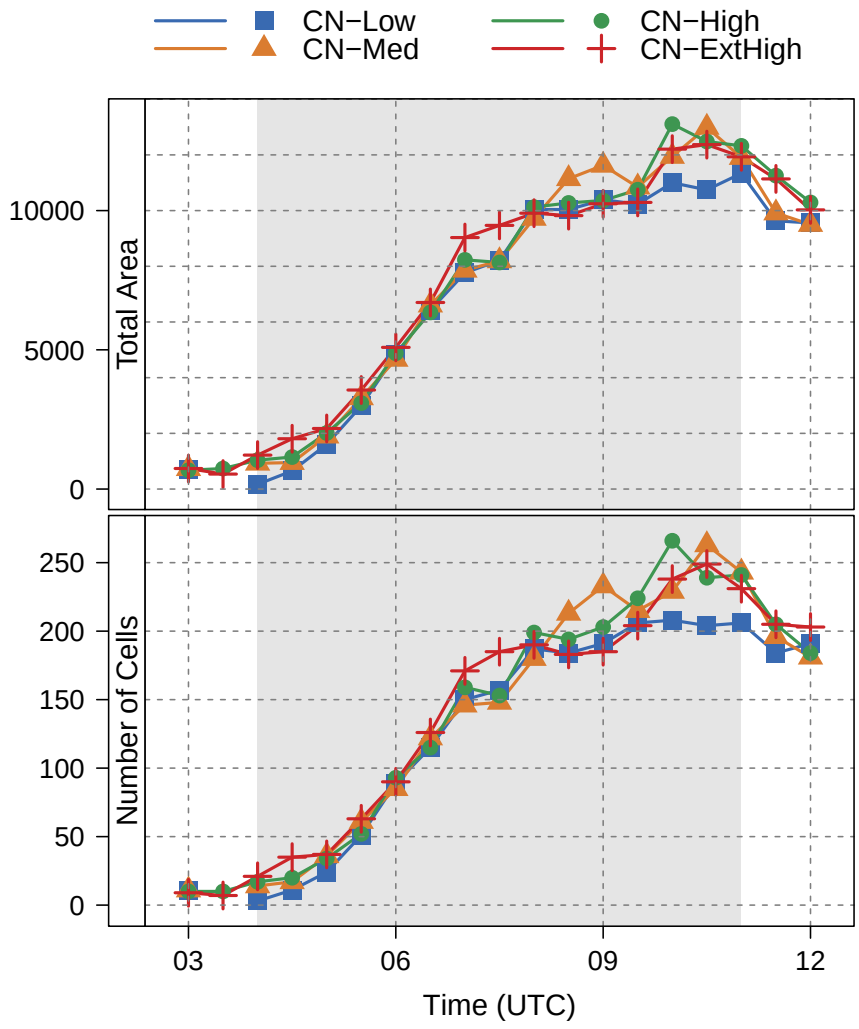


*Figure 3.8:* Total area of updraft ($km^2$) and number of updraft cells as a function of time for the CN-Low (blue), CN-Med (marigold), CN-High (green) and CN-ExtHigh (red) experiments. The volume integral of concentrations is weighted by their respective mass. The shaded area in grey represents the time period that the entire MCS is within the grid domain.

Volume integrals for liquid categories throughout time are computed for updraft greater than 5 m/s (Figure 3.9). In order to avoid meaningless computation, the volume integrals for concentrations of each liquid hidrometeor class are weighted by their mass. The maximum quantities of liquid mass, resulting from warm processes, are noted between 08:30 and 09:00 UTC. As CCN increases, cloud droplets and supercooled droplets increase in mass and number, whereas drizzle and rain demonstrate an opposite pattern. This effect is widely discussed in the scientific literature. In fact, higher aerosol loadings nucleate larger number of cloud droplets, inducing a narrow cloud droplet spectrum, in other words, lots of droplets with smaller sizes. As a consequence, the cloud droplet collection and warm rain formation are suppressed, allowing cloud droplets to be thrust aloft to upper levels. Once cloud droplets reach the freezing levels, they immediately become supercooled and are eventually either collected by ice particles or freeze.

Figure 3.10 shows the mean vertical profiles of mixing ratio and number of particles for cloud, drizzle, rain and supercooled droplets, considering the grid columns whose vertical velocity is greater than 5 m/s (Figure 3.10). The number concentration is weighted by the hydrometeor mass as in Figure 3.9. By comparing Figures 3.10 and 3.9, we can see that the aerosol effect observed in the volume integrals also clearly appears in the mean vertical profiles. In addition, we can see two well defined peaks in the supercooled profile at 5 and 8 km, respectively. It is also possible to note two sharp decreases in the droplet mixing ratio; the first one, placed between 5 and 7 km, is probably related to the riming process; and the second one, above 8 km, is associated to homogeneous freezing since cloud droplets freeze instantaneously at this height (regardless of the size) where the temperature is below -35 °C.

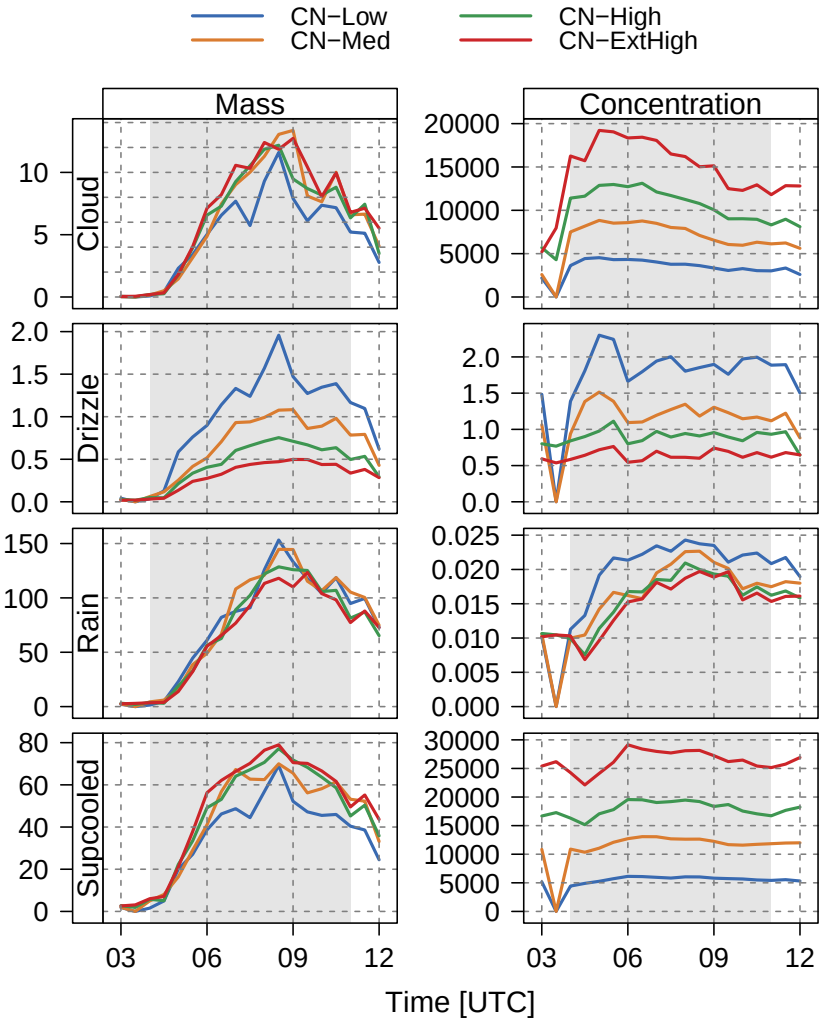


*Figure 3.9:* Volume integrals of cloud, drizzle, rain and supercooled cloud in terms of mass ($1 \times 10^8$ kg) and number concentration ($1 \times 10^5$ $m^{-3}$) throughout time for the CN-Low (blue), CN-Med (marigold), CN-High (green) and CN-ExtHigh (red) experiments. Only grid columns with updraft greater than 5 m/s are considered in the computation. The number concentrations are weighted by their respective mass. The shaded area in grey represents the time period that the entire MCS is within the grid domain.

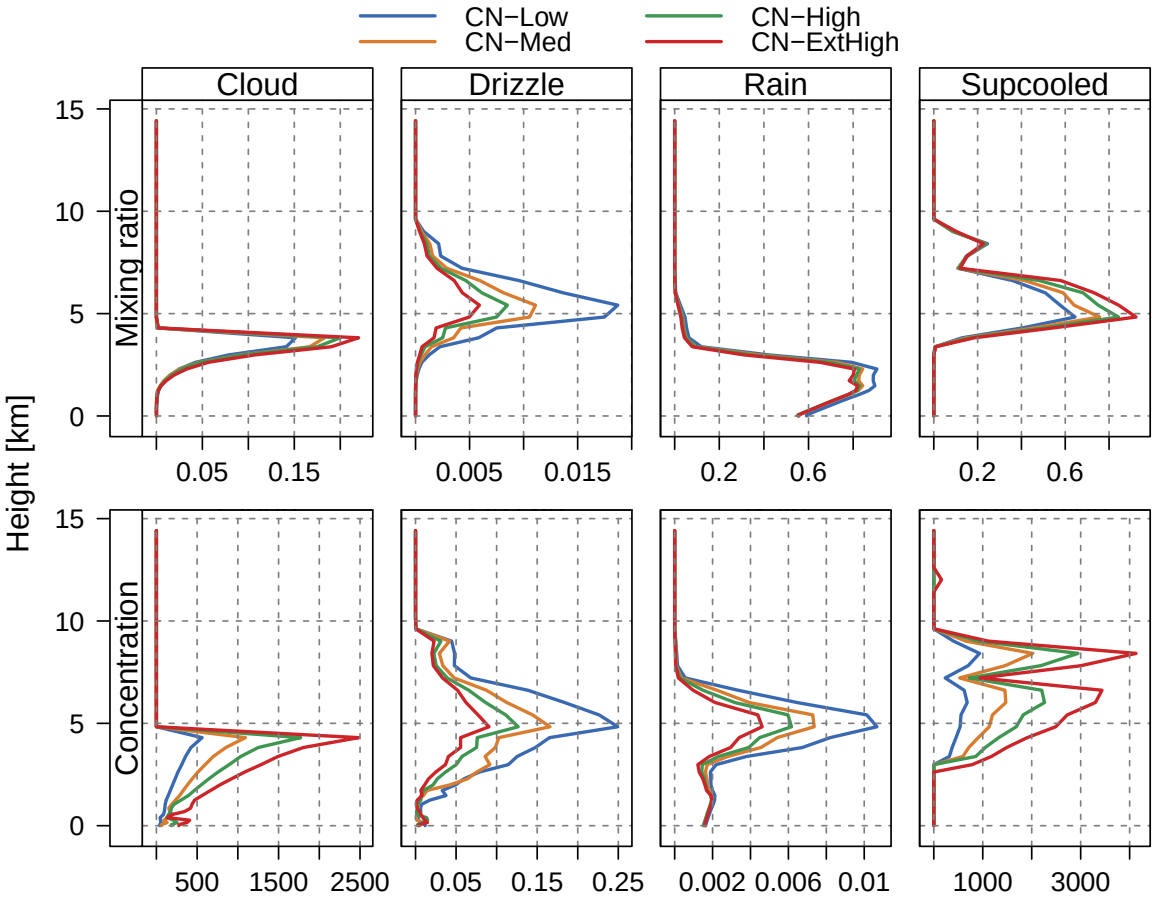


*Figure 3.10:* Mean vertical profiles of mixing ratio (g/kg) and number concentration ($1 \times 10^6$ m$^{-3}$) for cloud, drizzle, rain and supercooled cloud for the CN-Low (blue), CN-Med (marigold), CN-High (green) and CN-ExtHigh (red) experiments. Only grid columns with updraft greater than 5 m/s are considered in the computation.

Similar to Figure 3.9, Figure 3.11 depicts the volume integral of mass and number concentration for pristine and aggregates as a function of time. The total pristine mass does not show a clear response to aerosol increase, although huge amounts of aerosol seem to contribute to a decrease in the pristine mass. On the other hand, pristine number concentration has a monotonic response to CCN enhancement. The total aggregate mass and number concentration present a nonlinear response to aerosol increase, as already mentioned. Therefore, a slight increase in CCN (CN-Med compared to CN-Low) favors aggregate formation. However, further enhancements have the same impact on CN-Med, in other words, total aggregate mass and concentration do not change at the same rate as CCN particles increase. The average profiles for pristine and aggregates, given by Figure 3.12 (constructed as Figure 3.10), also captured the aerosol effect revealed in the volume integral. Moreover, above 8 km height, pristine mass and number concentration increase, while supercooled droplets decrease, indicating that ice particles are being formed by homogeneous freezing of cloud droplets.

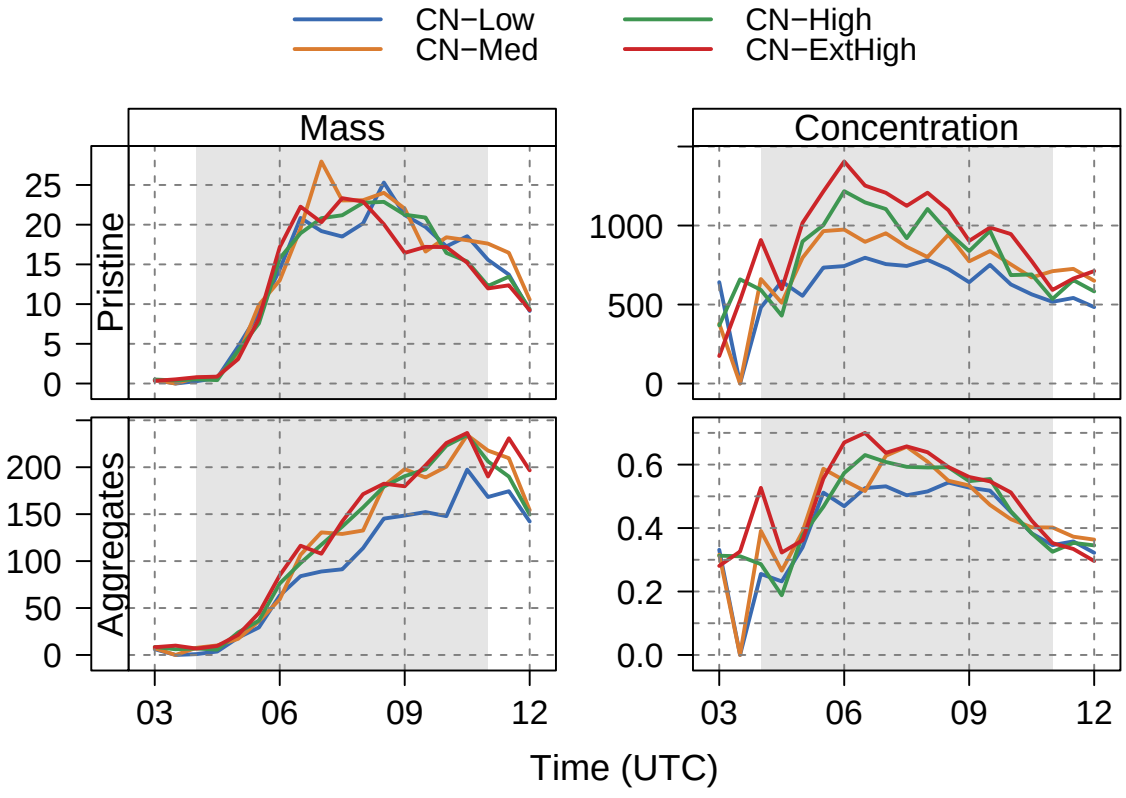


*Figure 3.11:* As in Figure 3.9, but for pristine and aggregate categories.

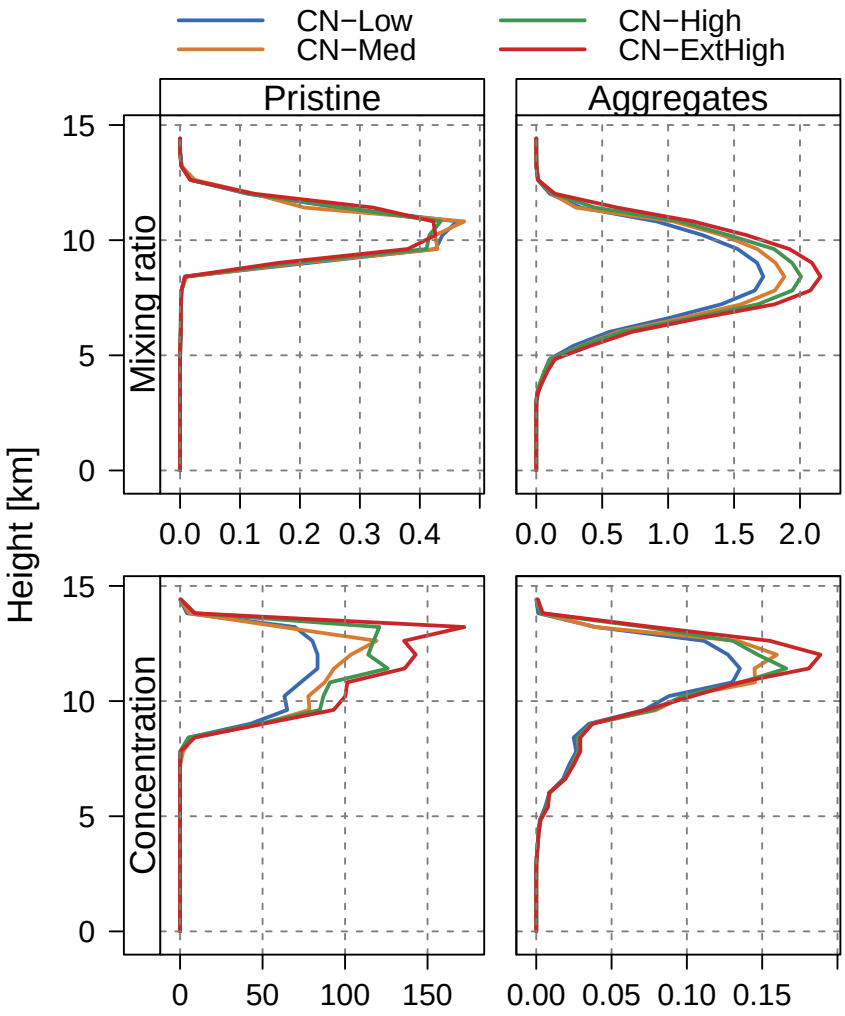


*Figure 3.12:* As in Figure 3.10, but for pristine and aggregate categories.

Immersed within an environment rich in supercooled liquid water, aggregate particles are likely to grow by the rimming process, rapidly allowing these ice particles to become graupel by collecting cloud droplets. Figure 3.13 (computed as Figure 3.9) illustrates this effect clearly, with a monotonically increase in the graupel mixing ratio as CCN is enhanced. In contrast, hail decreases monotonically as aerosol increases because of the cloud diameter reduction in response to high CCN concentration, as explained earlier. Indeed, tiny cloud droplets are more likely to be deflected by the air flow around the hailstones since they do not have enough inertia. Figure 3.12, computed as Figure 3.10, also shows this effect, being even clearer for the hail mixing ratio.

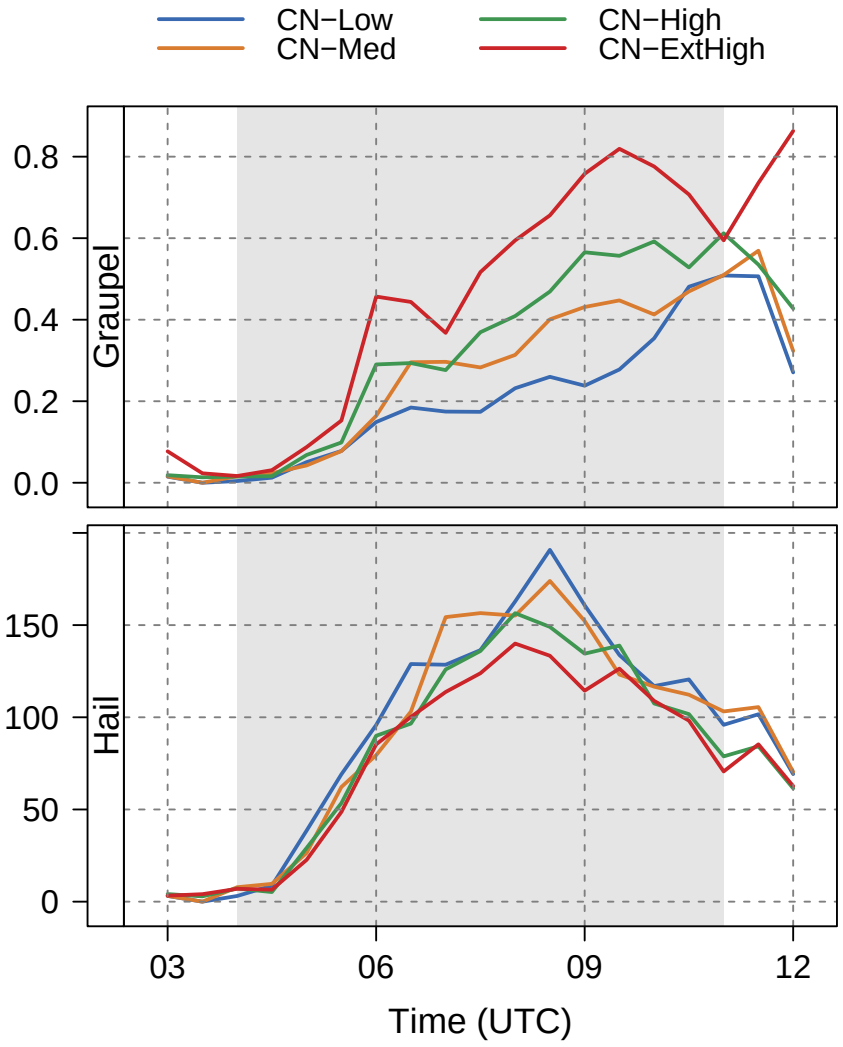


*Figure 3.13:* As in Figure 3.9, but for graupel and hail mixing ratios.

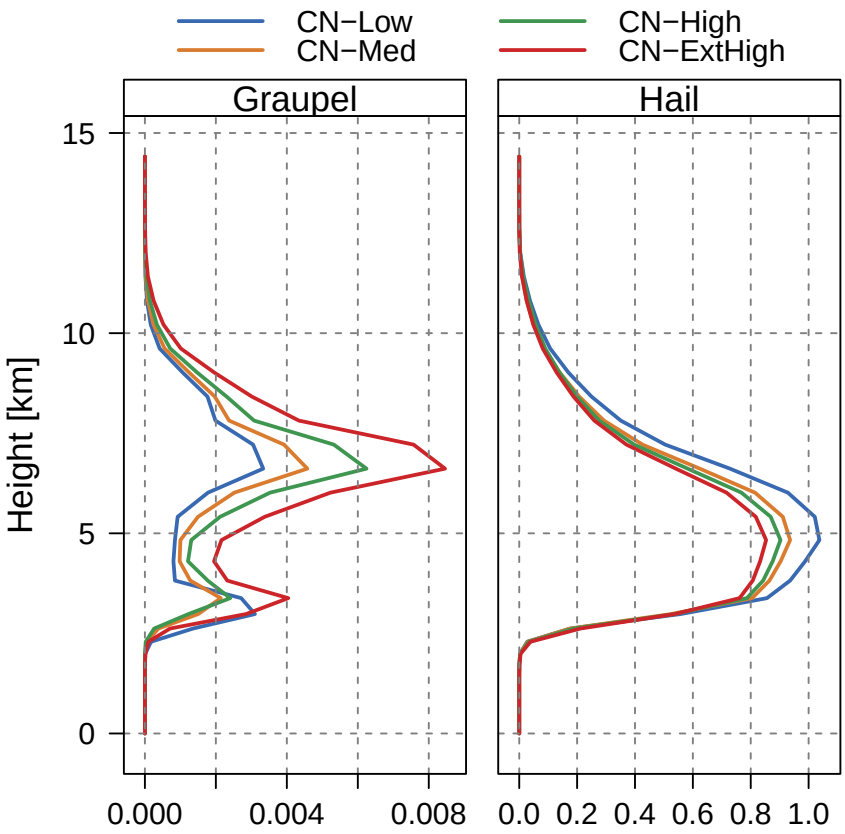


*Figure 3.14:* As in Figure 3.10, but for graupel and hail mixing ratios.

Figure 3.15 compares the vertical velocities produced by the experiments, where the left-hand panel shows an average of the three highest updraft peaks, whereas the right-hand panel shows the vertical velocity profile of the column with the strongest updraft. The updraft response to CCN number variation is highly nonlinear and depends on several factors. However, the updraft seems more intense for higher aerosol concentrations after 09:00 UTC (Fig. 3.15a), which might be associated with latent heat release. The maximum vertical velocity is produced by the CN-ExtHigh experiment, followed by the CN-Med, CN-Low and CN-High experiments(Fig. 3.15b). High aerosol loading may displace the updraft peak aloft as a consequence of homogeneous freezing enhancement (Carrió et al., 2014). This effect is due to riming suppression since cloud droplets are too small, being deflected by the air flow around the ice particles. Furthermore, riming suppression also causes a decrease in the updraft intensity below 10 km (Figure 3.15b) owing to the lower latent heat realized.

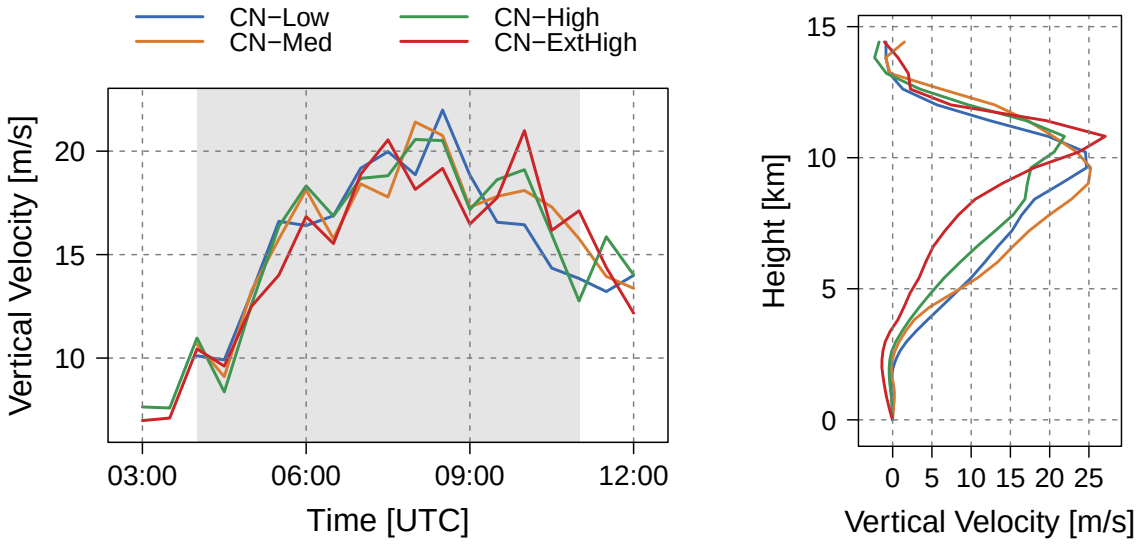


*Figure 3.15:* Average of the three highest updraft peaks throughout time (a) and strongest updraft profile (b) for the CN-Low (blue), CN-Med (marigold), CN-High (green) and CN-ExtHigh (red) experiments. The shaded area in grey represents the time period that the entire MCS is within the grid domain.

Columns from the ground up to height of 2 km with downdraft greater than 1 m/s were averaged for buoyancy, rain mixing ratio and downdraft speed (Figure 3.16) for the time period between 9:00 and 10:00 UTC. The model outputs were saved every 5 min to compute these profiles. The CN-ExtHigh experiment stands out with the largest values of rain mixing ratio, leading to stronger negative buoyancy and downdraft than the CN-Low experiment. In addition, the other two experiments, CN-Med and CN-High, present similar behavior when compared to CN-Low, although less pronounced. The highest rain mixing ratio of the CN-ExtHigh experiment may suggest the contribution of ice melting. Indeed, higher amounts of rain favor stronger negative buoyancy since the drops evaporate in an unsaturated environment, lowering the air temperature. This effect leads to heavier air parcels, which increase the vertical velocity toward the ground. Finally, stronger downdrafts intensify the low level convergence, which, in turn, may contribute to the formation and intensification of updrafts (Tao et al., 2007, 2012; Lebo and Morrison, 2014).

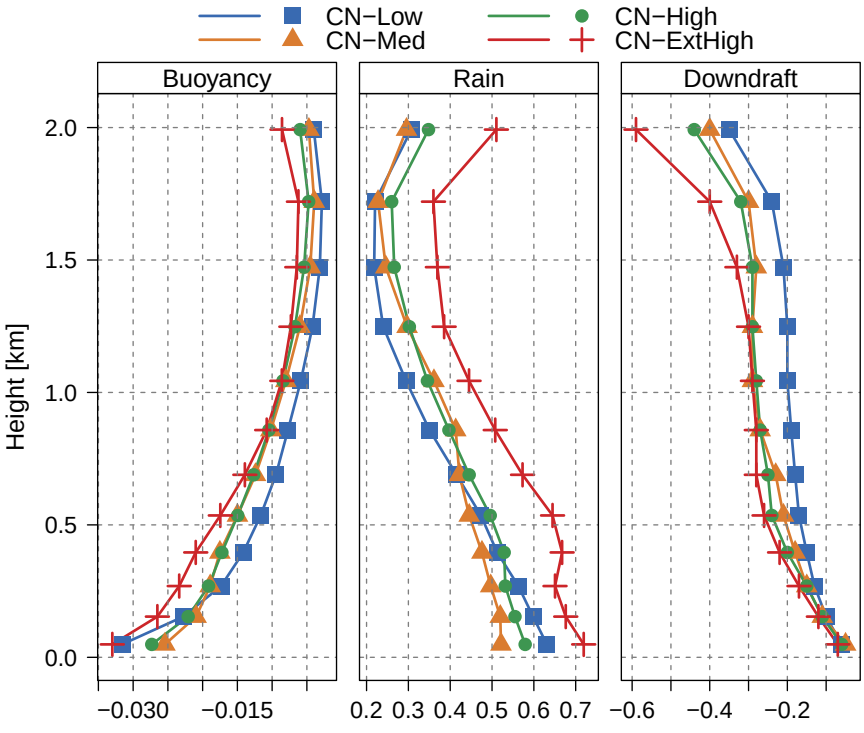


*Figure 3.16:* Averaged buoyancy, rain mixing ratio and downdraft between 9:00 and 10:00 UTC for the CN-Low (blue), CN-Med (marigold), CN-High (green) and CN-ExtHigh (red) experiments. The model outputs were saved every 5 min to compute these profiles. Only vertical velocities smaller than -1 m/s are considered for the average.

## 3.4 Conclusions

Many studies have shown the importance of studying the effect of biomass burning aerosols on cloud systems over the Amazon and neighboring regions (Andreae et al., 2004; Freitas et al., 2005; Koren et al., 2004, 2008; Martins et al., 2009; Martin et al., 2010; Artaxo et al., 2013; Gonçalves et al., 2015). Some authors suggest that these aerosols can be transported by low level flow to the La Plata Basin (Freitas et al., 2005). In this context, we performed four experiments with BRAMS-4.3, varying CCN concentration for an MCS case occurring over the La Plata Basin on 21 September 2010. The model was initialized with idealized CCN profiles that were based on Freitas et al. (2005).

Generally, higher CCN loadings increase the concentration of cloud droplets, and, consequently, reduce the collision-coalescence efficiency. This effect allows more droplets to reach the freezing levels and become supercooled. The availability of supercooled cloud droplets is directly linked to the riming efficiency. The chances of these hydrometors being collected by ice particles increase since there are more supercooled droplets available. Therefore, larger aggregates and graupel mixing ratios were observed as aerosol number concentration increases. Conversely, the hail mixing ratio decreased under larger aerosol loadings, which could be explained by the droplet size. Small cloud droplets are more likely to be deflected by the flow around hail particles, thereby reducing the riming efficiency. Then tiny supercooled droplets reach levels with temperatures below -35 °C, being instantaneously frozen.

The reduction of riming efficiency leads to a decrease in the updraft velocity below the homogeneous freezing level (below 10 km height) because less latent heat is released. However, since these small droplets were not collected by hail, they are capable of freezing homogeneously at upper levels. This effect increases the vertical velocity which, in turn, displaces the updraft peak to higher levels.

An invigoration of the downdrafts was verified for high CCN concentrations at low levels (below 2 km). The experiments with more CCN particles showed larger values of rain mixing ratio at low levels. Since there is more mass to evaporate, higher values of negative buoyancy were noted. This phenomenon leads to an invigoration of the downdrafts. Stronger downdrafts helped to increase the number of updraft cells, and, consequently, the total area covered by them. With more updraft cells, higher amounts of total upwelling

vapor flux were observed, favoring the condensation process. Associated with this effect, larger amounts of total accumulated precipitation over a bigger area were generated under higher concentration of CCN.

This paper is the first to study the impact of Amazon biomass burning aerosols on mesoescale convective system over the La Plata Basin from a numerical modeling point of view taking into account cloud microphysics – dynamics interactions. We showed an important link between aerosol microphysical effects, cloud dynamics and precipitation for the specific case of aerosols feeding an MCS in the La Plata Basin. Camponogara et al. (2014) observed a decrease in precipitation in the La Plata Basin associated with an increase in AOD (Aerosol Optical Depth) measured in the Amazon Basin as one of the possible scenarios detected in the data available for the period from 1999 up to 2012. They also detected a pattern where no aerosol effect on rainfall could be detected. Indeed, cloud-aerosol interactions are highly nonlinear, and different responses may occur, depending on environmental conditions as discussed in Section 3.1. Therefore, this issue needs further investigation, particularly with an extended number of cases, in order to fully understand the role of Amazon aerosols on mesoscale convective systems that take place over the La Plata Basin.

Chapter 4

# Mesoscale data assimilation

This chapter will be submitted for publication in the Geoscientific Model Development Journal.

## *4.1 Introduction*

In the past few decades the observation network has widely expanded and received significant improvement. Along with that, sophisticated assimilation techniques have been developed in order to incorporate observations into numerical models. As a consequence, the numerical weather prediction has become more accurate, although there still are many issues that need to be improved as, for example, the assimilation of non-state variables (i.e., radar reflectivity, satellite radiances, etc.). These type of observations cover larger areas than state variable (e.g., wind, temperature, pressure) and contribute to a better representation of the atmosphere state, especially for regions poor in state variable observations as, for instance, the La Plata Basin. In this context, ensemble data assimilation methods arise as a good solution to deal with this problem.

As mentioned by Kalnay (2003), ensemble data assimilation (EnsDA) is a method that computes different initial conditions of state variables in order to create ensemble model forecasts and observation operators. EnsDA is capable of producing an optimal estimation of state variables and their uncertainties owing to use of a flow-dependent background error covariance. The matrix is computed from ensemble model forecasts and is updated every assimilation cycle. One of most popular EnsDA algorithm is the ensemble Kalman filter (EnKF; Evensen, 1994) that has been widely used by the science community (Whitaker et al., 2008; Li et al., 2012; Weng and Zhang, 2012; Lavaysse et al., 2013; McMillan et al.,

2013; Bei et al., 2014; Houtekamer et al., 2014; Rubin and Collins, 2014; Buehner et al., 2015; Schwartz et al., 2015; Erdal and Cirpka, 2016; Zhang et al., 2016). The reason for this acceptance is related to the fact that EnKF can deal with nonlinear processes and is relatively easy to implement (Evensen, 1994, 2003).

A promising variation of the EnKF assimilation technique, called Maximum Likelihood Ensemble Filter (MLEF), has been developed by a group of researchers from CIRA (Cooperative Institute for Research in the Atmosphere) and is described by Zupanski (2005) and Zupanski et al. (2008). MLEF is designed to deal with highly nonlinear problems and represents the state-of-art in data assimilation. This algorithm combines the ensemble forecast method with an iterative cost function minimization technique.

During the last decade MLEF has been successfully implemented in numerical models such as Korteweg–de Vries–Burgers (Zupanski, 2005), finite-difference shallow-water global model (Zupanski et al., 2006), Goddard Earth Observing System Single Column Model (GEOS-5 SCM; Zupanski et al., 2007), Regional Atmospheric Modeling System (RAMS; Carrió et al., 2008) and Weather Research and Forecasting (WRF) model (Zupanski and Zupanski, 2009; Zupanski et al., 2011). Also, this assimilation algorithm has been applied for different meteorological phenomena with different types of data sets.

Carrió et al. (2008) explored the possibility of applying MLEF on microscale by using RAMS in cloud resolving model and large-eddy simulation modes. The authors assimilated remote sensing observations measured during FIRE/SHEBA field experiments. The data assimilation algorithm improved the model's simulation for the mixed-phase of boundary layer clouds in the Arctic, being capable of representing a polluted air mass above the inversion layer in terms of IFN and CCN. Furthermore, they observed a gain in quality of simulations as the ensemble size increases.

By assimilating synthetic GOES-R radiances at 10.35 $\mu$m throughout a coupled framework WRF–MLEF, Zupanski et al. (2011) evaluated the MLEF capability of extracting information from GOES-R radiances and incorporating into the atmospheric model for an extratropical cyclone case. The authors observed significant improvement of simulations with data assimilation when compared to the simulation without assimilation. They also observed different results depending on the control variable choice. For instance, cloud ice mixing ratio showed to be more relevant than potential temperature to improve the model performance since cloud ice mixing ratio can significantly affect the cloud top temperature.

Furthermore, they observed better results when hydrometeors that are more sensitive to satellite radiances are included. Later, Zupanski and Zupanski (2009) extended this study incorporating synthetic satellite microwave observation plus synthetic infrared brightness temperatures into WRF–MLEF system. As seen by Zupanski et al. (2011), the inclusion of microphysical control variables with satellite radiances as observations is beneficial to the numerical simulation of the extratropical cyclone case. The authors also noted that a larger number of control variables seem to contribute to the forecast improvement since these allow more freedom to MLEF adjustments in the numerical simulation.

As a creative example of the MLEF application, Apodaca et al. (2014) used the MLEF/WRF framework in order to assimilate lightning measurements (lightning strikes) as storm source information. The observation operator was computed by an empirical estimation of the flash lightning rate from the model's maximum updraft velocity. Unfortunately, a clear improvement was not observed for the 6 hour forecast. Nevertheless, the assimilation system affected several model state variables and improved the simulation in many assimilation cycles.

The nocturnal MCS formation is a result of a combination of synoptic scale forcing (e.g., weak mid-level short wave) plus mesoscale forcing (e.g., low-level jet) (Fritsch and Forbes, 2001). It is a big challenge to numerically simulate MCSs over the La Plata Basin since there are not enough observations of model state variables to represent appropriately the mesoscale environment. On the other hand, there are plenty measurements of non-state variables, such as satellite radiances, that cover entirely the La Plata Basin with a reasonable spacial and temporal resolution. In this context, this study aims to develop a coupled system between BRAMS–MLEF capable of assimilating infrared satellite radiances and to improve the simulation of a nocturnal MCS case observed over the La Plata Basin. Although the MLEF had been coupled to RAMS previously (Carrió et al., 2008), the BRAMS-MLEF coupling for mesoscale applications was a new development that represented a challenge with respect to computational issues as well as theoretical and practical aspects of the assimilation procedure. This is a first attempt to improve a simulation of a nocturnal MCS by assimilating not only the classical state variables but also satellite radiances. A detailed explanation about this coupled system is presented in Section 4.2. Sections 4.3 and 4.4 show the numerical results and conclusions, respectively.

## 4.2 Methodology

### 4.2.1 MESOASSIM

The Mesoscale Assimilation system (MESOASSIM) is a coupled framework of the atmospheric model BRAMS–4.3 and the assimilation algorithm MLEF. This framework is based on BRAMS/MLEF and RAMS/MLEF coupled versions for microscale data assimilation described by Carrió et al. (2008). MESOASSIM has been developed for mesoscale data assimilation and can incorporate infrared satellite data into BRAMS-4.3. Moreover, this system works in parallel in both supercomputers TUPÃ (from CPTEC/INPE – *Centro de Previsão de Tempo e Estudos Climáticos / Instituto Nacional de Pesquisas Espaciais*) and SDUMONT (from LNCC – *Laboratório Nacional de Computação Científica*). Hereafter a detailed description of MESOASSIM is presented: Section 4.2.1.1 reveals the MLEF algorithm; Section 4.2.1.2 describes the observation operator; Section 4.2.1.3 shows the MESOASSIM code suite; and Section 4.2.1.4 describes implementation issues related to MESOASSIM. The model BRAMS–4.3 has already been described in Chapter 3.

#### 4.2.1.1 Maximum likelihood ensemble filter

For the purpose of improving BRAMS's simulations, the Maximum Likelihood Ensemble Filter (MLEF) has been coupled into the atmospheric model. According to Zupanski (2005), MLEF combines ensemble data assimilation and maximum likelihood techniques in a new mathematically consistent framework. As an EnsDA algorithm, this framework computes a flow-dependent background error covariance to deal with model's uncertainties, which makes MLEF suitable for highly nonlinear processes. In summary, the goal of MLEF is to seek the maximum likelihood solution by minimizing the following cost function:

$$J(\boldsymbol{x}) = \frac{1}{2}(\boldsymbol{x} - \boldsymbol{x}_b)^T \boldsymbol{P}_f^{-1}(\boldsymbol{x} - \boldsymbol{x}_b) + \frac{1}{2}[\boldsymbol{y} - H(\boldsymbol{x})]^T \boldsymbol{R}^{-1}[\boldsymbol{y} - H(\boldsymbol{x})] \tag{4.1}$$

where $\boldsymbol{x}$ is the state vector whose length is defined by $N_{state}$ and $\boldsymbol{x}_b$ is the background state vector (prior state), also of dimension $N_{state}$. The nonlinear observation operator ($H$), placed in the second term of Eq. 4.1, converts the model space to observational space and is followed by the observation vector ($\boldsymbol{y}$) of dimension $N_{obs}$ (number of observations). $\boldsymbol{P}_f$ defines the forecast error covariance matrix ($N_{state} \times N_{state}$) and $\boldsymbol{R}$ indicates the observation

error covariance matrix ($N_{obs} \times N_{obs}$). The superscript T, placed in both terms of Eq. 4.1, represents the transpose of matrices.

The matrix $\boldsymbol{P}_f$ is computed by $\boldsymbol{P}_f = \boldsymbol{P}_f^{1/2}(\boldsymbol{P}_f^{1/2})^T$ and its square-root is defined as

$$\boldsymbol{P}_f^{1/2} = (\boldsymbol{b}_1 \;\; \boldsymbol{b}_2 \;\; \cdot \;\; \cdot \;\; \boldsymbol{b}_{N_{ens}}),\; \boldsymbol{b}_i = M(\boldsymbol{x}_{t-1} + \boldsymbol{p}_i) - M(\boldsymbol{x}_{t-1}) \tag{4.2}$$

where $M$ represents the forecast model and $\boldsymbol{p}_i$ is the random perturbation vector for each ensemble member $i$. The vector $\boldsymbol{b}_i$ is the column of matrix $\boldsymbol{P}_f^{1/2}$.

The Hessian preconditioning is incorporated into the MLEF algorithm by the change of variable

$$\boldsymbol{x} - \boldsymbol{x}_b = \boldsymbol{G}^{1/2}\boldsymbol{\zeta},\; \boldsymbol{G}^{1/2} = \boldsymbol{P}_f^{1/2}[\boldsymbol{I} + \boldsymbol{C}(\boldsymbol{x}_b)]^{-1/2} \tag{4.3}$$

where $\zeta$ is defined as the control vector of dimension $N_{ens}$ (number of ensemble members), $\boldsymbol{I}$ is the identity matrix ($N_{ens} \times N_{ens}$) and $C$ is a $N_{ens} \times N_{ens}$ matrix computed by

$$\boldsymbol{C}(\boldsymbol{x}_b) = [(\boldsymbol{Z}(\boldsymbol{x}_b))^T \boldsymbol{Z}(\boldsymbol{x}_b)]^{-1/2} \tag{4.4}$$

This algorithm updates $\zeta$ iteratively according to $\zeta_k = \zeta_{k-1} + \alpha_{k-1}\boldsymbol{d}_{k-1}$, where index k represents the minimization iteration, $\alpha$ is the step-length and $\boldsymbol{d}$ is the descent direction. The matrix $\boldsymbol{Z}$ is the observation perturbation formed by column vectors $z_i$ that is computed by

$$\boldsymbol{z}_i = \boldsymbol{R}^{-1/2}H(\boldsymbol{x} + \boldsymbol{b}_i) - \boldsymbol{R}^{-1/2}H(\boldsymbol{x}) \tag{4.5}$$

The eigenvalue decomposition is applied to the matrix $\boldsymbol{C}$ by the equation $\boldsymbol{C} = \boldsymbol{V}\boldsymbol{\Lambda}\boldsymbol{V}^T$, where $\boldsymbol{V}$ is the eigenvector and $\boldsymbol{\Lambda}$ is the eigenvalue. Hence, it is possible to efficiently compute the inverse square-root of $[\boldsymbol{I} + \boldsymbol{C}]^{-1/2}$ as follows:

$$[\boldsymbol{I} + \boldsymbol{C}]^{-1/2} = \boldsymbol{V}(\boldsymbol{I} + \boldsymbol{\Lambda})^{-1/2}\boldsymbol{V}^T \tag{4.6}$$

Once the Hessian preconditioning is calculated, the cost function gradient (Eq. 4.1) can be easily achieved by using the expression

$$\nabla J(\boldsymbol{x}) = [\boldsymbol{I} + \boldsymbol{C}(\boldsymbol{x}_b)]^{-1}\boldsymbol{\zeta} - (\boldsymbol{Z}(\boldsymbol{x}))^T\boldsymbol{R}^{-1/2}[\boldsymbol{y} - H(\boldsymbol{x})] \tag{4.7}$$

To compute the square-root analysis error covariance $\boldsymbol{P}_a^{1/2}$, MLEF uses the inverse of the Hessian matrix, updated after the cost function minimization, as follows:

$$\boldsymbol{P}_a^{1/2} = \boldsymbol{P}_f^{1/2}[\boldsymbol{I} + \boldsymbol{C}(\boldsymbol{x})]^{-1/2} \tag{4.8}$$

The cost function minimization is computed iteratively by using either the generalized nonlinear conjugate-gradient or the generalized quasi-Newton methods (Zupanski et al., 2008). Due to the Hessian preconditioning implementation, MLEF typically achieves convergence after 2–3 iterations (Zupanski, 2005).

#### *4.2.1.2 Observation operator*

As the main goal of this work is to assimilate GOES satellite radiances, we coupled the community radiative transfer model (CRTM) into MLEF. CRTM has been developed by the US Joint Center for Satellite Data Assimilation (JCSDA) and is mainly addressed to be incorporated into data assimilation systems (Chen et al., 2008). According to Chen et al. (2008) CRTM has specific modules that computes surface emissivity and reflectivity, aerosol absorption and scattering, cloud absorption and scattering, and gaseous absorption. This radiative transfer model is capable of computing radiances at the top of the atmosphere in order to simulate satellite data from microwave to infrared spectral regions by using model state variables as input.

We choose to compute the infrared brightness temperature (BT) at channel 10.7 $\mu m$ since it is not significant attenuated by the atmosphere. In addition, the emissivity is approximately 1 at this wavelength for almost all types of cloud and surfaces. In other words, the temperature related to this channel is close to the real temperature of cloud tops and surfaces. The mixing ratios and diameters for five hydrometers classes (cloud, rain, pristine, aggregates and graupel), atmospheric and canopy temperatures, pressure and the longitude/latitude location of each grid cell are used as input for calculation of BT by the CRTM. After BT is obtained, the normalized innovation vector $\boldsymbol{R}^{-1/2}[\boldsymbol{y} - H(\boldsymbol{x})]$ is finally computed.

Due to computational limitation, it was decided to interpolate the observations space into the model space instead of doing the opposite way that would be the ideal procedure. The inverse distance weighting (IDW) method was used to interpolate the observation grid into the model grid. This procedure will be changed in future updates.

#### 4.2.1.3 Computational suite

Figure 4.1 shows a flow chart of MESOASSIM that presents the main computational steps executed by the algorithm. Below follows a brief description about each one of these steps:

1. BRAMS is initialized with the data described in Section 4.2.2 to generate an output with the chosen control variables (control), that is, variables that will be both perturbed to create the ensemble members and updated by MLEF after every assimilation cycle;

2. Control variables are perturbed in order to generate the ensemble members ($\boldsymbol{b}_1$, $\boldsymbol{b}_2$, ..., $\boldsymbol{b}_{Nens}$);

3. MESOASSIM starts the cold run, i.e., BRAMS is initialized with non-perturbed variables (control) and, later with perturbed ones of each ensemble member separately. BRAMS is run without data assimilation at this point because the model needs time for adjusting to the initial conditions (spin-up time);

4. After the spin-up time, the assimilation cycle begins and BRAMS starts the forecast run for the assimilation cycle interval;

5. The forecast error covariance matrix computation takes place. As the analysis is unknown, MESOASSIM computes $\boldsymbol{P}_f^{1/2}$ from the model outputs as a first guess and later, calculates $\boldsymbol{P}_f$;

6. The observation operator computes the brightness temperature for control and ensemble members from the first guess;

7. In the first iteration of the cost function minimization, the Hessian preconditioning is calculated as shown in Section 4.2.1.1. This part is skipped by the code for next iterations;

8. The cost function is minimized and both analysis and analysis error covariance matrix are computed. In case of more iterations, the observation operator is recomputed by using the analysis instead of the first guess;

9. The next assimilation cycle begins.

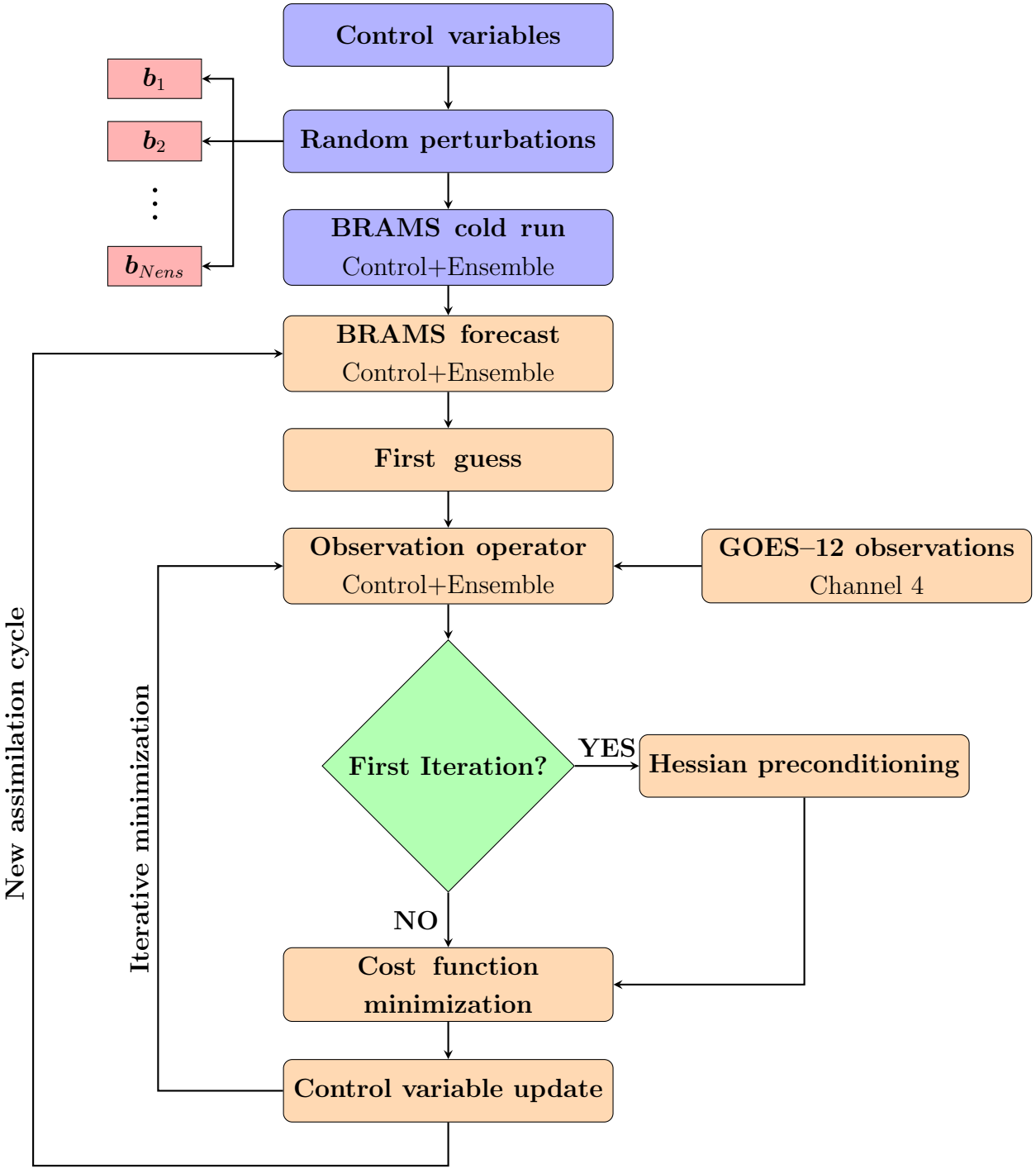


*Figure 4.1:* Flow diagram of MESOASSIM.

#### 4.2.1.4 Implementation issues

Hundreds of simulations were performed in order to find the best MESOASSIM setting and to resolve certain computational issues. Below a summary of some challenges that were faced is presented.

A script was developed in order to manage the control and ensemble runs into TUPÃ and SDUMONT supercomputers. These supercomputers work with a job queue system to organize the user's runs by priority, which depends on the number of cores, the time of computation, etc. The script sends all control and ensemble runs to the queue as jobs and waits until they finish, then MESOASSIM proceeds with the assimilation. Each one of these simulations are performed with 240 cores. In case of simulations with larger domains, the number of cores can be increased in the code.

Six grid configurations were used in the experiments with MESOASSIM and are shown in Table 4.1. In experiments with two nesting grids, the assimilation occurs only in the finest grid. Grid–A, Grid–C, Grid–D and Grid–E did not show good results in any of the experiments performed. The 2–way nested grids (Grid–D and Grid–E) only presented errors smaller than observations in the first data assimilation cycles. Experiments that used the Grid–C configuration showed noise in the west boundary of the grid, which contaminated the whole grid domain. The same behavior was observed in experiments with Grid–B. These noises in the grid lateral boundary were probably caused by the type of nesting grid since they were not observed in the 2-way nesting grids. Finally, experiments with strong lateral nudging (300 s) were attempted for both the Grid–B and Grid–C configurations. The Grid–B configuration was the only one that presented reasonable results and for this reason was selected as default for the next experiments.

*Table 4.1* - Grid configurations used in the MESOASSIM experiments.

| ID | Number of grids | Grid spacing | Nesting |
|---|---|---|---|
| Grid–A | 1 | 15 km | – |
| Grid–B | 2 | 16 km/8 km | 1-way |
| Grid–C | 2 | 16 km/4 km | 1-way |
| Grid–D | 2 | 16 km/8 km | 2-way |
| Grid–E | 2 | 16 km/4 km | 2-way |

Different approaches of assimilating infrared BT into BRAMS were attempted: cloud fraction; histogram of cloud top temperatures; and by considering each pixel one of GOES images as one observation. The cloud fraction and the cloud top temperature histogram did not work well, they caused an imbalance in MLEF, which lead to an overajustment in the control variables. One possible explanation for this problem is that these types of observations may not bring enough physical information to the assimilation algorithm. The experiments performed with BT assimilated by considering each pixel as one observation worked well and is used to continue this study.

Several control variable sets were tried in order to achieve a good performance with MESOASSIM. It was noted that when the control variable set had less then five variables, MLEF caused a model instability by overadjusting the control variables. MESOASSIM had a good performance with horizontal wind components as control variables. The wind vertical component did not help to the MLEF performance. With respect to the microphysical variables (hydrometeor mixing ratios and concentrations), the best result was obtained by selecting all of them as control variables. In summary, the best set found was: vapor mixing ratio, ice-liquid potential temperature, zonal and meridional wind components, Exner function, and mixing ratio and number concentration for all hydrometeors (cloud, drizzle, rain, pristine, snow, aggregates, graupel and hail).

### *4.2.2 Experiment design*

Two numerical experiments are performed with MESOASSIM for a case of MCS observed over the La Plata Basin on 21 September 2010: one without data assimilation (NoAssim) and other one with data assimilation (Analysis). The simulation starts at 12:00 UTC in 20 September 2010 with 17 hours of cold run (period without assimilation), one hour of assimilation interval and seven assimilation cycles. The assimilation cycle begins at 05:00 UTC and ends at 12:00 UTC on 21 September 2010.

The Analysis experiment is run with 32 ensemble members and 21 control variables. All BRAMS's prognostic variables are set as control variables, except the vertical velocity since it did not show good results in numerical tests. In this context, the control variable set consists of vapor mixing ratio, ice-liquid potential temperature, zonal and meridional wind components, Exner function, and mixing ratio e number concentration for all hydrometeor classes available in BRAMS-4.3 (cloud, drizzle, rain, pristine, snow, aggregates, graupel

and hail). The observational error is set as a BT of 25 K for all observations during the whole simulation, which means that this value is kept constant in the diagonal matrix $\boldsymbol{R}^{1/2}$ (square-root of observation error covariance). This error was chosen in order to keep the observation term of the cost function equation (Eq. 4.1) close to one, otherwise the algorithm may not work properly.

Two grids, nested 1-way, are set in the simulation with 16 (grid 1) and 8 km (grid 2) of grid spacing. Both grids are centered in the La Plata Basin and their sizes are 4800×5120 km (grid 1) and 1608×1576 km (grid 2). Figure 4.2 shows the model grids 1 and 2 as brown and blue boxes, respectively, whereas shaded area refers to the La Plata Basin topography elevation. The vertical domain extends to approximately 20 km with 45 levels with grid spacing ranging from 100 to 600 m and a 1.1 stretch ratio. Table 4.2 describes the main configuration of MESOASSIM framework. The data assimilation is done only in the finest grid.

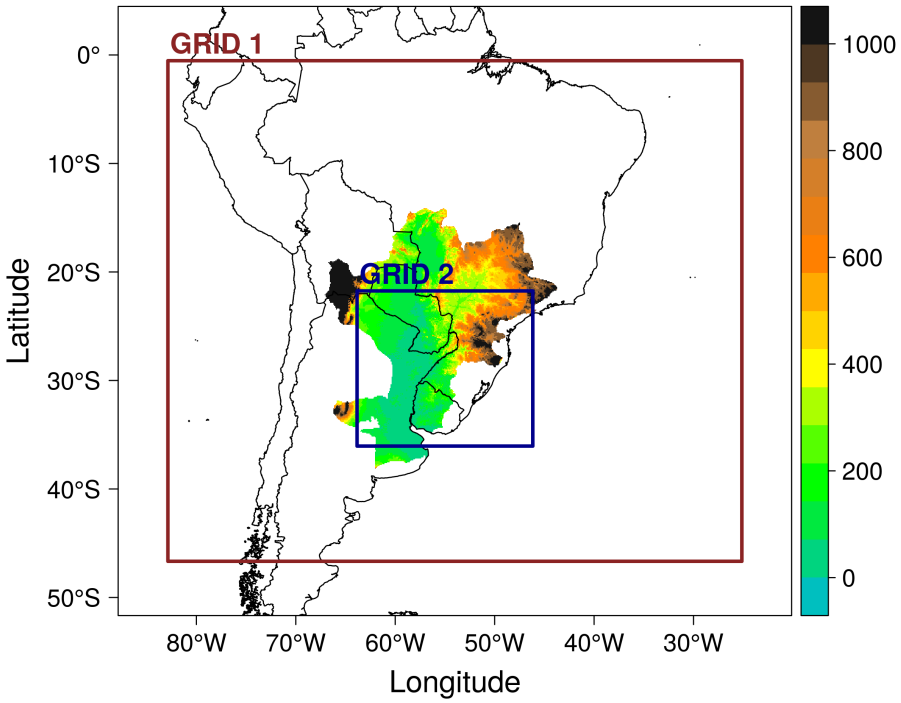


*Figure 4.2:* Model domain for 16 km (brown box) and 8 km (blue box) grid spacing. The topography elevation within the La Plata Basin region is shaded.

*Table 4.2* - Main configurations used in the simulations with MESOASSIM for the MCS case occurred on 21 September 2010.

| | |
|---|---|
| Number of points for lateral boundary nudging | 10 |
| Nudging time scale for lateral boundary | 300 s |
| Nudging time scale for the top of domain | 300 s |
| Lateral boundary condition | Klemp and Wilhelmson (1978) |
| Shortwave/Longwave radiation parametrization | Chen and Cotton (1987) |
| Turbulence parametrization | Mellor and Yamada (1982) |
| Convective parametrization (activated only for grid 1) | Grell (1993) |

The dataset used to initialize the atmospheric model is identical to that one described in Chapter 3: CFSR reanalysis, NDVI, heterogeneous soil moisture, sea surface temperature weekly averaged, topography, land use and soil texture. In addition, the MESOASSIM assimilates the brightness temperature at channel 10.7 $\mu$m (channel 4), retrieved by the satellite GOES 12. These data are downloaded in binary format from CPTEC/INPE by the link `http://satelite.cptec.inpe.br/pedidoweb/pedido.formulario.logic`.

## *4.3 Results*

Figure 4.3 shows the MCS observed on 21 September 2010 from 06:00 UTC (cycle 1) up to 12:00 UTC (cycle 7), where each cycle corresponds to the time that the respective BT observation is assimilated. The colors represent the brightness temperature at channel 10.7 $\mu$m retrieved by the satellite GOES 12. As can be seen in the figure, the MCS starts developing close to 05:00 UTC with two evident convective cells over southern Paraguay and western Rio Grande do Sul, Brazil. Then these cells begin to grow and merge, forming a large cloud shield that covers entirely the Rio Grande do Sul and Santa Catarina, Brazil, approximately at 10:00 UTC (cycle 6). The system seems to reach its maximum intensity near 09:00 UTC (cycle 5). After this time the MCS begins to decay.

The brightness temperature at channel 10.7 $\mu$m for NoAssim (experiment without data assimilation) is computed by CRTM for all data assimilation cycles and can be seen in Figure 4.4. By comparing Figure 4.4 against satellite observations (Figure 4.3), we can note that BRAMS is able to simulate the MCS's main mesoscale structure, although the convective cells over Northeast Argentina are not well simulated. Moreover, the model generated a convection in southern of Rio Grande do Sul state that was not observed in

the satellite images (Figure 4.3). The absence of an appropriate observational network to measure state variables (e.g., pressure, temperature, wind) over the La Plata Basin may partially contribute to the model errors. Nevertheless, the BRAMS's performance was reasonably since the model simulated the main system's life cycle and mesoscale structure.

Figure 4.5 is build similar to Figure 4.4, but regarding the Analysis experiment (experiment with data assimilation). This figure shows the BT computed from control variables, updated by MLEF after cost function minimization, for each data assimilation cycle. Contrasting Figures 4.4 and 4.5, it is possible to observe that the MCS from Analysis presents a shape closer to observations (Figure 4.3). However, Analysis does not represent the convection over South Paraguay and Northeast Argentina. MESOASSIM works to inhibit the clouds formation in the south flank of the MCS (close to Uruguay) and to produce colder BTs around the center of Rio Grande do Sul in cycles 5 and 6. Some erroneous adjustments of control variables are evident over Paraná, where MLEF seems to have intensified the convection. This may be explained by the proximity of the cloud cluster to the grid's lateral boundary. Boundary noises appear over the west border, close to Paraguay, and do not seem to compromise the MESOASSIM performance. These noises are probably caused by the 1-way nesting grid since they do not occur in 2-way nesting grid experiments (not shown here).

In order to highlight contrasts between the FGuess and Analysis experiments, the difference between them (i.e., $\mathrm{BT}_{Analysis}$-$\mathrm{BT}_{FGuess}$) are computed and depicted in Figure 4.6. It is possible to identify with more accuracy where MLEF changed the MCS structure in terms of BT. The highest correction values in magnitude are around 60 K over the vicinity of the system borders. MLEF did not adjust where there was not cloud formation, most part of adjustments were done in the MCS zone, where the biggest model errors are located. These results indicate that MLEF tends to correct more where is needed, which is really important for MESOASSIM performance.

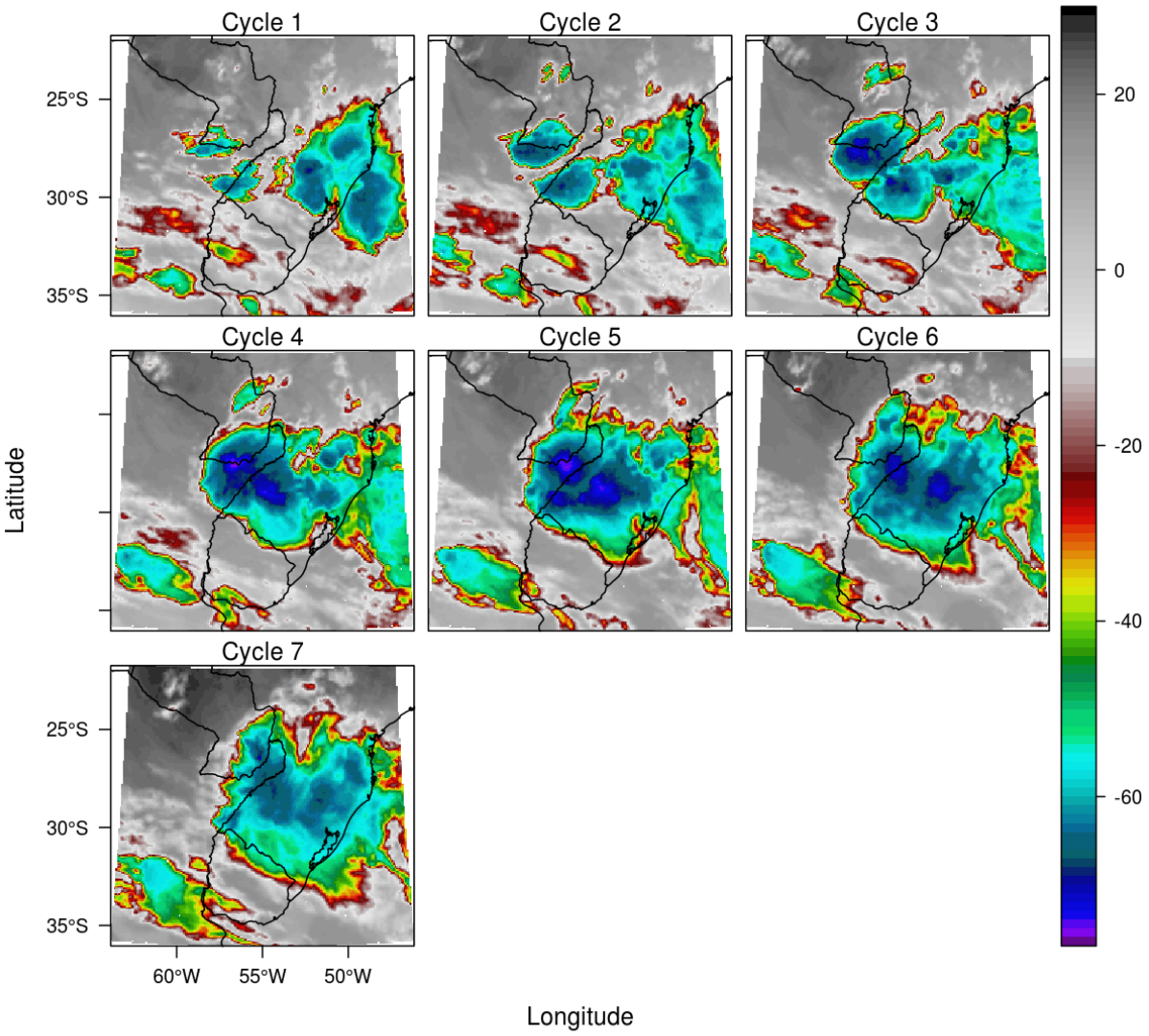


*Figure 4.3:* Infrared satellite data from GOES 12 for an MCS observed on 21 September 2010. Colors indicate the brightness temperature at channel 10.7 $\mu$m.

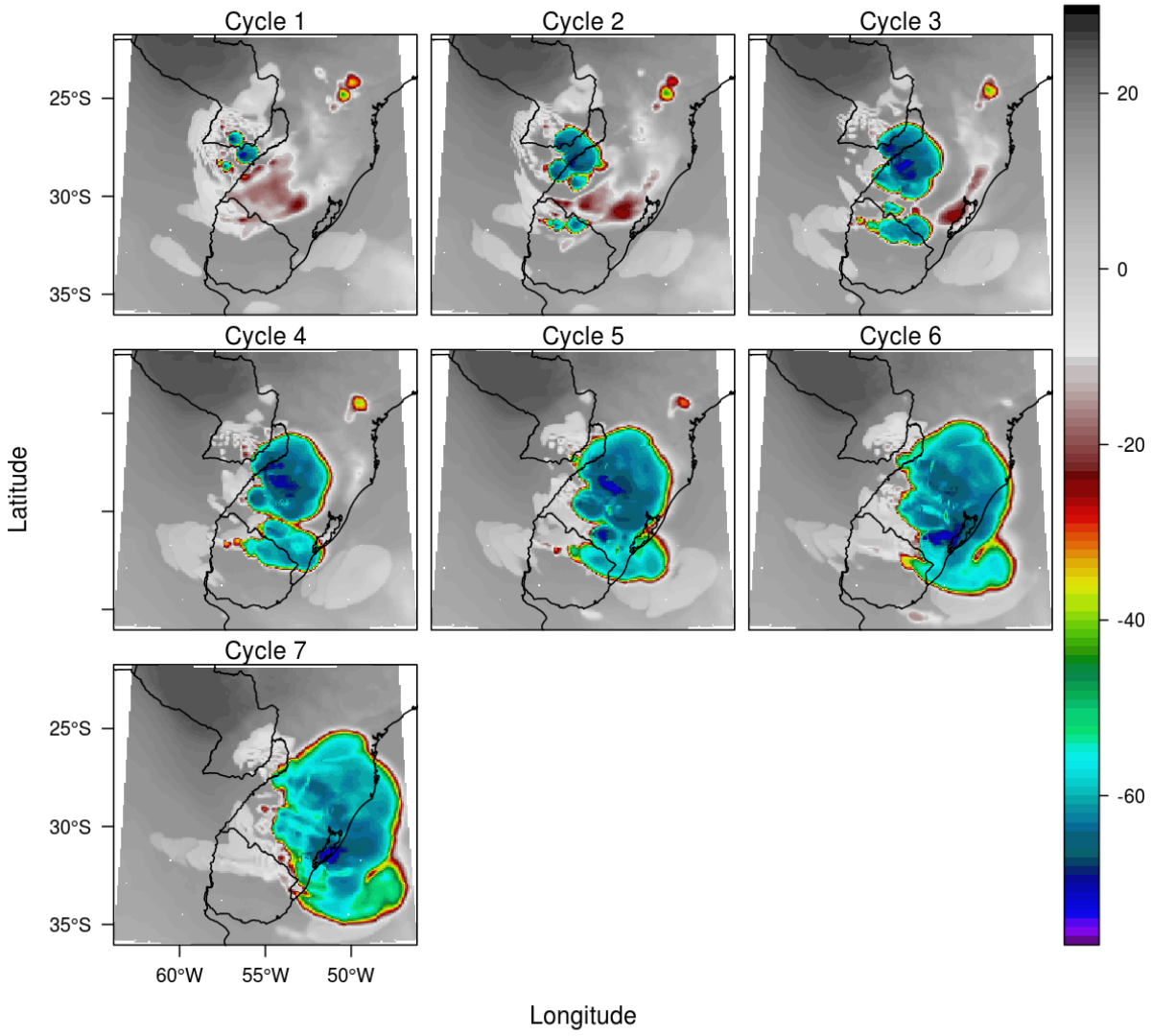


*Figure 4.4:* Synthetic infrared satellite images computed by CRTM for the NoAssim experiment from 06:00 UTC (cycle 1) up to 12:00 UTC (cycle 7), with one hour of interval. Colors indicate the brightness temperature at channel 10.7 $\mu$m.

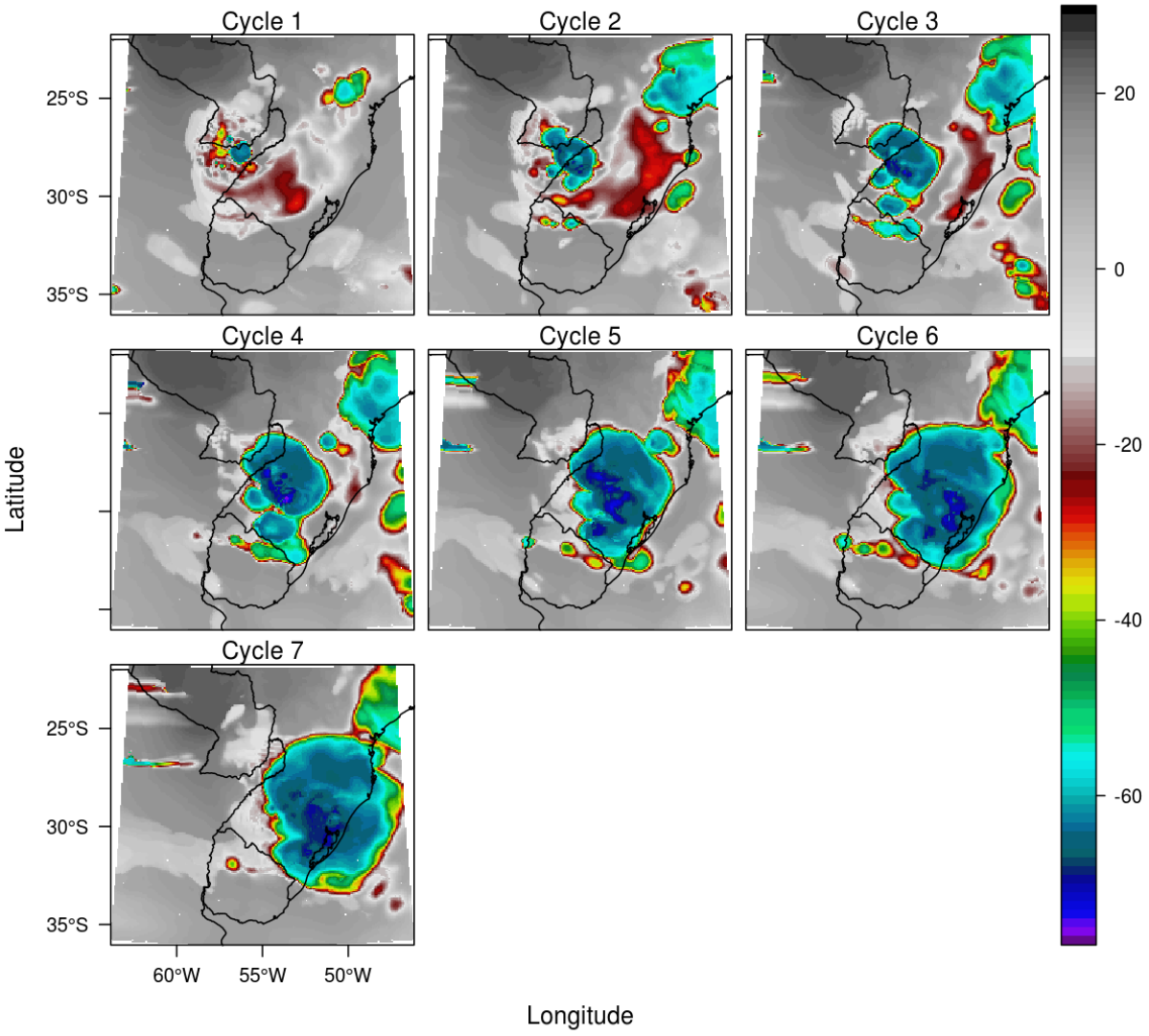


*Figure 4.5:* As in Figure 4.4, but for the Analysis experiment.

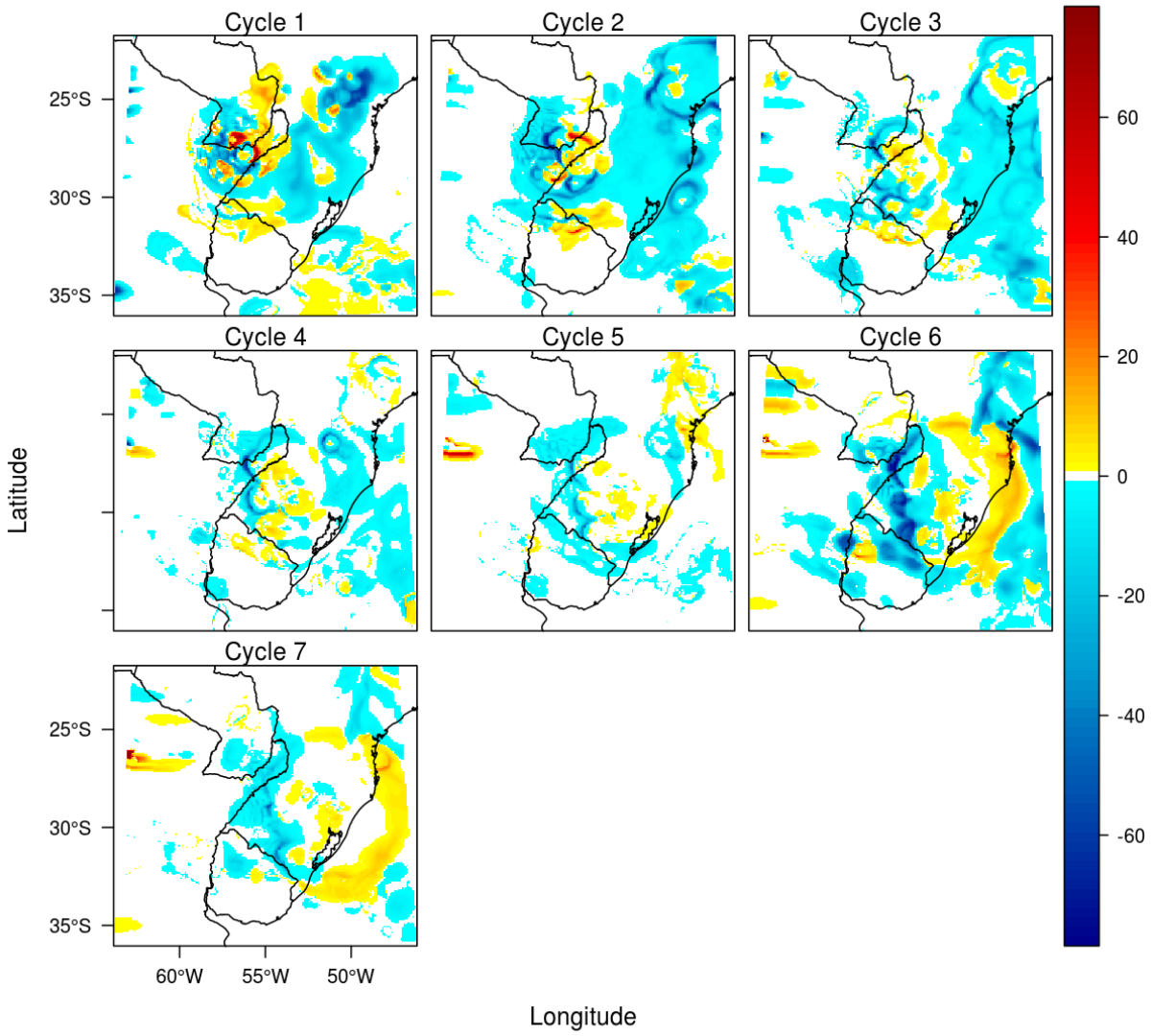


*Figure 4.6:* Difference between the BTs from the Analysis and FGuess experiments for all assimilation cycles (from 06:00 UTC up to 12:00 UTC, with one hour of interval).

The total cost function normalized by the number of observations (i.e., $\sum \boldsymbol{J}_f + \sum \boldsymbol{J}_{obs}/N_{obs}$, where $\boldsymbol{J}_f$ and $\boldsymbol{J}_{obs}$ refer to forecast and observation terms of the cost function described in Eq. 4.1, respectively) is depicted in Figure 4.7. The line colors indicate the respective minimization iteration where marigold represents the first iteration, green indicates the second iteration and red refers to the third iteration, whereas blue indicates the value of the total cost function before minimization. It is known that the smaller is the total cost function, the closer is the numerical simulation to observations. We observe that the total cost function presents bigger values between cycles 3 and 5, whereas smaller values are observed after cycle 5. As the minimization number increases, the total cost function decreases, although it is more significant before cycle 4. The highest values of the cost function are likely associated with the intense MCS's convective activity.

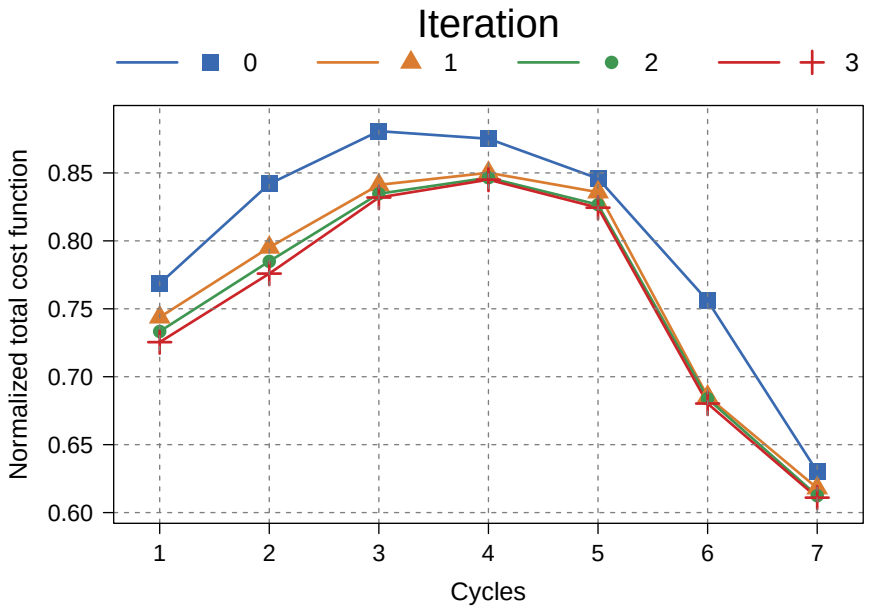


*Figure 4.7:* Total cost function normalized by the number of observations. Colors indicate the respective minimization iteration where marigold represents the first iteration, green indicates the second iteration and red refers to the third iteration. The color blue represents the total cost function before minimization.

Figure 4.8 compares the root mean square error (RMSE) of BT from NoAssim, FGuess and Analysis for all observations, computed as follows:

$$RMSE_{tot} = \sqrt{\sum_{i=1}^{N_{obs}} \frac{(y_i - H(x_i))^2}{N_{obs}}} \tag{4.9}$$

The FGuess refers to the fist guess brightness temperature that is computed from the Analysis experiment before the cost function minimization. Comparisons between Figures 4.8 and 4.7 show that they have similar shape, which is not a surprise since both represent the distance between simulation and observation. The Analysis experiment presents smaller $\text{RMSE}_{tot}$ than NoAssim for all assimilation cycles (Figure 4.8), although their errors are almost identical in cycle 5. When we compare FGuess and Analysis, it becomes evident that MLEF reduces the $\text{RMSE}_{tot}$ of the brightness temperature for all cycles, even though MLEF does not always improve the BRAMS's performance for the next cycle. For example, in cycles 3 and 4 the FGuess decreases less than NoAssim, indicating that the control variables adjusted by MLEF in cycle 3 were not capable of improving the next assimilation cycle. The same thing occurs between cycles 4 and 5. Besides this behavior, the MESOASSIM presents satisfactory outcomes.

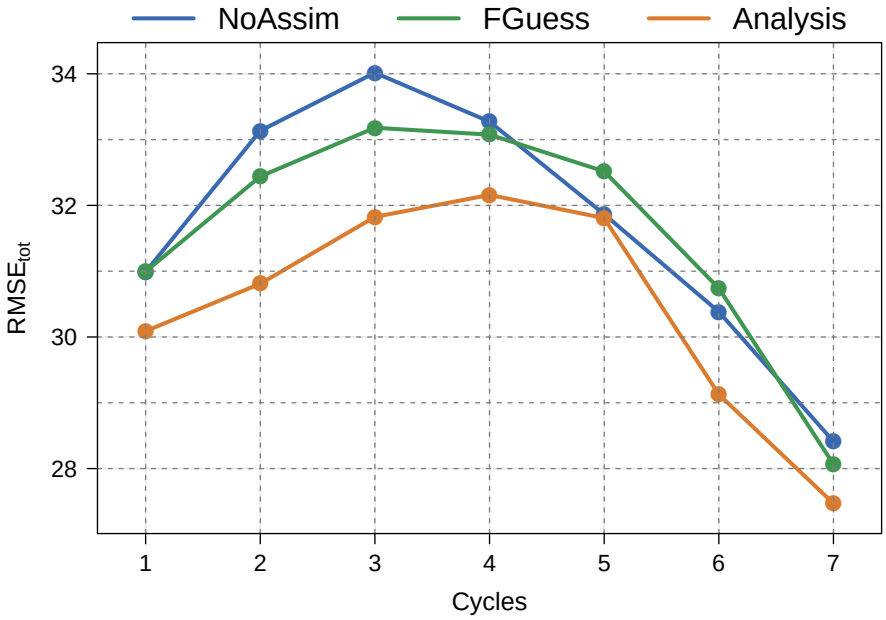


*Figure 4.8:* Root mean square error of BT from NoAssim, FGuess and Analysis for all observations. FGuess refers to the fist guess brightness temperature that is computed from Analysis before the cost function minimization.

In attempt to verify exclusively the performance of MESOASSIM regarding the MCS simulation, we computed the RMSE of BT over the MCS area ($RMSE_{mcs}$) for 58°W–46.2°W and 34°S–25°S (Figure 4.9). Larger errors are observed for $RMSE_{mcs}$ (Figure 4.9) when compared to $RMSE_{tot}$ (Figure 4.8), which is expected since the model biggest errors are located over the MCS area. Figure 4.9 shows that MLEF updates were not good enough to improve the model performance between cycles 3 and 5, as depicted in Figure 4.8. However, the absolute differences between NoAssim and Analysis $RMSE_{mcs}$ are greater than $RMSE_{tot}$, in other words, the MCS simulation of Analysis is even closer to the infrared satellite observations when compared to $RMSE_{tot}$.

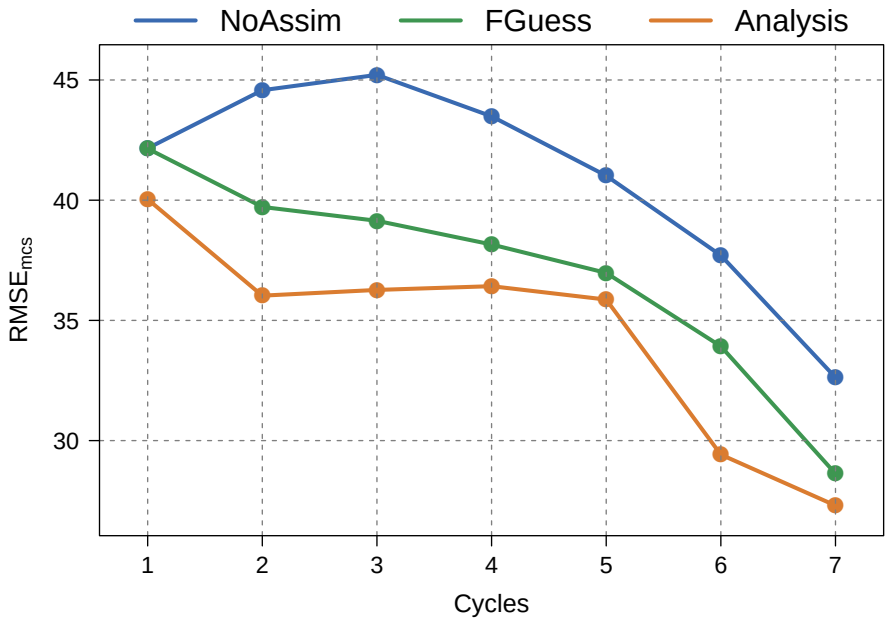


*Figure 4.9:* Root mean square error of BT from NoAssim, FGuess and Analysis over the MCS area (58°W–46.2°W and 34°S–25°S). The Fguess refers to the fist guess brightness temperature that is computed from Analysis before the cost function minimization.

The five strongest updrafts and downdrafts of the NoAssim and Analysis experiments are averaged for each assimilation cycle (Figure 4.10), except for the first one since the vertical velocity is not a control variable and, thereby it is not affected by MLEF updates in this cycle. By comparing the NoAssim and Analysis experiments, it is evident that MESOASSIM intensified the convection in all cycles, except in cycle 3 for updrafts and cycle 4 for downdrafts. In cycle 2 (07:00 UTC) occurs the largest contrasts between NoAssim and Analysis for both updraft and downdraft, with absolute differences around 3 m/s and 7 m/s, respectively. It is important to highlight that even though the vertical velocity is not a control variable, it shows an expressive response to BT assimilation.

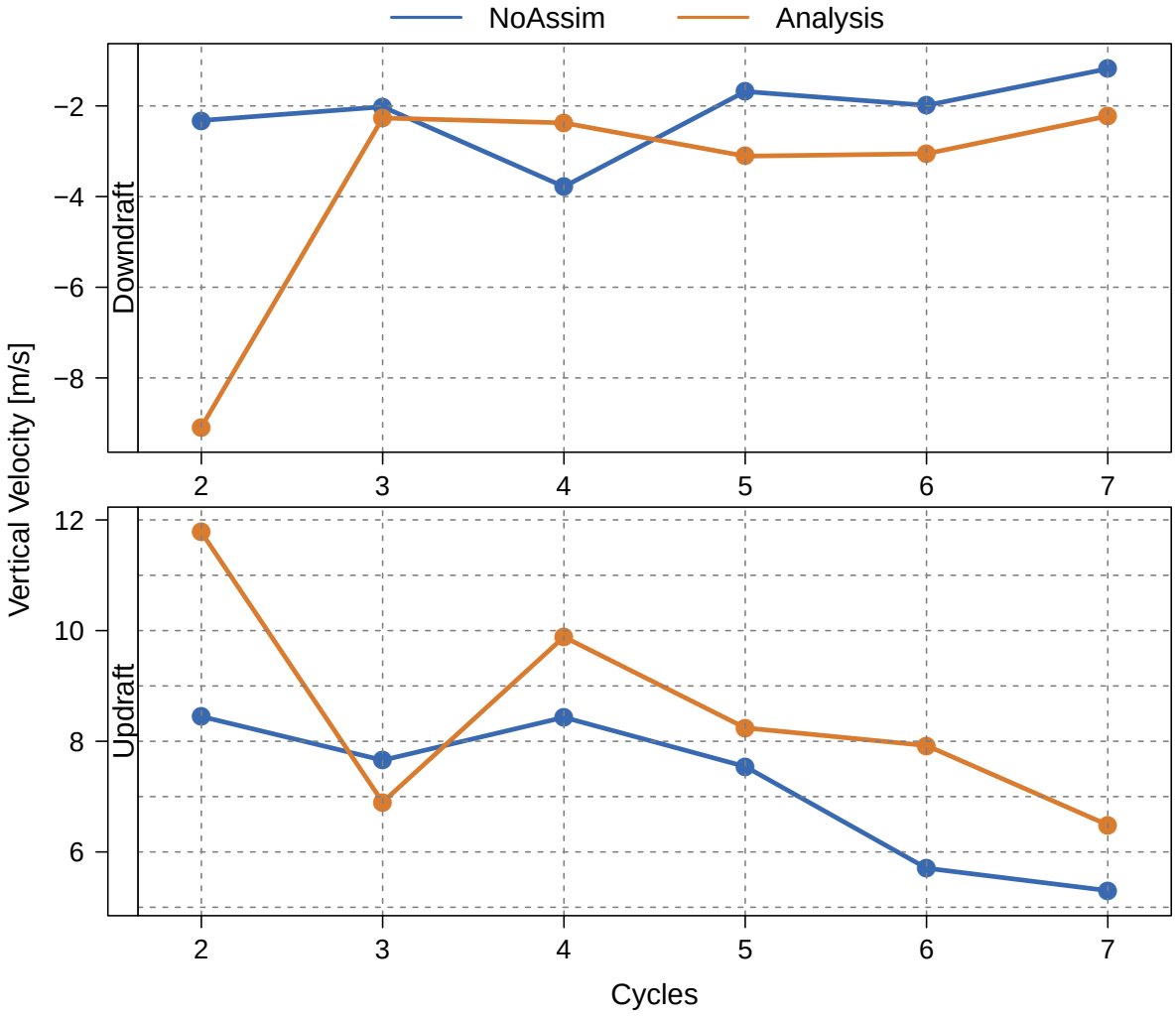


*Figure 4.10:* Average of the five strongest updrafts and downdrafts of the NoAssim and Analysis experiments for each assimilation cycle, except for the first one.

Synoptic fields related to the NoAssim (left-hand panels) and Analysis (right-hand panels) experiments are shown in Figures 4.11, 4.12, 4.13 and 4.14 for cycle 4 (09:00 UTC). The wind field at 2 km height is presented by Figure 4.11 where the wind direction is represented by vectors and its magnitude (m/s) is shaded. Expressive contrasts between NoAssim and Analysis are verified over South Brazil and North Argentina, where the low level jet is intensified with its maximum velocity displaced toward the northwest. The highest differences in the wind direction are observed over west part of Rio Grande do Sul state, where the MCS is located. Figure 4.12 compares the vapor mixing ratio fields in g/kg at 2 km height for NoAssim and Analysis. In general, the experiment with data assimilation shows a moister environment, specially over the MCS location (Figure 4.5). Looking at ice-liquid potential temperature at height of 2 km (Figure 4.13), slight differences appear over South Brazil, in particular over the zone where MCS is located. The high level wind is depicted in Figure 4.14 (similar to Figure 4.11, but at 10 km height). A displacement of the jet core toward the northwest is evident when the NoAssim and Analysis fields are analyzed as well as a wind strengthening in Rio Grande do Sul (intensifying the high level divergence related to MCS) and a wind weakening in Paraná. The stronger winds over Rio Grande do Sul increase divergence at the top of atmosphere, which may contribute to the updraft intensification shown in Figure 4.10.

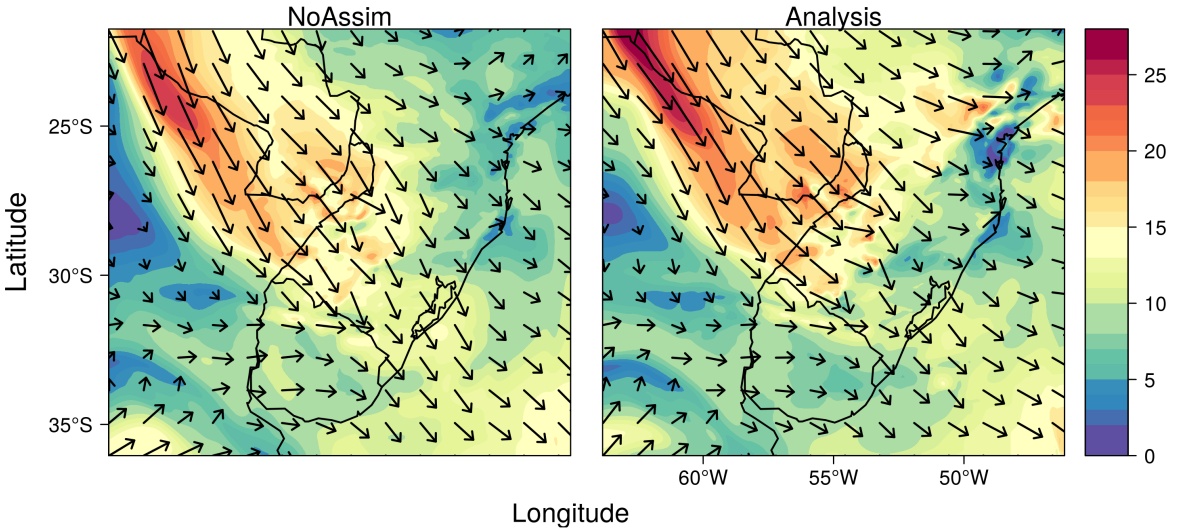


*Figure 4.11:* Wind field at 2 km height for the NoAssim (left panel) and Analysis (right panel) experiments. The wind direction is represented by vectors and its magnitude (m/s) is shaded.

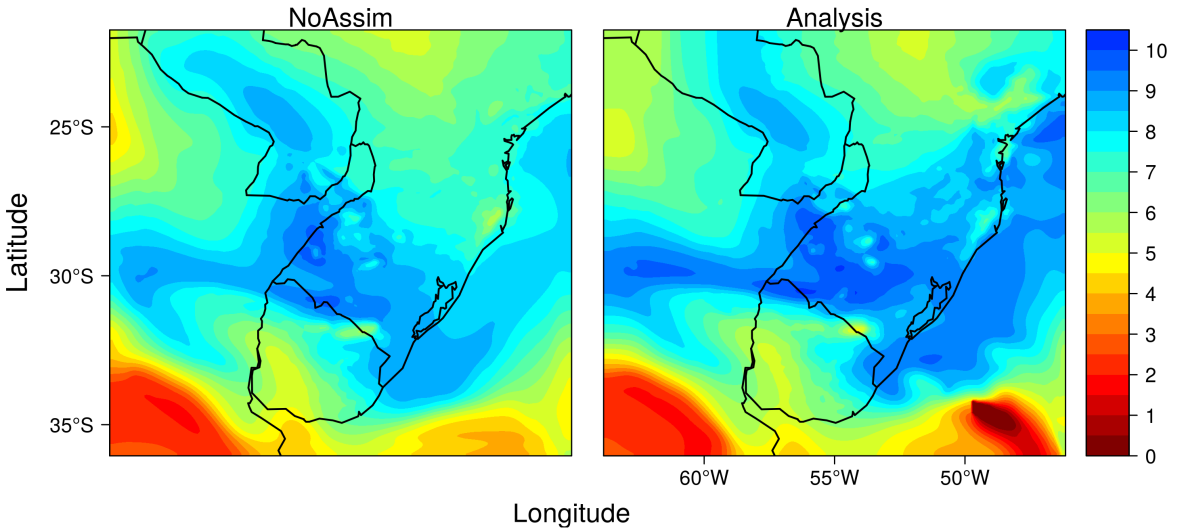


*Figure 4.12:* Vapor mixing ratio (g/kg) at 2 km height for the NoAssim (left panel) and Analysis (right panel) experiments.

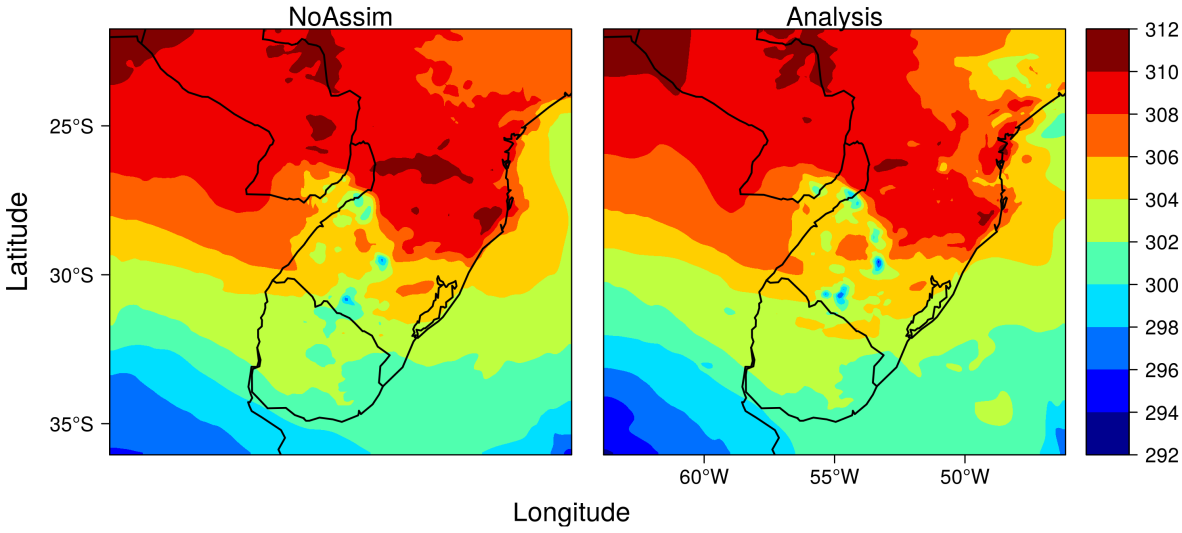


*Figure 4.13:* Ice-liquid potential temperature (K) at 2 km height for the NoAssim (left panel) and Analysis (right panel) experiments.

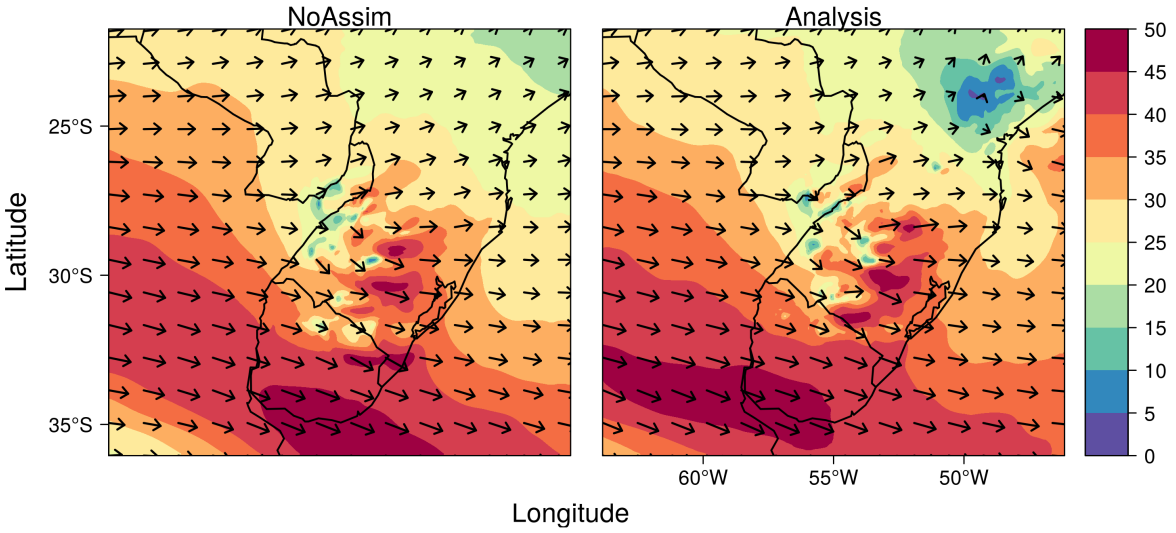


*Figure 4.14:* Wind field at 10 km height for the NoAssim (left panel) and Analysis (right panel) experiments. The wind direction is represented by vectors and its magnitude (m/s) is shaded.

Figure 4.15 shows the accumulated precipitation from 06:00 UTC (cycle 1) to 12:00 UTC (cycle 7) computed from the TRMM–3B42's precipitation product and the NoAssim and Analysis experiments. Both experiments do not simulate the precipitation shown by TRMM over Argentina (domain's southwest corner) and do produce rain over Paraná state that is not observed in TRMM's precipitation field. Also, the two simulations exhibit larger amounts of precipitation than TRMM, although TRMM may underestimate the real precipitation (Su et al., 2008). Despite errors, both simulations are able to generate the precipitation shown by TRMM–3B42 over the zone where MCS is located. Moreover, the Analysis experiment produces more precipitation than NoAssim over center and northwest zones of Rio Grande do Sul, as is observed in TRMM's precipitation.

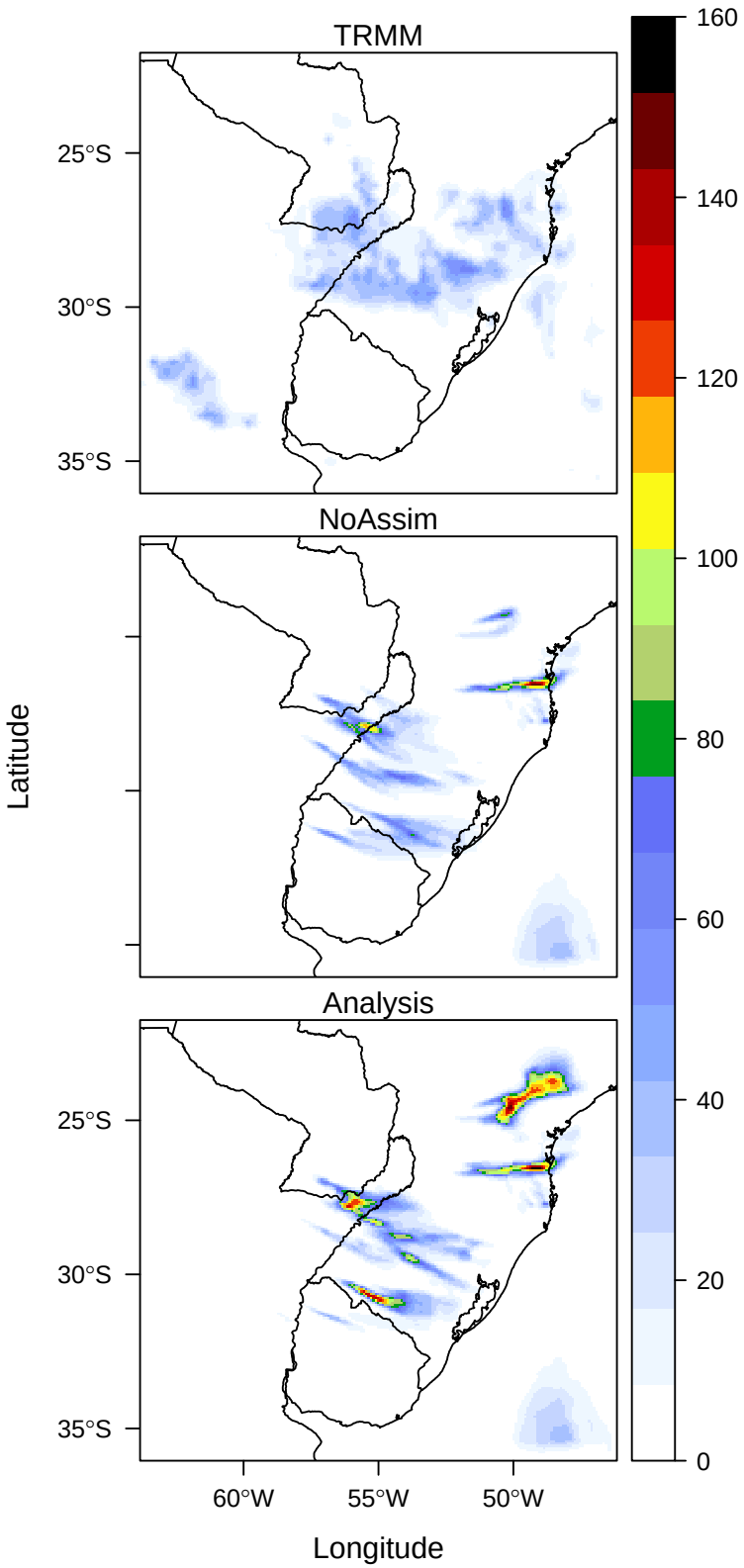


*Figure 4.15:* Accumulated precipitation from 06:00 UTC (cycle 1) to 12:00 UTC (cycle 7) computed from the TRMM-3B42's precipitation product and the NoAssim and Analysis experiments.

## 4.4 Conclusions

A mesoscale coupled framework of BRAMS–MLEF was developed in order to improve numerical simulations. This framework is called Mesoscale Assimilation system (MESOASSIM) and can assimilate brightness temperature at channel 4 (10.7 $\mu$m) from satellite GOES-12. As a first step, two experiments were performed with MESOASSIM for an MCS event observed over the La Plata Basin on 21 September 2010. One experiment was run without data assimilation (NoAssim), whereas the other one was run with data assimilation (Analysis).

MLEF did not represent part of the MCS convection, located over Paraguay and Northeast Argentina and did insert erroneous adjustments over Paraná, which may be caused by the proximity with the domain's border. Nonetheless, the MCS from Analysis showed a cloud shield shape closer than NoAssim to observations. In addition, the Analysis experiment presented smaller errors than NoAssim in all assimilation cycles for $\mathrm{RMSE}_{tot}$ and, specially, for $\mathrm{RMSE}_{mcs}$. In other words, MLEF tends to adjust more where errors are bigger.

The vertical velocity showed a significant response to the data assimilation, even though this variable was not included in the control variable set. EnsDA was able to intensify both updraft and downdraft, reaching absolute differences of 3 m/s and 7 m/s, respectively. Furthermore, MLEF was capable of intensifying the low level jet and displacing the high level jet core as well as increasing the moisture and changing the temperature gradient at 2 km, specially over MCS's area and surroundings.

Accumulated precipitation comparisons showed that both the NoAssim and Analysis experiments generated more precipitation than was produced by the TRMM–3B42 product. However, as shown by Su et al. (2008), the TRMM–3B42 precipitation product may underestimate rainfall amounts. The experiment with data assimilation produced more precipitation than NoAssim over center and northwest of Rio Grande do Sul state and over Northeast Argentina, as it was observed in TRMM–3B42 precipitation product.

The non-state variable assimilation is a really complex issue, specially for highly non-linear models. Nevertheless, in summary, MESOASSIM framework improved the numerical simulation, decreasing the distance between model results and satellite observations. The methodology presented here is a first step toward the mesoscale data assimilation in

BRAMS. In the future, it is intended to assimilate other GOES satellite channels and other types of data as well as for incorporating new methods to generate ensemble members.

Chapter 5

# Main conclusions and future work

This study sought to understand how aerosols from biomass burning in the Amazon Basin may interact with MCSs that form over the La Plata Basin during the spring. To accomplish this issue, this study was divided in three parts. The first part is related to an observational analysis and was presented in Chapter 2. The second part addressed the numerical study of an MCS case and was shown in Chapter 3. The last part is presented in Chapter 4 and refers to an attempt to assimilate infrared satellite data.

The observational study (Chapter 2) was carried out by using three statistical tools and dataset from AERONET, Reanalyses 2 and TRMM-3B42. Interesting results were achieved and the main conclusion are presented as follows:

1. The dynamic component appears as the principal rain forcing, although the aerosols also have a relevant contribution;

2. It was possible to detect the aerosol effect under weak upward motion scenarios, where higher AOD values are related to rain suppression;

3. The fist eigenvector captured the dynamic forcing, where negative $\omega$ and positive RH are related to amounts of precipitation above average;

4. The second eigenvector identified rain suppression associated with the aerosol forcing, where positive values of AOD are followed by negative values of precipitation.

By using the atmospheric model BRAMS–4.3, numerical simulations were performed for a case of MCS observed on 21 September 2010 during the spring (Chapter 3). An important link between the aerosol effect and MCS's dynamics was verified. The main conclusion are presented below:

1. Greater amounts of precipitation covering larger areas were produced in environments with higher aerosol loadings;

2. The supercooled liquid water availability was larger as the CCN concentration increased, which leaded to an increase in the number of ice particles;

3. A reduction in the riming efficiency weakened the updrafts at mixing levels and displaced the updraft velocity peak aloft, under high CCN concentrations;

4. Stronger downdrafts were observed under higher CCN concentration, being associated with an increase in the number of updraft cells and the corresponding area covered.

In attempt to improve the model simulations for expanding the understanding of MCS–CCN interaction, the Mesocale Assimilation system was developed. This system is a coupling of BRAMS–MLEF and is addressed to assimilate brightness temperature at channel 10.7 $\mu$m from GOES 12. The main results about MESOASSIM performance are shown below:

1. The shape of the MCS's cloud shield from Analysis was closer to observations when compared to NoAssim;

2. The Analysis experiment showed smaller errors than NoAssim in all assimilation cycles, especially over the MCS zone;

3. Updrafts and downdrafts were intensified by MLEF;

4. MLEF strengthened the low-level jet as well as displaced the high level jet;

5. The data assimilation algorithm increased the vapor content, and changed the temperature gradient at 2 km height, especially over the MCS's area and surroundings;

6. The Analysis experiment produced more precipitation than the NoAssim experiment over the center and northwest of Rio Grande do Sul state and over the northeast of Argentina, as it was observed in the TRMM–3B42 precipitation product.

In summary, the observational and numerical studies (Chapters 2 and 3) presented contrasting results. The first one showed rain suppression as aerosol increased, whereas

the second one presented the opposite behavior. It is important to highlight that Chapter 2 showed an statistical analysis from observation and analyzed several cases of rain in 12 years, whereas Chapter 3 referred to a modeling study for one case of a nocturnal MCS. In addition, the model BRAMS–4.3 takes into account only the aerosol microphysical effect, and the observational results might be influenced by others effects of aerosols such as radiative and composition. The aerosol effects are also sensitive to environmental conditions, which may have contributed to the results. Indeed, the aerosol effects in large cloud clusters such as MCSs are really complex and highly nonlinear. Hence, it was tried to improve the model simulation by assimilating infrared satellite observations through the MESOASSIM framework. This approach worked well and MESOASSIM showed good performance in the experiments. CCN experiments with the improved simulation will be performed in future work.

## *5.1 Future work*

The results presented in this research encourage the development of future works as follows:

- To extend the period of the observational analysis and to use other types of data sets.
- To activate the radiative effect of aerosols in the atmospheric model in order to evaluate its impact on MCSs.
- To implement a nucleation scheme in the microphysical parametrization that considers aerosol chemical composition. This scheme was implemented in experimental versions of the RAMS and OLAM models.
- To simulate other MCS cases observed over the La Plata Basin during spring and to verify how other cases are related to the observational analysis.
- To perform CCN experiments with the improved simulation generated by MESOASSIM.
- To assimilate other types of data such as radar and surface stations.

- To implement other methods for computing ensemble members as lagged forecast and spatial covariance.

## *5.2 Final statement*

The present work represents a first attempt to study the cloud microphysical-dynamical interaction for mesoscale convective systems observed over the La Plata Basin, particularly with respect to the role of biomass burning aerosols originated in the Amazon Basin and Central Brazil during the end of the dry season.

Observations indicate a pattern where an impact of aerosol is seen as a suppression of rainfall in MCSs observed in the La Plata Basin. For a specific case, the aerosol induces an enhancement of cloud dynamics indicators such as updrafts and downdrafts. Deficiencies in the initial state, provided by large scale analysis, have prompted the development of a mesoscale assimilation system that indicates quite promising results, which will be explored further in future work. These novel results point to important aspects on the impact of biomass burning aerosols on mesoscale convective systems, particularly in the case of the systems observed in the La Plata Basin.

# Bibliography


Albrecht B. A., Aerosols, cloud microphysics, and fractional cloudiness, Science, 1989, vol. 245, p. 1227

Albrecht R. I., Goodman S. J., Buechler D. E., Blakeslee R. J., Christian H. J., Where are the lightning hotspots on Earth?, Bulletin of the American Meteorological Society, 2016

Albrecht R. I., Morales C. A., Silva Dias M. A. F., Electrification of precipitating systems over the Amazon: Physical processes of thunderstorm development, Journal of Geophysical Research, 2011, vol. 116, p. D08209

Anabor V., Stensrud D. J., de Moraes O. L. L., Serial Upstream-Propagating Mesoscale Convective System Events over Southeastern South America, Monthly weather review, 2008, vol. 136, p. 3087

Andreae M. O., Rosenfeld D., Artaxo P., Costa A., Frank G., Longo K., SILVA DIAS M., Smoking rain clouds over the Amazon, Science, 2004, vol. 303, p. 1337

Apodaca K., Zupanski M., DeMaria M., Knaff J. A., Grasso L. D., Development of a hybrid variational-ensemble data assimilation technique for observed lightning tested in a mesoscale model, Nonlinear Processes in Geophysics, 2014, vol. 21, p. 1027

Artaxo P., Martins J. V., Yamasoe M. A., Procópio A. S., Pauliquevis T. M., Andreae M. O., Guyon P., Gatti L. V., Leal A. M. C., Physical and chemical properties of aerosols in the wet and dry season in Rondônia, Amazonia, Journal of Geophysical Research, 2002, vol. 107, p. 8081

Artaxo P., Rizzo L. V., Brito J. F., Barbosa H. M., Arana A., Sena E. T., Cirino G. G., Bastos W., Martin S. T., Andreae M. O., Atmospheric aerosols in Amazonia and land

use change: from natural biogenic to biomass burning conditions, Faraday discussions, 2013, vol. 165, p. 203

Bei N., Li G., Meng Z., Weng Y., Zavala M., Molina L., Impacts of using an ensemble Kalman filter on air quality simulations along the California–Mexico border region during Cal–Mex 2010 Field Campaign, Science of the Total Environment, 2014, vol. 499, p. 141

Buehner M., McTaggart-Cowan R., Beaulne A., Charette C., Garand L., Heilliette S., Lapalme E., Laroche S., Macpherson S. R., Morneau J., et al., Implementation of deterministic weather forecasting systems based on ensemble–variational data assimilation at Environment Canada. Part I: The global system, Monthly Weather Review, 2015, vol. 143, p. 2532

Camponogara G., SILVA DIAS M. A. F., Carrió G. G., Relationship between Amazon biomass burning aerosols and rainfall over the La Plata Basin, Atmospheric Chemistry and Physics, 2014, vol. 14, p. 4397

Carrió G., Cotton W., Cheng W., Urban growth and aerosol effects on convection over Houston: Part I: The August 2000 case, Atmospheric Research, 2010, vol. 96, p. 560

Carrió G. G., Cotton W. R., Urban growth and aerosol effects on convection over Houston. Part II: Dependence of aerosol effects on instability, Atmospheric Research, 2011, vol. 102, p. 167

Carrió G. G., Cotton W. R., Loftus A., On the response of hailstorms to enhanced CCN concentrations, Atmospheric Research, 2014, vol. 143, p. 342

Carrió G. G., Cotton W. R., Zupanski D., Zupanski M., Development of an aerosol retrieval method: Description and preliminary tests, Journal of Applied Meteorology and Climatology, 2008, vol. 47, p. 2760

Chen C., Cotton W., The physics of the marine stratocumulus-capped mixed layer, Journal of the Atmospheric Sciences, 1987, vol. 44, p. 2951

Chen Y., Weng F., Han Y., Liu Q., Validation of the community radiative transfer model by using CloudSat data, Journal of Geophysical Research: Atmospheres, 2008, vol. 113

Conforte J. C., Um estudo de complexos convectivos de mesoescala sobre a América do Sul, São José dos Campos: Instituto Nacional de Pesquisas Espaciais, 1997, Ph.D. Thesis, 140

Cotton W. R., Pielke R. A., Walko R. L., Liston G. E., Tremback C. J., Jiang H., McAnelly R. L., Harrington J. Y., Nicholls M. E., Carrio G. G., Mcfadden J. P., RAMS 2001: Current status and future directions, Meteorology and Atmospheric Physics, 2003, vol. 82, p. 5

Durkee J. D., Mote T. L., A climatology of warm-season mesoscale convective complexes in subtropical South America, International Journal of Climatology, 2010, vol. 30, p. 418

Dye J. E., Knight C. A., Toutenhoofd V., Cannon T. W., The mechanism of precipitation formation in northeastern Colorado cumulus III. Coordinated microphysical and radar observations and summary, Journal of the Atmospheric Sciences, 1974, vol. 31, p. 2152

Eck T. F., Holben B. N., Slutsker I., Setzer A., Measurements of irradiance attenuation and estimation of aerosol single scattering albedo for biomass burning, Journal of Geophysical Research, 1998, vol. 103, p. 31

Erdal D., Cirpka O. A., Joint inference of groundwater–recharge and hydraulic–conductivity fields from head data using the ensemble Kalman filter, Hydrology and Earth System Sciences, 2016, vol. 20, p. 555

Evensen G., Sequential data assimilation with a nonlinear quasi-geostrophic model using Monte Carlo methods to forecast error statistics, Journal of Geophysical Research: Oceans, 1994, vol. 99, p. 10143

Evensen G., The ensemble Kalman filter: Theoretical formulation and practical implementation, Ocean dynamics, 2003, vol. 53, p. 343

Fan J., Yuan T., Comstock J. M., Ghan S., Khain A., Leung L. R., Li Z., Martins V. J., Ovchinnikov M., Dominant role by vertical wind shear in regulating aerosol effects on deep convective clouds, Journal of Geophysical Research: Atmospheres (1984–2012), 2009, vol. 114

Fan J., Zhang R., Li G., Tao W.-K., Effects of aerosols and relative humidity on cumulus clouds, Journal of Geophysical Research: Atmospheres (1984–2012), 2007, vol. 112

Freitas S. R., Longo K. M., Dias M. A. S., Dias P. L. S., Chatfield R., Prins E., Artaxo P., Grell G. A., Recuero F. S., Monitoring the transport of biomass burning emissions in South America, Environmental Fluid Mechanics, 2005, vol. 5, p. 135

Freitas S. R., Panetta J., Longo K. M., Rodrigues L. F., Moreira D. S., Rosário N. E., Dias P. L. S., Dias M. A. S., Souza E. P., Freitas E. D., et al., The Brazilian developments on the Regional Atmospheric Modeling System (BRAMS 5.2): an integrated environmental model tuned for tropical areas, Geoscientific Model Development, 2017, vol. 10, p. 189

Fritsch J. M., Forbes G. S., Mesoscale Convective Systems, Severe Convective Storms, Meteorological Monographs, 2001, pp 323–356

Gonçalves W. A., Machado L. A. T., Kirstetter P.-E., Influence of biomass aerosol on precipitation over the Central Amazon: an observational study, Atmospheric Chemistry and Physics, 2015, vol. 15, p. 6789

Grell G. A., Prognostic evaluation of assumptions used by cumulus parameterizations, Monthly Weather Review, 1993, vol. 121, p. 764

Guyon P., Graham B., Beck J., Boucher O., Gerasopoulos E., Mayol-Bracero O., Roberts G., Artaxo P., Andreae M., Physical properties and concentration of aerosol particles over the Amazon tropical forest during background and biomass burning conditions, Atmospheric Chemistry and Physics, 2003, vol. 3, p. 951

Hill G. E., Factors controlling the size and spacing of cumulus clouds as revealed by numerical experiments, Journal of the Atmospheric Sciences, 1974, vol. 31, p. 646

Hobbs P. V., Politovich M. K., Radke L. F., The structures of summer convective clouds in eastern Montana. I: Natural clouds, Journal of Applied Meteorology, 1980, vol. 19, p. 645

Holben B. N., Eck T. F., Slutsker I., Tanre D., Buis J. P., Setzer A., Vermote E., Reagan J. A., Kaufman Y. J., Nakajima T., Lavenu F., Jankowiak I., Smirnov A., AERONET –

A federated instrument network and data archive for aerosol characterization, Remote sensing of environment, 1998, vol. 66, p. 1

Houtekamer P. L., Deng X., Mitchell H. L., Baek S.-J., Gagnon N., Higher resolution in an operational ensemble Kalman filter, Monthly Weather Review, 2014, vol. 142, p. 1143

IPCC Climate Change 2007: Contribution of Working Group I to the Fourth Assessment Report of the Intergovernmental Panel on Climate Change. Cambridge University Press Cambridge, United Kingdom and New York, NY, USA, 2007, 996

Jones T., Christopher S., Statistical properties of aerosol-cloud-precipitation interactions in South America, Atmospheric Chemistry and Physics, 2010, vol. 10, p. 2287

Kalnay E., Atmospheric modeling, data assimilation and predictability. Cambridge university press, 2003

Kanamitsu M., Ebisuzaki W., Woollen J., Yang S.-K., Hnilo J. J., Fiorino M., Potter G. L., Ncep-doe amip-ii reanalysis (r-2), Bulletin of the American Meteorological Society, 2002, vol. 83, p. 1631

Khain A. P., BenMoshe N., Pokrovsky A., Factors determining the impact of aerosols on surface precipitation from clouds: An attempt at classification, Journal of the Atmospheric Sciences, 2008, vol. 65, p. 1721

Klemp J. B., Wilhelmson R. B., The simulation of three-dimensional convective storm dynamics, Journal of the Atmospheric Sciences, 1978, vol. 35, p. 1070

Koren I., Kaufman Y. J., Remer L. A., Martins J. V., Measurement of the effect of Amazon smoke on inhibition of cloud formation, Science, 2004, vol. 303, p. 1342

Koren I., Martins J. V., Remer L. A., Afargan H., Smoke invigoration versus inhibition of clouds over the Amazon, Science, 2008, vol. 321, p. 946

Lavaysse C., Carrera M., Bélair S., Gagnon N., Frenette R., Charron M., Yau M., Impact of surface parameter uncertainties within the Canadian regional ensemble prediction system, Monthly Weather Review, 2013, vol. 141, p. 1506

Lebo Z. J., Morrison H., Dynamical effects of aerosol perturbations on simulated idealized squall lines, Monthly Weather Review, 2014, vol. 142, p. 991

Li L., Zhou H., Gómez-Hernández J. J., Franssen H.-J. H., Jointly mapping hydraulic conductivity and porosity by assimilating concentration data via ensemble Kalman filter, Journal of hydrology, 2012, vol. 428, p. 152

Lilly D. K., On the numerical simulation of buoyant convection, Tellus, 1962, vol. 14, p. 148

Lin J. C., Matsui T., Pielke Sr R., Kummerow C., Effects of biomass-burning-derived aerosols on precipitation and clouds in the Amazon Basin: A satellite-based empirical study, Journal of geophysical research, 2006, vol. 111, p. D19204

Loftus A. M., Cotton W., Carrió G. G., A triple-moment hail bulk microphysics scheme. Part I: Description and initial evaluation, Atmospheric Research, 2014, vol. 149, p. 35

Machado L. A. T., Rossow W. B., Guedes R. L., Walker A. W., Life cycle variations of mesoscale convective systems over the Americas, Monthly Weather Review, 1998, vol. 126, p. 1630

McMillan H. K., Hreinsson E., Clark M. P., Singh S. K., Zammit C., Uddstrom M. J., Operational hydrological data assimilation with the recursive ensemble Kalman filter, Hydrology and Earth System Sciences, 2013, vol. 17, p. 21

Maddox R. A., Mesoscale convective complexes, American Meteorological Society, Bulletin, 1980, vol. 61, p. 1374

Mahrer Y., Pielke R. A., A numerical study of the airflow over irregular terrain, Beiträge zur Physik der Atmosphäre, 1977, vol. 50, p. 98

Marengo J. A., Douglas M. W., Silva Dias P. L., The South American low-level jet east of the Andes during the 1999 LBA-TRMM and LBA-WET AMC campaign, Journal of Geophysical Research, 2002, vol. 107, p. 8079

Martin S. T., Andreae M. O., Artaxo P., Baumgardner D., Chen Q., Goldstein A. H., Guenther A., Heald C. L., Mayol-Bracero O. L., McMurry P. H., et al., Sources and properties of Amazonian aerosol particles, Reviews of Geophysics, 2010, vol. 48

Martins J. A., Silva Dias M. A. F., Gonçalves F. L. T., Impact of biomass burning aerosols on precipitation in the Amazon: A modeling case study, Journal of Geophysical Research, 2009, vol. 114

Mellor G. L., Yamada T., Development of a turbulence closure model for geophysical fluid problems, Reviews of Geophysics, 1982, vol. 20, p. 851

Meyers M. P., Walko R. L., Harrington J. Y., Cotton W. R., New RAMS cloud microphysics parameterization. Part II: The two-moment scheme, Atmospheric Research, 1997, vol. 45, p. 3

Morton D., Defries R., Randerson J., Giglio L., Schroeder W., Van Der Werf G., Agricultural intensification increases deforestation fire activity in Amazonia, Global Change Biology, 2008, vol. 14, p. 2262

Nesbitt S. W., Cifelli R., Rutledge S. A., Storm morphology and rainfall characteristics of TRMM precipitation features, Monthly weather review, 2006, vol. 134, p. 2702

Reboita M. S., Gan M. A., Rocha R. P., Ambrizzi T., Regimes de precipitação na América do Sul: uma revisão bibliográfica, Revista Brasileira de Meteorologia, 2010, vol. 25, p. 185

Reinhardt T. E., Ottmar R. D., Castilla C., Smoke impacts from agricultural burning in a rural Brazilian town, Journal of the Air & Waste Management Association, 2001, vol. 51, p. 443

Rodriguez C. A. M., da Rocha R. P., Bombardi R., On the development of summer thunderstorms in the city of São Paulo: Mean meteorological characteristics and pollution effect, Atmospheric Research, 2010, vol. 96, p. 477

Rosenfeld D., TRMM observed first direct evidence of smoke from forest fires inhibiting rainfall, Geophysical Research Letters, 1999, vol. 26, p. 3105

Rosenfeld D., Lohmann U., Raga G. B., O'Dowd C. D., Kulmala M., Fuzzi S., Reissell A., Andreae M. O., Flood or drought: how do aerosols affect precipitation?, science, 2008, vol. 321, p. 1309

Rotunno R., Klemp J. B., Weisman M. L., A theory for strong, long-lived squall lines, Journal of the Atmospheric Sciences, 1988, vol. 45, p. 463

Rubin J. I., Collins W. D., Global simulations of aerosol amount and size using MODIS observations assimilated with an Ensemble Kalman Filter, Journal of Geophysical Research: Atmospheres, 2014, vol. 119

Saleeby S. M., Cotton W. R., Simulations of the North American Monsoon System. Part I: Model Analysis of the 1993 Monsoon Season, Journal of Climate, 2004, vol. 17, p. 1997

Saleeby S. M., Cotton W. R., A binned approach to cloud-droplet riming implemented in a bulk microphysics model, Journal of Applied Meteorology and Climatology, 2008, vol. 47, p. 694

Salio P., Nicolini M., Zipser E. J., Mesoscale convective systems over southeastern South America and their relationship with the South American low-level jet, Monthly Weather Review, 2007, vol. 135, p. 1290

Schwartz C. S., Romine G. S., Weisman M. L., Sobash R. A., Fossell K. R., Manning K. W., Trier S. B., A real-time convection-allowing ensemble prediction system initialized by mesoscale ensemble Kalman filter analyses, Weather and Forecasting, 2015, vol. 30, p. 1158

Silva Dias M. A. F., Rozante J. R., Machado L. A. T., Complexos Convectivos de Mesoescala na América do Sul, Tempo e Clima no Brasil, 2009, pp 181–194

Su F., Hong Y., Lettenmaier D. P., Evaluation of TRMM Multisatellite Precipitation Analysis (TMPA) and its utility in hydrologic prediction in the La Plata Basin, Journal of Hydrometeorology, 2008, vol. 9, p. 622

Tao W.-K., Chen J.-P., Li Z., Wang C., Zhang C., Impact of aerosols on convective clouds and precipitation, Reviews of Geophysics, 2012, vol. 50

Tao W. K., Li X., Khain A., Matsui T., Lang S., Simpson J., Role of atmospheric aerosol concentration on deep convective precipitation: Cloud-resolving model simulations, Journal of Geophysical Research, 2007, vol. 112, p. D24S18

Torres J. C., Nicolini M., A composite mesoscale convective systems over southern South America and its relationship to low-level jet events. In CONFERENCE ON SOUTH AMERICAN LOW-LEVEL JET, CD-ROM, Santa Cruz de la Serra , 2002

Tremback C. J., , 1990 Numerical simulation of a mesoscale convective complex: Model development and numerical results

Tripoli G. J., Cotton W. R., The Colorado State University three-dimensional cloud mesoscale model – 1982. Part I: General theoretical framework and sensitivity, Journal de Recherches Atmospheriques, 1982, vol. 16, p. 185

Twomey S., Pollution and the planetary albedo, Atmospheric Environment, 1974, vol. 8, p. 1251

van den Heever S. C., Carrió G. G., Cotton W. R., DeMott P. J., Prenni A. J., Impacts of nucleating aerosol on Florida storms. Part I: Mesoscale simulations, Journal of the Atmospheric Sciences, 2006, vol. 63, p. 1752

Velasco I., Fritsch J. M., Mesoscale convective complexes in the Americas, Journal of Geophysical Research, 1987, vol. 92, p. 9591

Vera C., Baez J., Douglas M., Emmanuel C. B., Marengo J., Meitin J., Nicolini M., Nogues-Paegle J., Paegle J., Penalba O., Salio P., Saulo C., Silva Dias M. A. F., Silva Dias P., Zipser E. J., The South American Low-Level Jet experiment, Bulletin of the American Meteorological Society, 2006, vol. 87, p. 63

Walko R. L., Cotton W. R., Meyers M., Harrington J., New RAMS cloud microphysics parameterization part I: the single-moment scheme, Atmospheric Research, 1995, vol. 38, p. 29

Wall C. L., The impact of aerosols on convective clouds: a global perspective, The University of Utah, 2013, Ph.D. Thesis

Weng Y., Zhang F., Assimilating airborne Doppler radar observations with an ensemble Kalman filter for convection-permitting hurricane initialization and prediction: Katrina (2005), Monthly Weather Review, 2012, vol. 140, p. 841

Whitaker J. S., Hamill T. M., Wei X., Song Y., Toth Z., Ensemble data assimilation with the NCEP global forecast system, Monthly Weather Review, 2008, vol. 136, p. 463

Wilks D. S., Statistical methods in the atmospheric sciences second edn. Academic press, Elsevier Burlington, 2006, 610

Williams E., Rosenfeld D., Madden N., Gerlach J., Gears N., Atkinson L., Dunnemann N., Frostrom G., Antonio M., Biazon B., Camargo R., Franca H., Gomes A., Lima M., Machado R., Manhaes S., Nachtigall L., Piva H., Quintiliano W., Machado L., Artaxo P., et al., Contrasting convective regimes over the Amazon: Implications for cloud electrification, Journal of Geophysical Research: Atmospheres, 2002, vol. 107

WWAP The United Nations World Water Development Report 3: water in a changing world. Paris: UNESCO, 2009, 429

Zhang F., Minamide M., Clothiaux E. E., Potential impacts of assimilating all-sky infrared satellite radiances from GOES-R on convection-permitting analysis and prediction of tropical cyclones, Geophysical Research Letters, 2016, vol. 43, p. 2954

Zhou C., Zhang X., Gong S., Wang Y., Xue M., Improving aerosol interaction with clouds and precipitation in a regional chemical weather modeling system, Atmospheric Chemistry and Physics, 2016, vol. 16, p. 145

Zipser E. J., Cecil D. J., Liu C., Nesbitt S. W., Yorty D. P., Where are the most intense thunderstorms on Earth?, Bulletin of the American Meteorological Society, 2006, vol. 87, p. 1057

Zupanski D., Hou A. Y., Zhang S. Q., Zupanski M., Kummerow C. D., Cheung S. H., Applications of information theory in ensemble data assimilation, Quarterly Journal of the Royal Meteorological Society, 2007, vol. 133, p. 1533

Zupanski D., Zupanski M., Grasso L. D., Brummer R., Jankov I., Lindsey D., Sengupta M., Demaria M., Assimilating synthetic GOES-R radiances in cloudy conditions using an ensemble-based method, International journal of remote sensing, 2011, vol. 32, p. 9637

Zupanski M., Maximum likelihood ensemble filter: theoretical aspects, Monthly Weather Review, 2005, vol. 133, p. 1710

Zupanski M., Fletcher S., Navon I. M., Uzunoglu B., Heikes R. P., Randall D. A., Ringler T. D., Daescu D., Initiation of ensemble data assimilation, Tellus A, 2006, vol. 58, p. 159

Zupanski M., Navon I. M., Zupanski D., The Maximum Likelihood Ensemble Filter as a non-differentiable minimization algorithm, Quarterly Journal of the Royal Meteorological Society, 2008, vol. 134, p. 1039

Zupanski M., Zupanski D., Cloud-Resolving Ensemble Data Assimilation. In The 5-th WMO Symposium on Data Assimilation , 2009, p. 5

# Appendix

# Appendix A

# Implementations on BRAMS–4.3

## *A.1 Updates, adjustments and code problems*

Corrections were made in the subroutine responsible to select the varfiles, which are used to initialize the model as well as to feed its grid boundaries. This subroutine had problems in finding varfiles when the model was started in history mode. The error occurs if BRAMS is started at 24:00 UTC or at exactly time of the varfile. These corrections are really important because allow BRAMS to work correctly with the assimilation algorithm.

Several modifications were done in the MLEF code in order to gather the varfiles generated by BRAMS and work in parallel mode in the TUPÃ and SDUMONT supercomputers. An expressive amount of time was spent for the purpose of making the algorithm work correctly with many cores at the same time.

The Community Radiative Transfer Model (CRTM), broadly known in the scientific community, was implemented in MLEF, making possible infrared satellite data assimilation. CRTM can compute the brightness temperature within the longwave infrared spectrum from model variables. This synthetic satellite data can be compared to GOES observations, permitting MESOASSIM to assimilate this type of data.

The current version of the two moment microphysics (2M) used in RAMS, version 6, was implemented into BRAMS. According to Cotton et al. (2003), this parameterization comes with many benefits, such as:

- New hydrometer category called drizzle, which improves the collection process for the rain droplets formation;
- Source and sink processes of CCN;

- Bin scheme for the riming process;
- Bin sedimentation scheme;
- Sea salt and dust treatment;
- Implementation of a more efficient and stable algorithm for heat and vapor diffusion.

Minor changes have been make in BRAMS's anisotropic deformation boundary layer parameterization (Lilly, 1962; Hill, 1974) due numerical instability, when the model was initialized in homogeneous mode. In addition, a RAMS's warm bubble subroutine was implemented into BRAMS in order to be used with this initialization mode. The warm bubble can be configured directly from the model's namelist (RAMSIN).

Loftus et al. (2014) has implemented a scheme for predicting the hail reflectivity Z$h$ (3MHAIL) into RAMS 2M microphysics. According to Dye et al. (1974), the radar reflectivity factor is given by the sixth moment of the number density distribution. Once we have Z$h$, the hail shape parameter can be diagnosed for every time step instead of being fixed during the whole simulation. This approach leads to a more realistic representation of hail size spectrum. Moreover, 3MHAIL parametrization deals in a more coherent way with the hail melting process and, thereafter, generates more reliable downdrafts. As another advantage, this parametrization is capable to simulate reasonable amount and diameter of precipitated hail particles at the surface. Due to all the advantages related to 3MHAIL, this parametrization was implemented into BRAMS. Unfortunately, the version of 3MHAIL available had some coding problems which generated numerical instability. Two months of debugging was necessary to solve these numerical problems.

The aforementioned implementations discussed in the above section have taken basically the whole internship period at CSU. Many computational problems had to be overcome and dozens of programs were developed from scratch in order to make the MESOASSIM framework work properly. All these coding work was accomplished in just one year for which I am thankful to the guidance of Dr. Carrió, who has a vast knowledge of numerical models.

## A.2 Validation of microphysical parameterizations

Once the atmospheric model was updated, comparative experiments were done between BRAMS 4.3 and RAMS 6.0 in order to evaluate if the microphysical scheme implemented in to BRAMS is working correctly. Both models were initialized with a horizontal homogeneous field, whose vertical profile is showed in Figure A.1. The experiments were split into high and low CCN concentrations, 2000 $cm^3$ e 300 $cm^3$, respectively.

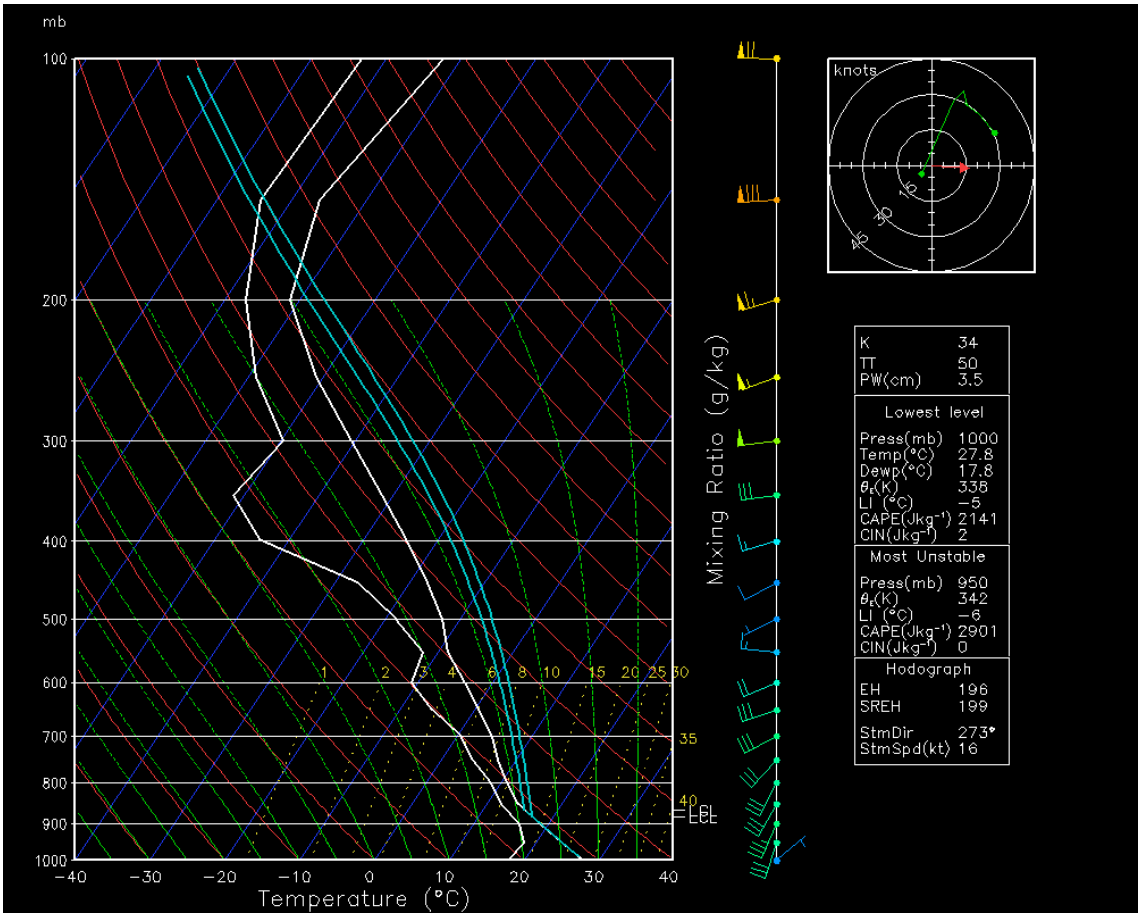


*Figure A.1:* Skew-t diagram of temperature, dew point temperature and wind used in the numerical experiments.

Figure A.2 shows the total grid integration of supercooled cloud water ($r_{sr}$), rain ($r_r$), and hail ($r_h$) mixing ratios as well as the maximum vertical velocity throughout the simulation time for the two moments microphysical scheme. Blue and red lines represent the BRAMS and RAMS results, respectively, where dashed lines indicate high CCN concentrations and solid lines indicate low CCN concentrations. Analyzing the figures, we perceive that the 2M implementation was successful since both models show similar results, in which a high CCN concentration is associated with larger $r_{sr}$ and smaller $r_r$ and

$r_h$. $w_{max}$ does not present any significant response to varying aerosol concentrations.

Figure A.3 is similar to Figure A.2, but for 3MHAIL scheme. The BRAMS and RAMS experiments show similar behavior, being more sensitive to different CCN concentrations when compared to Figure A.2. Higher aerosol loading generates larger $r_{sr}$ and smaller $r_r$. However, total integrated hail mixing ratio does not show significant response to the CCN concentration.

The total accumulated rain (acr) and hail (ach) at the surface, during 45 minutes of simulation, are shown in Figures A.4 and A.5, respectively. Both figures were made from 2M parametrization for high and low CCN concentrations. Great similarity is observed between BRAMS and RAMS results, which do not show significant contrast related to aerosol loading. Figure A.6 and A.7 were made as the last figures, but using 3MHAIL parametrization. The models present similar results with almost no response to CCN concentrations.

Considerable differences are observed between 2M and 3MHAIL with respect to surface amounts of rain and hail. Larger values of acr and ach are seen in both models for 3MHAIL, when compared to 2M. Indeed, unlike the 3MHAIL scheme, the 2M microphysical parametrization is not capable of generating reasonable amounts of hail over the surface, as explained before.

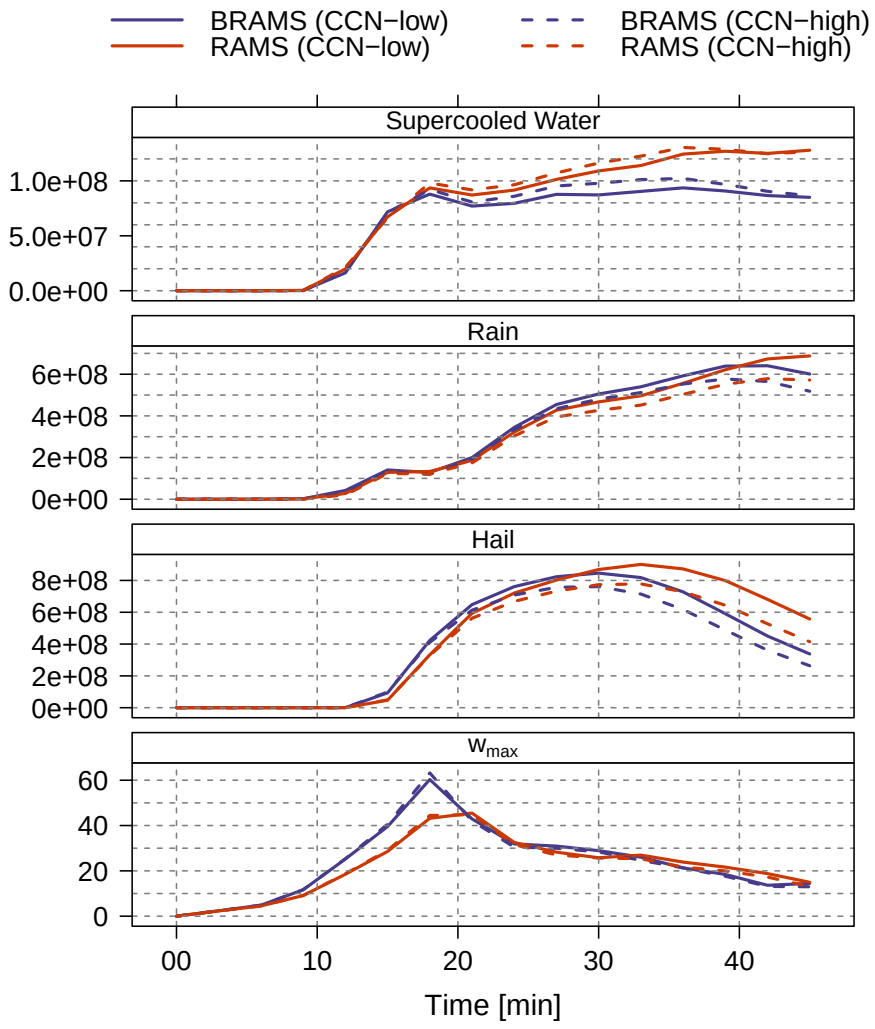


*Figure A.2:* Total grid integration of supercooled cloud water, rain and hail mixing ratios as well as maximum vertical velocity from BRAMS (blue line) and RAMS (red line). The experiments with low and high CCN concentrations are represented by solid and dashed, respectively. These numerical simulations were done by using the 2M scheme.

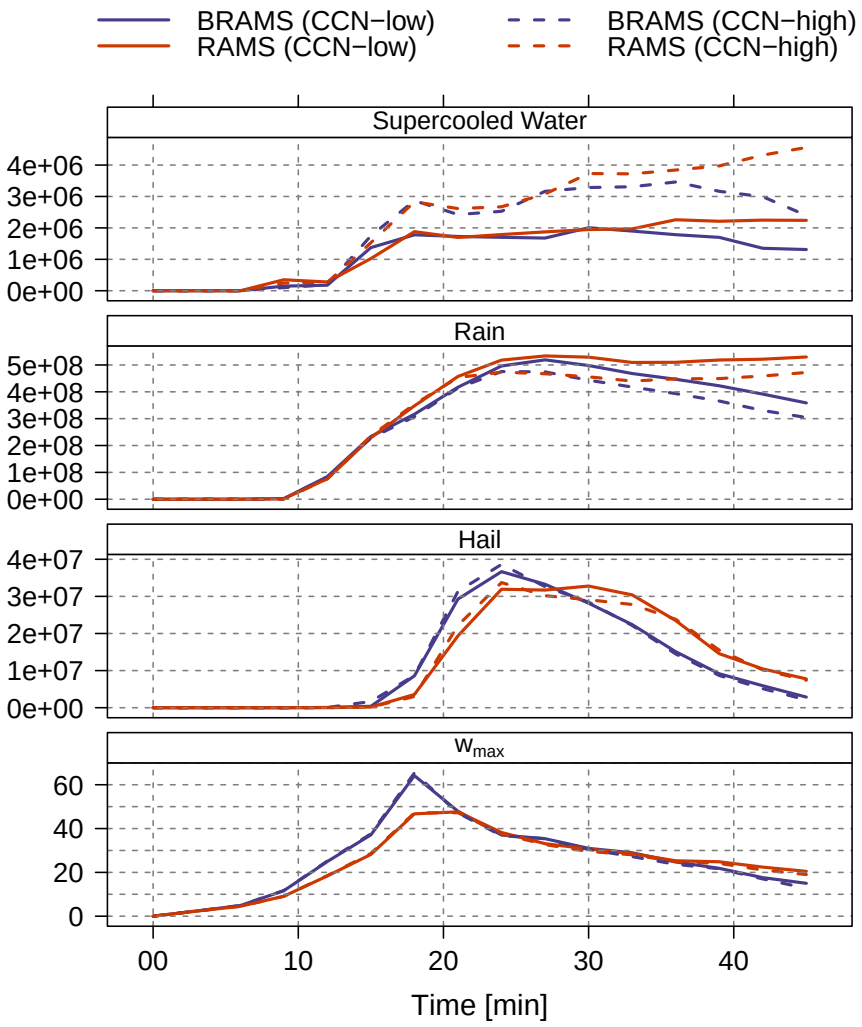


*Figure A.3:* Same as Figure A.2, but with 3MHAIL scheme.

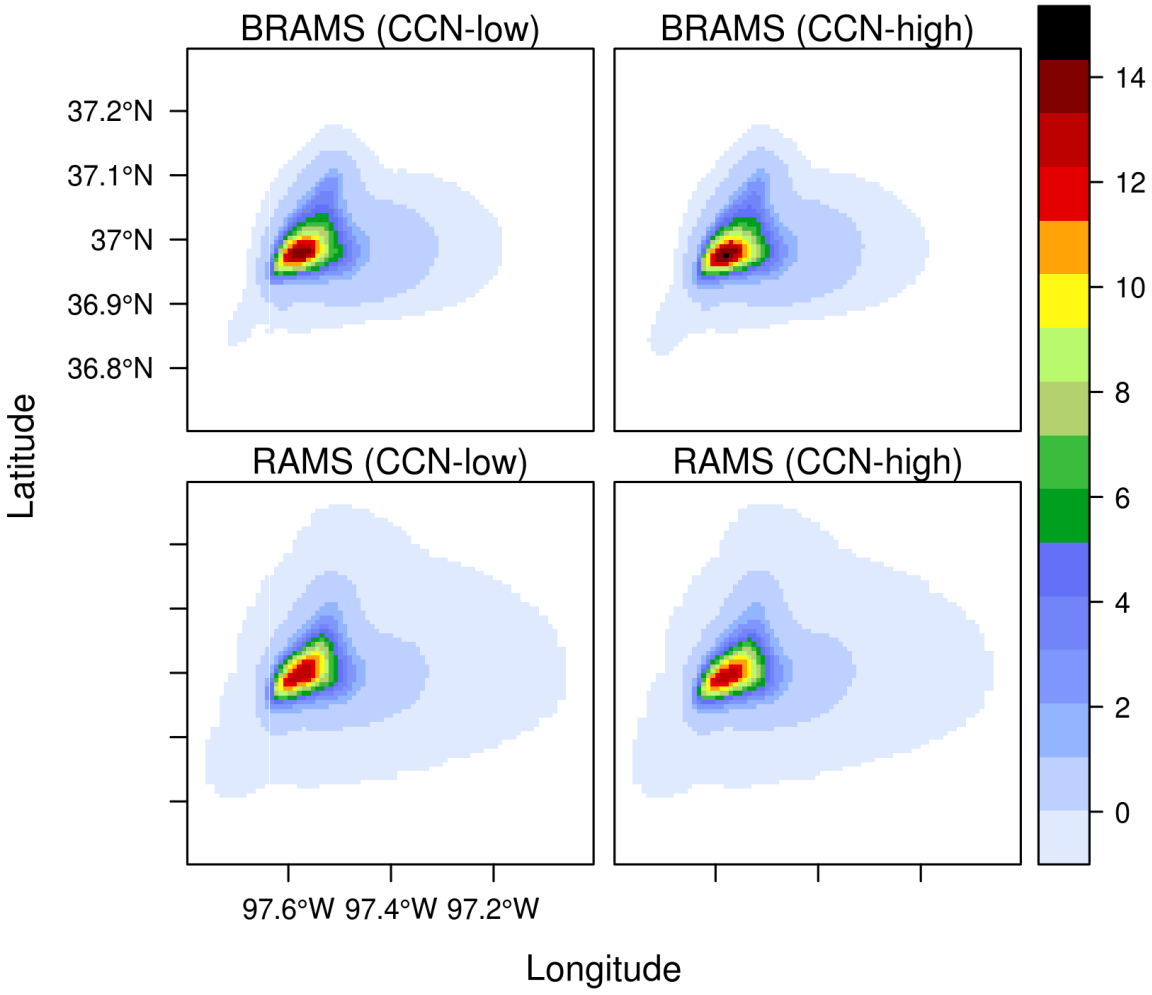


*Figure A.4:* Surface amounts of rain during 45 minutes of simulation from BRAMS and RAMS for low and high CCN concentrations using the 2M microphysical parametrization.

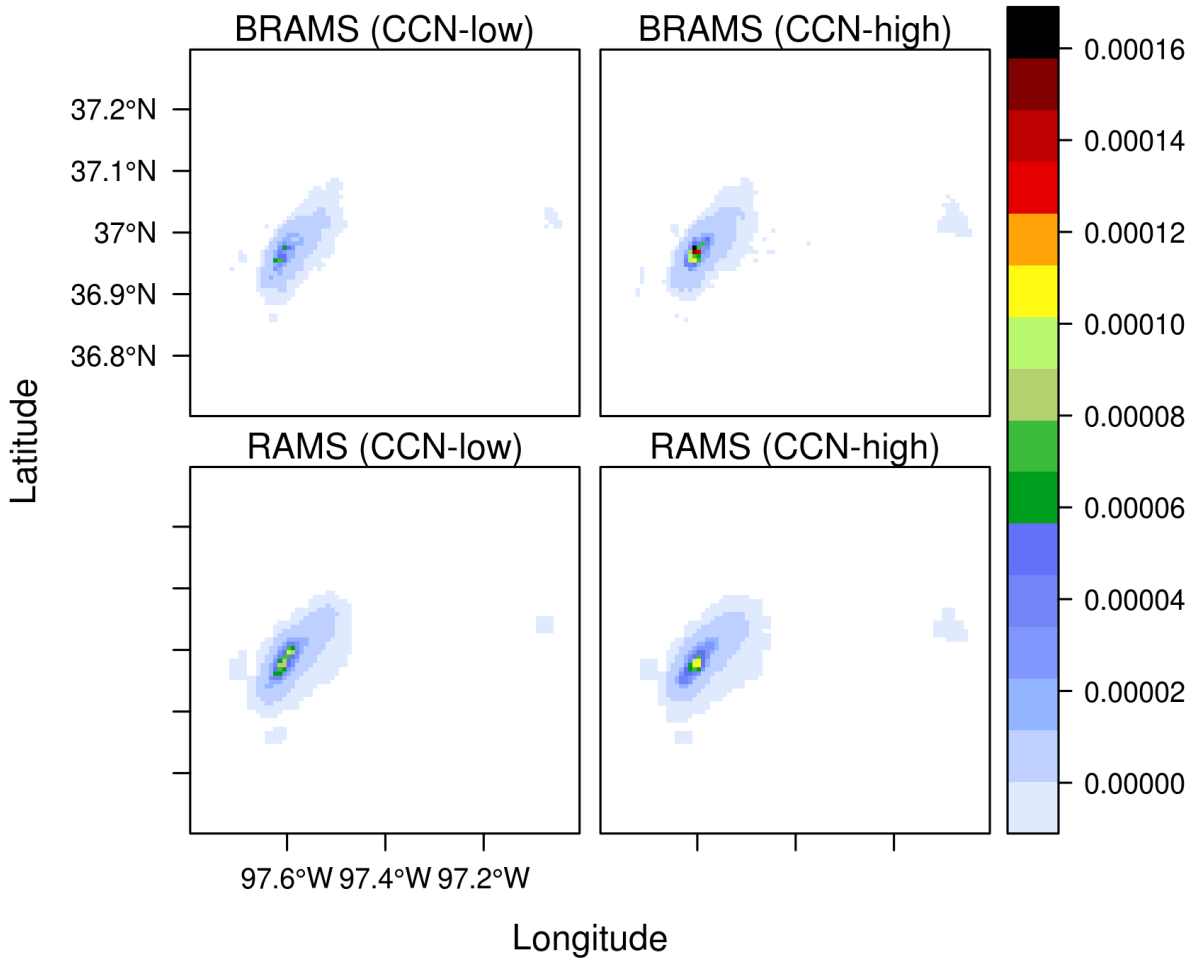


*Figure A.5:* Surface amounts of hail (ach) during 45 minutes of simulation from BRAMS and RAMS for high and low CCN concentrations using the 2M microphysical parametrization.

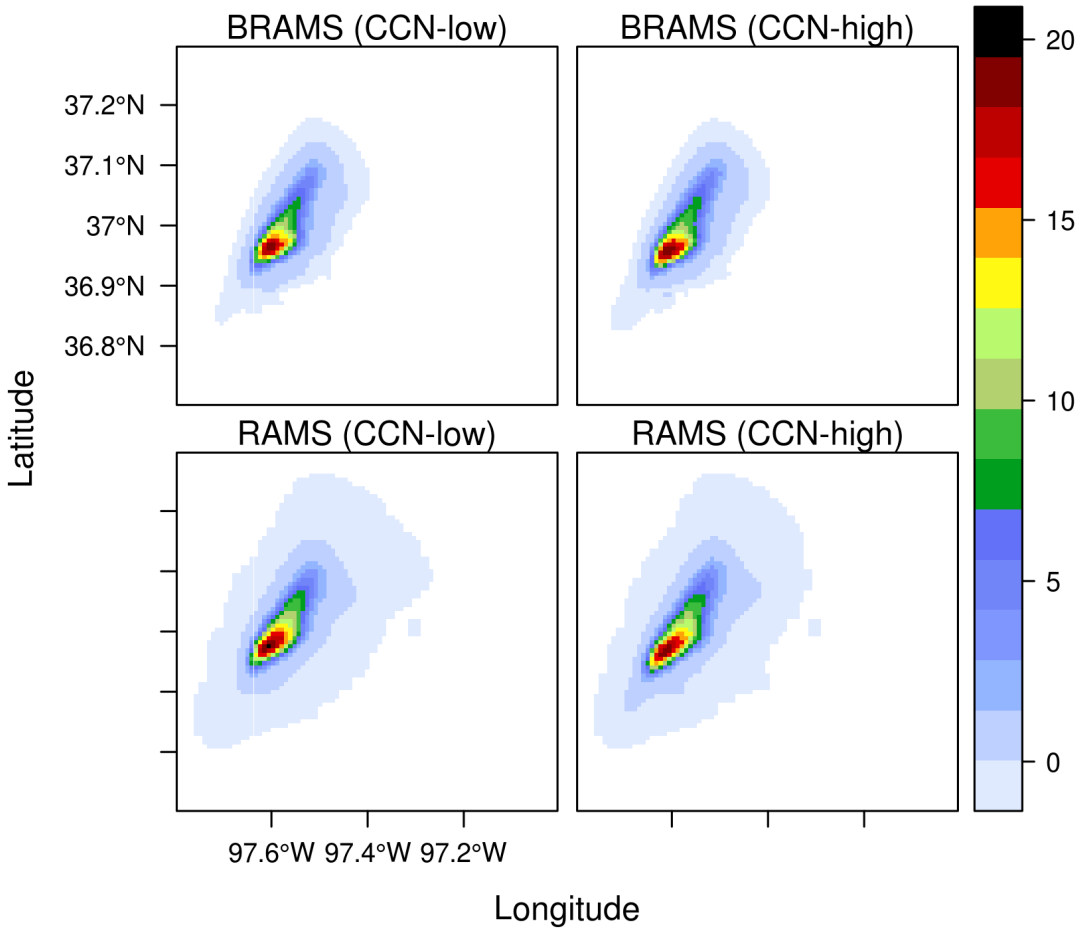


*Figure A.6:* Same as Figure A.4 but using 3MHAIL scheme.

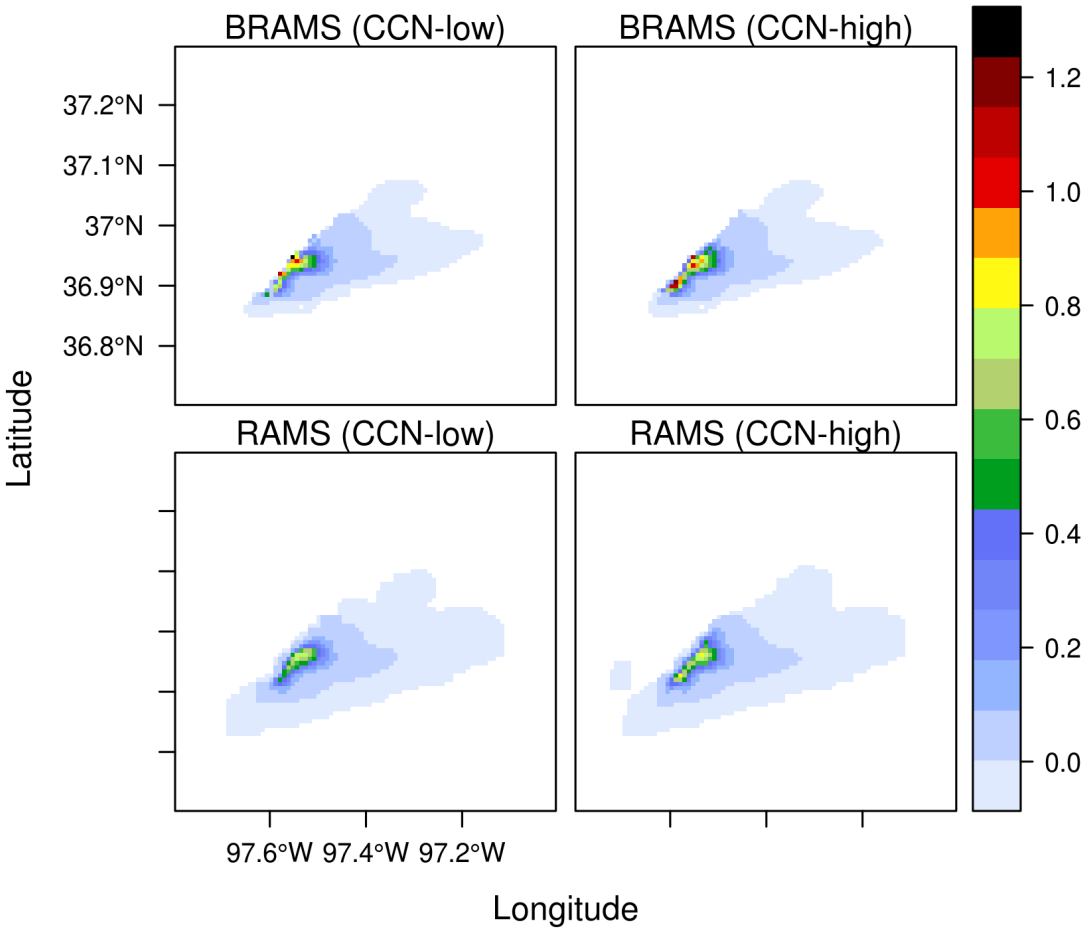


*Figure A.7:* Same as Figure A.5 but using 3MHAIL scheme.